Liquid Phase Profile Reactors for the Epoxidation of Propylene to Propylene Oxide on Titanium Silicalite-1 Catalyst: Spatially Resolved Measurements and Numerical Simulations

Vom Promotionsausschuss der
Technischen Universität Hamburg

zur Erlangung des akademischen Grades
Doktor-Ingenieur (Dr.-Ing.)

genehmigte Dissertation

von
Andres Eduardo Aquino

aus
Chubut, Argentinien

2023

1. Gutachter: Prof. Dr. rer. nat. Raimund Horn
2. Gutachter: Prof. Dr.-Ing. Michael Schlüter
Tag der mündlichen Prüfung: 25. September 2023
https://doi.org/10.15480/882.8789

1 Abstract

The spatial profile measurement technique was applied for the first time to a liquid phase reaction to study the selective oxidation of propylene to propylene oxide with hydrogen peroxide over Titanium Silicalite-1 catalyst, also known as (HPPO) process. Two spatial profile reactors based on the minimal invasive capillary sampling technique were design, constructed and brought into operation for this work. Both reactors are able to measure spatially resolved concentration and temperature profiles at industrially relevant conditions, that is 40°C and 20-35 bar pressure, with propylene entirely in liquid phase. A compact profile reactor was used to perform kinetics studies. The reaction was carried with different contact times LHSV = 3.0, 6.0 and 12.0 $[h^{-1}]$ respectively, achieving high conversion and selectivity. The experimental data while transitioning towards steady state shows that the catalyst undergoes an induction/activation period in which the target reaction of formation of propylene oxide progressively is being catalyzed. An average of 24 hours was required to reach a stable final concentration of propylene oxide with a carbon closure of less than 10%, at this point the reaction was considered in steady state. The spatially resolved concentration profiles of the main epoxidation reaction follows an pseudo-zeroth-order behavior. Several DFT studies reported that the rate determining step in the epoxidation reaction sequence is the adsorption dissociation of hydrogen peroxide on the Ti site of the catalyst. In this sense, when the concentration of hydrogen peroxide molecules far exceeds the number of available Ti sites on the surface of the catalyst the epoxidation rate will be limited by the maximal speed at which Ti sites can adsorb and dissociate hydrogen peroxide molecules, leading to the observed pseudo-zeroth-order behavior. In contrast to the main epoxidation reaction, the side products concentration profiles exhibit a typical non-linear trend. As primary side products of reaction 1-methoxy-2-propanol, 2-methoxy-1-propanol and propylene glycol were quanti-

fied. Also hydroxacetone and methoxyacetone from the reaction of 1-methoxy-2-propanol, 2-methoxy-1-propanol and propylene glycol with hydrogen peroxide were detected as secondary side products. Formic acid, methylformate, dipropyleneglycol methylether isomers and dipropyleneglycol isomers were detected in trace amounts. Quantitative data for the formation of hydroxyacetone is provided for the first time.

The experimental concentration profiles were simulated using an axial 1D-pseudo-homogeneous dispersion model with two kinetic models reported in the scientific literature. It was found that the models from the literature cannot predict accurately the spatially resolved concentration profiles measured in this work. This might be explained by the fact that these models are based on the assumption that the rate determining step is the propylene reaction with the $Ti \bullet OOH$ active specie on the surface of the catalyst. Additionally, a kinetic model based on an Eley-Rideal mechanism in which the rate determining step is the dissociative adsorption of hydrogen peroxide on the Ti site to form the $Ti \bullet OOH$ active specie is proposed. Upon linearization, the derived model shows a correlation of $R^2 = 0.99$ and $R^2 = 0.98$ with the linearized form of the experimental differential rate. The small deviation from linearity is attributed to the variation of the model parameters with the local temperature. Statistical analysis of the models in this work shows that the derived Eley-Rideal mechanism has the highest correlation with the concentration gradients measured within the catalyst bed.

A pilot scale reactor with a internal diameter comparable to those in technical scale (HP-PO) reactors was implemented to compare two approaches under same reaction conditions. On one hand, the reactor was packed with catalyst extrudates with dimensions similar to those implemented in industrial applications. Alternatively, a potential solution for process intensification was explored. In this case, the reactor was packed with additively manufactured catalyst-coated open cell structures as substitute approach for the conventional randomly packed bed reactor. By comparing the two approaches at same specific flow and conversion a reduction of the local temperature from 45.5°C to 42.5°C was observed for the randomly packed bed and the open cell structures respectively. Additionally, an increase of the selectivity toward propylene oxide of about 18% and of the yield of reaction of about 13% was measured. Nevertheless, these improvements cannot

be attributed conclusively to the enhanced thermal transport properties of the open cell structures due to a flattening of the concentration profile after 30 mm of catalyst bed. From the experimental data is not possible to conclude that the improvements in terms of selectivity and yield would have remained the same if the reaction would have proceeded undisturbed throughout the whole length of the catalytic bed. Even though questions still remain, these results may provide a basis for further investigation on the application of periodic open cells structures as alternative packing for fixed bed reactors, most particularly on kinetically limited reaction systems.

Contents

1 Abstract

2 Introduction **1**

3 Theory **4**

3.1 Industrial production of propylene oxide 4

3.1.1 Future trends in the propylene oxide production 8

3.2 The hydrogen peroxide-propylene oxide process (HP-PO) 10

3.2.1 Hydrogen peroxide-propylene oxide process (HP-PO) in the industry 10

3.2.2 Titanium silicalite-1 catalyst 12

3.2.3 Kinetics of the HP-PO reaction 14

3.2.4 Reaction mechanism of the (HP-PO) reaction 20

3.2.5 Effects of reaction conditions: solvent, temperature and pressure 26

3.3 Periodic Open Cell Structures (POCs) 27

3.4 Spatial profile reactors 31

3.5 Measurements in experimental fixed bed reactors 37

4 Materials and Methods **41**

4.1 List of chemicals used 41

4.2 TS-1/SiO_2 catalyst preparation and characterization 41

4.3 Periodic Open Cells Coating Procedure 43

4.4 Analytical Methods 45

4.5 Modeling of fixed bed reactors 47

4.6 Profile data fitting 53

5 Results and Discussion **57**

5.1 Liquid phase spatial profile reactors 57

5.1.1 Pilot scale spatial profile reactor 58

5.1.2 Compact profile reactor (CPR) 61

5.1.3 Dosing system and sampling 62

5.2 Catalyst Characterization 63

5.3 POC Coating 65

5.4 Determination of products of reaction, mass balance 67

5.5 Experimental measurements in compact profile reactor (CPR) . . . 72

5.6 Experimental determination of external mass transfer limitations . . 73

5.7 Determination of steady state 75

5.8 Spatially resolved concentration profiles 81

5.9 Validation of kinetic models from literature 87

5.10 Development of kinetic model 92

5.11 Measurements in (HP-PO) pilot scale reactor 104

6 Summary & Outlooks **110**

7 Appendix **116**

7.1 Evaluation of transport limitations and dispersion 116

7.2 Kinetic parameters used for numerical simulations 120

2 Introduction

Catalysis plays a fundamental role in the modern world and is a key factor in developing sustainable chemical and biochemical processes. These materials enable the efficient utilization of limited natural resources by increasing the rate of reaction, decreasing the rate of unwanted side products and reducing the waste generation. Their importance is reflected by the fact that 35 % of the world GDP is influenced by some type of catalyst [1]. In the particular case of the chemical industry, 85 % of the chemical products are produced by heterogeneous catalysis [2]. For applications that use solid catalysts, fixed bed reactors are often preferred in the industry. In this type of reactors catalyst particles are arranged randomly and held in position while the fluid phase flows around them. Due to the simple constructions with no moving parts, flexible and stable temperature control this type of reactors are used in a wide range of applications and reactions conditions. In contrast to homogeneous catalyst, where the active site is well defined, catalytic processes taking place on heterogeneous catalyst are often more complicated. This is because the nature of the active site is usually not well defined. For this reason, research and development of new processes in heterogeneous catalysis is challenging and often trial and error based approach are used. Moreover, these challenges are enhanced by the fact that reactions are often performed at elevated pressures, temperatures and with hazardous chemicals increasing the difficulty of measuring inside of the reactor to obtain reliable kinetic data. For this reason, most experimental reactors rely on inlet and outlet measurements while their interior remains as a black box. The reactor is often operated in differential mode (small conversion) and as isothermal as possible to allow assignment of the measured rates to the inlet concentration and temperature values. To obtain kinetic data and explore the reaction network, the contact time or a proportional quantity such as the mass of the catalyst divided by the inlet flow rate has to be varied

systematically which underlines extensive experimental work. In this sense, traditional approaches such as integral or differential experimental fixed bed reactor can provide only a limited amount of information about the spatiotemporal evolution of the reaction throughout the catalytic bed. In consequence, a complete understanding of the overall reaction process cannot be obtained by these inlet-outlet measurements techniques and models derived from such experiments may have a narrow range of applicability. For this reason, new trends are emerging in the catalysis community to develop techniques suitable to probe a solid catalyst under working conditions [3], [4] [5], [6], [7], [8], [9], [10]. One of these new trends is the measurement of spatially resolved profiles within catalytic reactors, in particular in fixed-bed reactors, which are characterized by pronounced spatial gradients in almost all process variables. The term spatially resolved profiles refers to the measurement of kinetically relevant variables within the reactor catalyst bed such as molar concentration of species or molar flow rates ($C_i(z)$, $n_i(z)$) and temperature in the fluid phase ($T_f(z)$) as a function of the spatial coordinate (z). The spatial sampling principle is based on the movement of a thin sampling capillary along the axis of a reactor that continuously transfers a representative sample of the actual position (z) to an analytical device for analysis. The most robust and widely applied technique to measure spatial profiles inside catalytic fixed-bed reactors is the minimally invasive capillary sampling technique. This technique was developed independently and in different embodiments by various groups [7], [8], [9]. The spatial profile technique by Horn et.al [4], [11], [12] uses a closed capillary design with a side sampling orifice. This design provides the sampling capillary enhanced mechanical stability which opens a wide spectrum of applications in heterogeneous catalysis, most specifically, in the measurement of spatially resolved kinetic and spectroscopic profiles in packed bed reactors. So far, the minimally invasive capillary sampling technique was restricted to heterogeneously catalyzed gas phase reaction.

The measurements presented in this work demonstrate for the first time the application of the minimal invasive spatial sampling technique to study a heterogeneous catalytic liquid phase reactions. The reaction studied in this work is the selective oxidation of propylene to propylene oxide with hydrogen peroxide on Titanium Silicalite-1 catalyst. Two different scales reactors are used in this work. A com-

mercially available compact profile reactor was used to study the reaction under safe conditions due to the small reacting volume and with low consumption of chemicals. In this case, the catalyst used are splits from sieved catalyst extrudates. Two models from the scientific literature were used to simulate the experimental data. Additionally, a new model based on a Eley-Rideal mechanism in which the rate determining step is the dissociative adsorption of hydrogen peroxide on the Ti site to form an $Ti \bullet OOH$ active specie(s) is proposed. A statistical analysis was performed to asses quantitatively the degree of correlation of the different models in this work with respect to the concentration gradients measured experimentally within the catalyst bed. The second reactor is a state of the art pilot scale profile reactor with an internal diameter comparable to the diameter used in technical scale applications. Two different reactors systems were compared in this case. On one hand, the pilot scale profile reactor was filled with catalyst extrudates with a size similar to those used in industrial applications conforming a randomly packed bed. Additionally, the reactor was packed with a structured bed constituted by additively manufactured catalyst-coated open cell structures. Both approaches were compared in terms of temperature, selectivity and yield under the same specific flow and conversion.

3 Theory

3.1 Industrial production of propylene oxide

Epoxides are a highly reactant chemical group due to the oxiranic ring present in their structures. This ring can be easily open in the right conditions to give a wide variety of chemical products. For this reason, epoxides are used as starting material to produce a huge scope of products such as polyesters resins, surfactants, polyurethane and lubricants. The two most important epoxides are ethylene oxide and Propylene oxide (PO). In 2010, the PO worldwide production was approximately 7.5 Mtons/year [13]. The applications of PO are the productions of polyether polyols (65%) which are used for the production of polyurethane foams, the production of propylene glycol (30%) and propylene glycol ethers (4%) [14]. Currently, ethylene oxide can be obtain in a gas phase oxidation with atmospheric oxygen over Ag/SiO_2 catalyst with high selectivity and conversions. In contrast, the direct gas phase epoxidation of Propylene (Pr) to PO in industrial scale has still not been developed. Due to issues regarding the catalytic stability, deactivation with time on stream, among others drawbacks this process is far from industrial standards. For this reason, alternative production methods for the synthesis of PO have been developed. The most widely commercialized production processes shown in Figure 3.1 are the dehydrochlorination of chlorohydrin largely used by DOW Chemicals, the hydro-peroxide processes (PO-MTBE, PO-SM) developed by Halcon Corp, the cumene-hydro-peroxide process (PO-CH) developed by Sumitomo Chemicals Ltd, and the hydrogen peroxide-propylene oxide (HP-PO) developed by DOW Chemicals-BASF and Evonik/Thyssenkrupp Industrial Solutions AG.

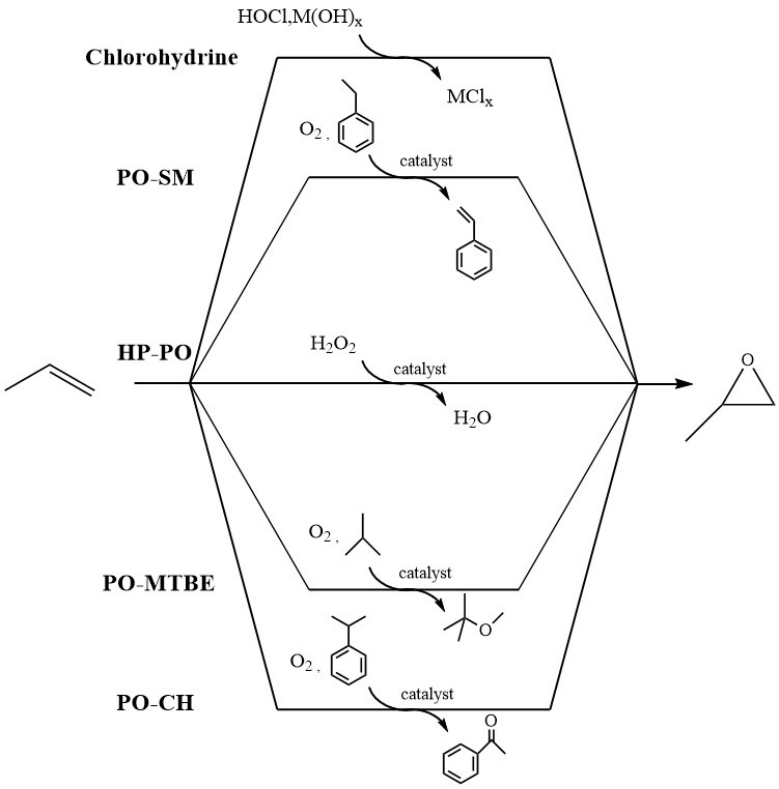

Figure 3.1: Reactions of the industrially relevant production processes for propylene oxide. Adopted from [15]

The majority of PO is currently produced by the chlorohydrin route first described by Wurtz et.al [16] in 1859. This process is performed in two steps. In the first step the intermediate hydrochlorous acid ($HOCl$) is formed by the reaction of water and gaseous chlorine. This intermediate reacts with Pr to form two propylene chlorohydrines, 2-chloro-1-propanol and 1-chloro-2-propanol respectively. As side products of reaction 1,2-dichloropropane and dichloro-dipropyl ether are formed. This reaction is usually performed in a bubble column reactor at 1.5 bar and 50°C. The two isomers are formed with a selectivity of 90-95%. The propylene chlorohydrines are subsequently dehydrochlorinated in a second step by calcium hydroxide or sodium hydroxide to form the target product PO. Beside PO, 2.1 tons of $CaCl_2$ and 0.1 tons of 1,2-dichloropropane and dichloro-dipropyl ether are obtained per ton of PO. This constitutes the main disadvantage of this process, since $CaCl_2$ solutions have low commercial value. When sodium hydroxide is used as base

for the dehydrochlorination the $NaCl_2$ formed can be use for the production of Cl_2 by electrolysis. This step reduces the salt load of the process waste water, but needs additional power and purification steps which increases the investment. Moreover, chlorine in aqueous solution, HCl and propylene chlorohydrine are extremely corrosive and the construction materials must be selected very carefully which underlines a high initial investment. Because of the disposal problems of the brine and chlorohydrin by-products and their environmental impact no new plant using this process are built [14], [17].
Others industrial processes for the production of PO can be divided into coproduct-producing processes such as propylene oxide-styrene monomer (PO-SM) and propylene oxide-methyl tert-butyl ether (PO-MTBE) respectively, and coproducts-free routes such as propylene oxide-cumene hydroperoxide (PO-CH) and propylene oxide-hydrogen peroxide (HP-PO). The (PO-SM) [18], (PO-MTBE) [19] and (PO-CH) [20] routes are based on the peroxidation of an alkane to an alkyl-hydroperoxide which reacts with Pr to produce PO and an alcohol using either homogeneous tungsten, molybdenum, vanadium catalyst or titanium based heterogeneous catalyst. In the case of the (PO-SM) process, the hydroperoxide is formed by the reaction of ethylbenzene with air at 146°C and 2 bar to form a mixture of 12-14% mass of ethylbenzene hydroperoxide in ethylbenzene. Then, the peroxide solution is mixed with Pr and homogeneous molybdenum catalyst [21], [22] or a titanium based heterogeneous catalyst [23], [24], [25] to produce PO. The epoxidation is performed at 100°C and 35 bar. The effluents of the epoxidation reactor are mainly constituted by PO, α-phenylethanol, acetonephenone, unreacted Pr and other organic impurities. The remaining α-phenylethanol, acetophenone mixture is fed to a dehydration reactor at 270°C and 0.35 bar with an alumina catalyst and triphenylmethane as solvent to form styrene with 98% selectivity. Both α-phenylethanol and acetophenone are the main byproducts of the process. The coproduct styrene can be commercialized for the production of styrene based polymers with a wide range of applications. In the (PO-MTBE) process, the hydroperoxide precursor is isobutane which reacts with oxygen to form tert-butyl-hydroperoxide [26]. This liquid phase reaction is usually preformed at 120-140°C and 25-35 bar. The isobutane conversion is usually about 48% at a selectivity of 50% towards the hydroperoxide. The products of reaction are constituted by tert-butyl hydroperoxide, tert-butyl alcohol from

the decomposition of the alkyl-hydroperoxide and smaller amounts of aldehydes and ketones. In a second step, the epoxidation reaction takes place by mixing the aforementioned mixture with a homogeneous catalyst (usually molybdenum salt) and Pr using toluene as solvent. This liquid phase reaction is performed at about 110°C and 40 bar pressure with a selectivity towards PO of about 80%. The conversion of Pr reaches about 9% per cycle from which about 98% is converted to PO. The tert-butyl alcohol is recovered and dehydrated to isobutane and then converted to methyl tert-butyl ether ($MTBE$) which is usually commercialized as fuel additive. In general, the (PO-SM) and (PO-MTBE) processes produce less waste than the chlorohydrine process and have the advantage of being chlorine free. A characteristic of these routes is the production of a coproduct in a fixed ratio, usually 2-4 times the amount of PO produced. The challenge using the coproduct technologies is to achieve a high PO selectivity and to have a competitive market for the coproduct.

Due to the mentioned drawbacks of the (PO-SM) and (PO-MTBE) processes, extensive research was performed to develop a coproduct free route for the production of PO. In this sense, the (PO-CH) process operated by Sumitomo Chemicals [20], [27] has two distinctive characteristics. The first one, is that cumene is easier to hydroperoxidate and is more stable than styrene or isobutane hydroperoxide. The second one, is that no coproducts are produced since the cumene alcohol formed in the epoxidation reaction can be hydrogenated back to cumene. This process involves several reactions steps. In a first step, cumene reacts with air at 80°C and 42 bar to produce a solution of 25% mass of cumene hydroperoxide in cumene [28]. In a second step, the epoxidation reaction takes place by the reaction of cumene hydroperoxide with Pr. This reaction is catalyzed by a mesoporous titanium silicate catalyst [29]. The outlet stream of the reactor is constituted by PO, dimethylphenylmethanol, acetophenone, unreacted Pr, and other organics. The dimethylphenylmethanol can be converted back to cumene by dehydration to methylstyrene on activated alumina followed by hydrogenation to cumene over palladium or copper based catalyst. The dehydration to methylstyrene and hydrogenation to cumene can be performed by packing one catalyst after the other in a single fixed bed reactor at 14 bar and 205°C [30]. Two plant were constructed using this technology one in 2003 in Chiba, Japan by Sumitomo with a capacity

of 200 kt/year and other in Saudi Arabia in 2009 by joint venture of Sumitomo and Saudi Aramco with the same capacity.

3.1.1 Future trends in the propylene oxide production

Despite the progress made in the PO production, a direct, sustainable and environmentally friendly single-step synthesis by direct epoxidation of Pr to PO is still not available. While ethylene oxide can be produced by direct epoxidation of ethylene using molecular oxygen over $Ag/\alpha Al_2O_3$ catalyst with high conversion and selectivity, the analog process for the production of PO still has not been developed. Attempts to implement an $Ag/\alpha Al_2O_3$ catalyst for the epoxidation of PO resulted in low conversion and selectivity. The unique characteristic of silver in the epoxidation of ethylene is found in its ability to dissociatively adsorb oxygen [31]. For propylene, the direct abstraction of a H atom by one of the dissociated oxygen atoms on the surface of the catalyst is more favorable than that for ethylene, because propylene is able to produce an allyllic intermediate. The reaction step shown in Figure 3.2 in which the epoxide precursor can react with the neighboring dissociated oxygen atom cannot happen with ethylene, because it has no γ-H atoms. This allyllic intermediate results in a lower energy barrier which can partly explain the lower epoxidation selectivity [14]. For this reason, acrolein instead of PO is preferentially formed during oxidation of propylene on silver catalyst. Alternatively, a wide range of catalytic systems both for liquid and gas phase direct epoxidation of Pr had been investigated. For the liquid phase direct epoxidation, soluble/insoluble molybdenum, tungsten, vanadium based catalyst [14] and molten salts such as $LiNO_3$, $NaNO_3$ and KNO_3 [32] have been used. For the direct gas phase epoxidation, both promoted Ag catalyst [33], [34], [35], [36], [37], [38], [39], [40] and Cu based catalyst [41], [42], [43], [44], [45] have been gaining significant attention. In all fore mentioned cases the catalyst performance in terms of stability, conversion and selectivity are far from industrial standards. So far the most promising route for a direct epoxdation of Pr to PO is the production of PO over nanometer Au catalyst in presence of both H_2 and O_2. This catalyst first developed by Haruta et.al [46] in 1998, showed that by supporting gold nanoparticles smaller than 4 nm on a titania

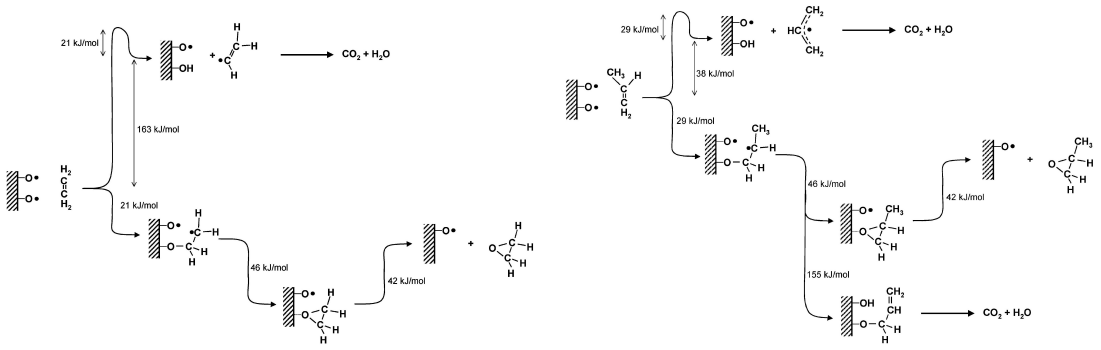

Figure 3.2: Reaction scheme for the epoxidation and total oxidation reaction pathways for Pr and ethylene over silver catalyst. Taken from [53]

oxide support a selectivity toward PO of upto 99 % can be obtained. Nevertheless this promising performance in terms of selectivity, the catalyst suffers from low Pr conversion of 1-2 %, deactivation of the catalyst with time on stream of few hours and lack of reproducibility of the catalytic performance [47]. A significant advance in this catalytic system is the implementation of microporous TS-1 with low Ti loadings as support. Delgass showed in a serie of publications that by combining highly disperse Ti and small Au nanoparticles synthesized by deposition precipitation method on TS-1, the catalyst reproducibility and stability can be enhanced achieving stable production for more than 45 hours [48], [49], [50], [51]. With the Au/TS-1 catalyst the Pr conversion was further improved to 8.8 % with a selectivity of 81 % at a reaction temperature of 200 °C. This led to the highest reported PO formation rate for standard reaction conditions of 1 atm, 200 °C and a feed composition of 10/10/10/70 $O_2/H_2/Pr/Ar$ of 160 $[g\ h^{-1}\ kg_{cat}^{-1}]$ [52]. Despite these improvements in performance, stability and reproducibility, current catalysts are still not economically competitive. Moreover, a crucial point for industrial applications is that the operation mode of the reactor is not clear due to the dangers of handling O_2/H_2 mixtures in a technical scale reactor.

3.2 The hydrogen peroxide-propylene oxide process (HP-PO)

Despite the effort made, a industrial scale direct synthesis route for PO with molecular oxygen is still not available. Through time, alternatives to develop a simpler, more efficient and environmentally friendlier PO synthesis route have been explored to overcome the drawbacks of the coproducts dependence of the (PO-SM)/(PO-MTBE) routes and the complexity and high energy demand of the (PO-CH) process. In this sense, the development of the epoxidation of Pr to PO by HP also know as (HP-PO) process has been a significant step forward. For this reason this process was awarded with the Green Chemistry award in 2010 by the US Environmental Protection Agency EPA [54]. Because of the high cost of the HP as oxidant the process economy is viable only if HP is produced in-situ. A strategy to overcome this limitation is to integrate both HP and PO production plants. Currently, most of HP is produced using the anthrahydroquinone autoxidation process [55], [56] which produces a diluted solution of HP in water and MeOH. The cost-saving feature of the (HP-PO) process is that the HP plant adducts can be used directly in the epoxidation of Pr without significant separation steps, which reduces the energy and transportation costs. Although is possible to use catalysts such as molybdenum oxide or tungsten oxide to epoxidize Pr with HP, these catalyst are sensitive to the presence of water which is usually present in HP solutions [57], [58]. Homogeneous catalyst are not widely used for this process because of the additional separation costs. The direct integration of both HP and PO production processes is enabled by the TS-1 catalyst, which is able to epoxidize Pr in an aqueous solution of HP at mild conditions without catalyst deactivation. In the following sections the details of the (HP-PO) process will be highlighted.

3.2.1 Hydrogen peroxide-propylene oxide process (HP-PO) in the industry

The (HP-PO) process was developed independently by Evonik/Thyssenkrupp Industrial Solutions AG [15] and BASF/Dow Chemicals [59], [13]. Both technologies are similar being the most significant difference the type of reactor used for the

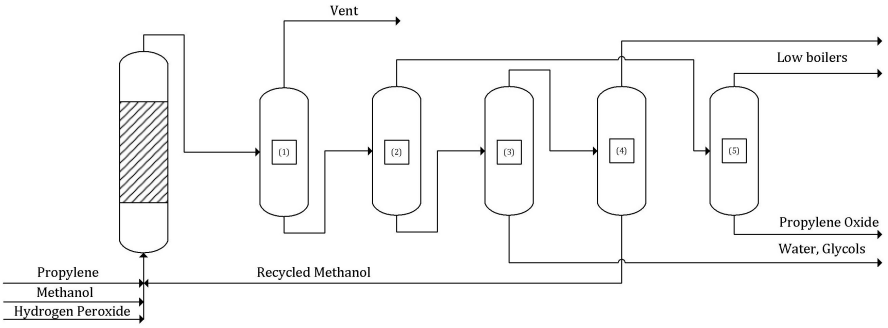

Figure 3.3: BASF/DOW HP-PO process simplified flow chart

epoxidation. The patented process by BASF and DOW uses a tubular fixed bed reactor with intermediate product separation [60], while Evonik/Thyssenkrupp carries the epoxidation in a patented plate bundle reactor for efficient heat removal [61]. A simplified flow diagram of the patented process by BASF and DOW is shown in Figure 3.3. The HP for the epoxidation is supplied by Slovay [13]. The epoxidation reaction is carried out at 40-60°C and 30 bar in a 2 step tubular fixed bed reactor with intermediate PO removal achieving full HP and Pr conversion [62], [13]. After reaction, the off gases are removed in Figure 3.3 (1) and the adducts of reaction are separated by 4 distillation columns in Figure 3.3 (2)-(4), the Methanol (MeOH) is recovered in Figure 3.3 (4) an recycled back. In 2008 BASF/DOW/Solvay inaugurated a 300 kton/year in Antwerp, Belgium using this technology.

A simplified flow diagram of the process by Evonik/Thyssenkrupp Industrial Solution AG is shown in Figure 3.4. The HP for the epoxidation is supplied by Evonik which is one of the world leading producers of HP [56]. In this case, the reaction is carried at 40-60°C and 20-30 bar in a patented plate bundle reactor [61]. After reaction, the adducts are expanded in a flash unit in Figure 3.4 (1) to separate the Pr from the liquid phase. Both Pr and MeOH are recovered and recycled back Figure 3.4 in (2) and (6) respectively. The product PO is purified in Figure 3.4 (5) with 99.9% purity. In 2008 Evonik/Tyssenkrupp built the first plant using the (HP-PO) technology in Ulsan, Korea with a capacity of 100 kton/year [15]. After these two first (HP-PO) plants in Ulsan Korea by Evonik/Tyssenkrupp and Antwerp, Belgium by BASF/Dow Chemicals/Slovay further sites in Saudi Arabia,

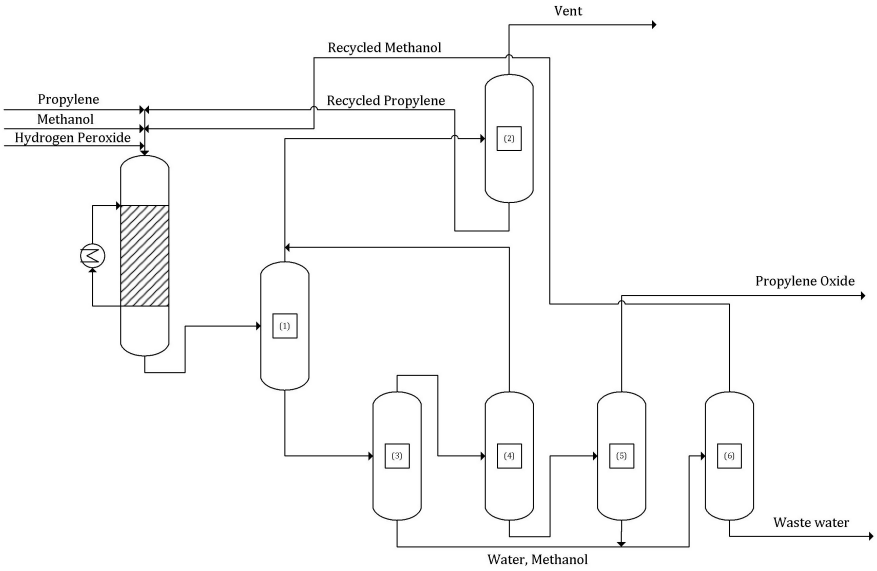

Figure 3.4: Evonik/Thyssenkrupp HP-PO process simplified flow chart

Thailand and China were announced which underlines the potential and interest on this new technology [15].

3.2.2 Titanium silicalite-1 catalyst

TS-1 is a transition metal substituted zeolite first synthesized by Taramasso et.al [63] by hydrothermal method of mixed alkoxides. The crystallization gel is obtained by the controlled hydrolysis of teraethyl orthotitanate (TEOT) $Ti(OC_2H_5)_4$ and tertaethyl orthosilicate (TEOS) $Si(OC_2H_5)_4$ using tetrapropylammonium hydroxide (TPAOH) as template. This mixture of alkoxides result in a zeolite were tetrahedral $[SiO_4]$ are substituted by $[TiO_4]$ units in the MFI framework [64]. The amount of titanium which can be inserted into the framework is limited to about 3 wt% TiO_2. The TS-1 MFI structure shows a three dimensional system of channels shown in Figure 3.5 of 0.5-0.6 nm that constitute the zeolite micropores. Several reviews about the synthesis, characterization and catalytic activity of the TS-1 catalyst are available in the scientific literature [65], [66], [67], [68].
The typical surface area and pore volume reported in literature are 420-450 $[m^2\ g^{-1}]$ and 0.18-0.26 $[cm^3\ g^{-1}]$ respectively [63], [69]. To confirm the presence of Ti(IV) in the zeolite framework, the TS-1 catalyst is typically characterized by IR, XRD

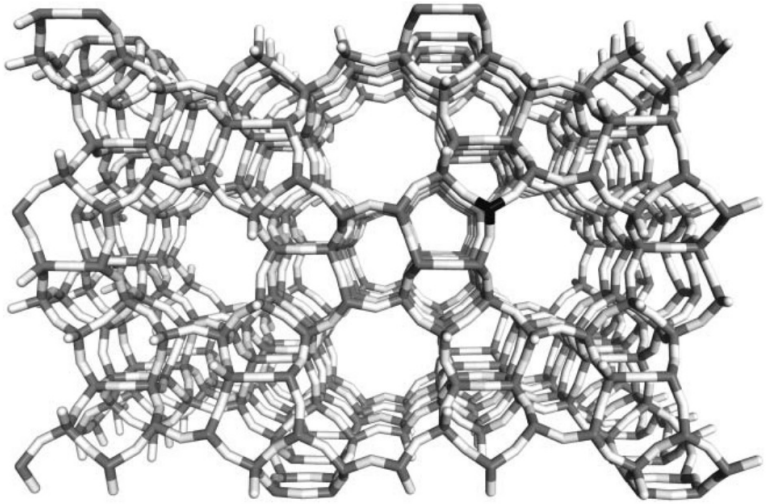

Figure 3.5: TS-1 structure, Si(grey) and Ti(black) tetrahedral connected via oxygen bridges (white) (taken from [64])

and UV-vis spectroscopy. The FT-IR spectra shows an absorption band at about 970 $[cm^{-1}]$ that is not present in the spectrum of either pure silicalites or titanium oxide [63], [70], this band is assigned to the asymmetric stretching mode of Si-O-Ti units and indicates the incorporation of Ti into the MFI framework [71]. The UV-vis spectra shows an absorption band near 215 nm which indicates the presence of tetrahedral Ti species while the absence of other peaks indicates that other phases of Ti such as amorphous, rutile or anatase are not present [72]. The XRD pattern of TS-1 catalyst shows an enhancement of the peaks at 24.4° and 29.3° when compared with the pattern of Silicalite-1 which indicates the incorporation of the Ti atoms in the MFI framework and the change from monoclinic symmetry of Silicalite-1 to a orthorhombic symmetry of Titanium Silicalite-1 [63], [73].

There are several publications and patents regarding the deactivation and regeneration of the TS-1 catalyst [74], [75], [76], [77], [78], [79]. The general agreed deactivation mechanism occurs by reduction of the available surface area due to blocking of the pores by the formation of oligomers within the narrow catalyst channels [80], [81]. It was experimentally observed, that the deactivation of the catalyst increases along the reactor axial coordinate reaching its maximum at the outlet of the reactor, where the concentration of side products is the highest [77]. Additionally, Wang et.al [78] performed a long term study to measure the catalytic

stability, deactivation and regeneration of TS-1 and derived an expression for the loss of activity based on the kinetic data.
The most used technique for the regeneration of the TS-1 catalyst is amthermal treatment with either diluted HP solutions at temperatures below 100 °C or with MeOH at 140-204 °C. An almost complete recovery of the surface area of the catalyst by treatment with diluted solutions of HP has been reported by both Degussa (currently Evonik) and Wang [79] [82].

3.2.3 Kinetics of the HP-PO reaction

In the liquid phase selective oxidation shown in Equation 3.1 Pr is oxidized by HP to PO on TS-1 with high selectivity (90-95%) at 40°C and at enough pressure to keep the Pr entirely in liquid phase (usually 30 bar) using MeOH as solvent. The only coproduct is water, what makes this reaction environmentally benign.

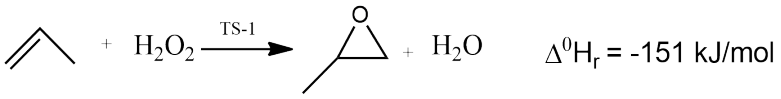

(3.1)

While several side products shown in Equation 3.2 have been reported for this reaction only 1-methoxy-2-propanol, 2-methoxy-1-propanol and propylene glycol (hereafter 1-MPOL, 2-MPOL and PG respectively) have been properly quantified [83], [84], [85], [86]. These side products can further react with PO to form oligomers by increasingly reacting with PO. The formation of side products lowers the overall yield of reaction and deactivates the catalyst. These high molecular weight oligomers cannot diffuse through the narrow pores of the catalyst blocking them and decreasing the available surface area for the reaction [80], [81], [79]. Also the reactions of MeOH with HP to formic acid and methylformate shown in

Equation 3.3 have been reported by BASF without quantitative data [87].

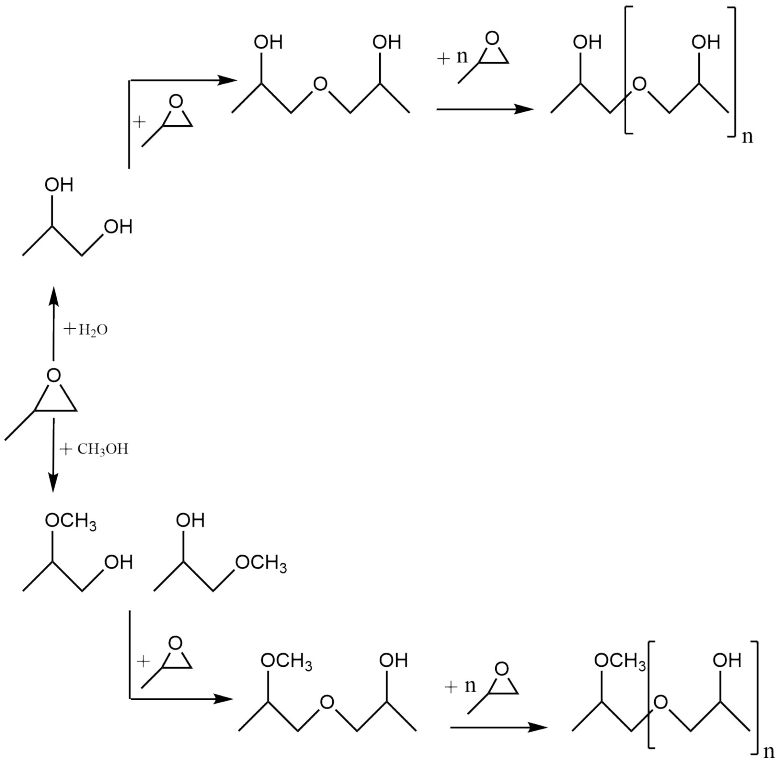

(3.2)

Methlyformate has a similar boiling point than PO which underlines a problem in the downstream purification steps. Also the decomposition of HP is a safety issue in industrial plant since Pr and oxygen can form explosive mixtures.

$$
\begin{aligned}
H_2O_2 &\longrightarrow 0.5O_2 + H_2O \\
CH_3OH{+}2H_2O_2 &\longrightarrow HCOOH + 3H_2O \\
CH_3OH{+}HCOOH &\longrightarrow HCOOCH_3 + H_2O
\end{aligned}
\tag{3.3}
$$

Only limited number of publications about the kinetics of the liquid phase selective oxidation of Pr to PO with HP over TS-1 can be found in the scientific literature. A summary of the available publications and their main parameters is shown in Table 3.1. Most publications focus on the main epoxidation reaction and do not provide rate law expression for the formation of side products. In all cases, the studies performed the reaction at conditions far from the one used in

industrial scale applications. In technical scale reactors both BASF/DOW and Evonik/Thyssenkrupp perform the epoxidation at pressures higher than 15 bar, condition at which Pr is in liquid phase [13], [15] which raises the question if these studies are representative of an industrial scale reactor.

Reference	Pressure [bar]	Pr phase	Reactor type	Considered Reactions	Solvent	Considered Models
1. [69]	0.7-7	Gas	Batch	Main	Methanol	L-H and E-R
2. [88]	—	—	Batch	Main and Side	Isopropanol	E-R
3. [89]	1-6	Gas	Batch	Main	Isopropanol	L-H and E-R
4. [90]	2-6	Gas	Fixed bed	Main	Methanol	L-H and E-R
5. [83]	3-5	Gas	Batch	Main and Side	Methanol	E-R
6. [91]	18-30	Liquid	Fixed bed	Main	Methanol	E-R
7. [84]	5-7	Gas	Fixed bed	Main and Side	Methanol	E-R

Table 3.1: List of relevant publications about HPPO kinetics E-R= Eley-Rideal, L-H= Langmuir-Hinshelwood

Several kinetic models have been tested for this reaction shown in Figure 3.6 and Figure 3.7. All derived models so far are based on the assumption that the rate determining step in the epoxidation reaction sequence is the reaction of Pr with the Ti-hydroperoxy active specie on the surface of the catalyst. Both Chadwick et.al [69] and Wang et.al [90] study the epoxidation reaction using as solvent MeOH in a batch and fixed bed reactors respectively at low pressure with Pr in gas phase. Based on different hypothesized reaction mechanism both tested an Eley-Rideal mechanism with HP being adsorbed on the surface of the catalyst and Pr reacting from the fluid phase and a Langmuir-Hinshelwood mechanism considering both single and dual active sites. on one hand, the model of Chadwick included the competitive adsorption of MeOH and the allowance for the enhancement of

Pr solubility depending on the water to MeOH ratio of the media. On the other hand, the model of Wang considered that the epoxidation reaction took place on TS-1 with adsorbed MeOH do to its high concentration and the competitive adsorption of PO in the derived rate law. Both studies excluded the adsorption of water due to the hydrophobicity of the TS-1 catalyst. After statistical analysis of the experimental data both publications arrived to different results. The study of Chadwick concluded that the best agreement was obtained with a dual site Langmuir-Hinshelwood mechanism, whereas Wang reported a better agreement with an Eley-Rideal mechanism with adsorbed HP and Pr reacting from the free phase. Additionally, Clerici et.al [80] observed that the reaction approximates zeroth-order behavior for high HP concentrations. Other publications studied the epoxidation reaction using as solvent isopropanol [88], [89] which is not the solvent used in industrial applications. The type of solvent used has an impact on the catalytic activity of the TS-1 catalyst [92], [89], [93], [94], therefore the results measured in isopropanol as media are not representative of an industrial scale process.

So far, only two publication provided rate law expression for the main epoxidation reaction and the formation of side products using as solvent MeOH. Both publications are based on an Eley-Rideal mechanism with Pr reacting from the fluid phase. Di serio et.al [83] studied the decomposition of HP, the main epoxidation reaction and the ring opening reactions in two batch reactors at pressures between 3-5 bar and 40°C with the catalyst shaped in to microspheres by spray-drying technique and suspended in the reactive mixture. In the case of Sulimov et.al [84], the epoxidation reaction was carried in a 15 mm diameter and 250 mm long fixed bed reactor at 30-60°C and 5-7 bar pressure. In this case, the catalyst powder was shaped into 2 mm diameter and 5 mm length extrudates using as binder aluminum 5,6-oxynitride. The reaction network considered in each publication and the derived rate laws are shown in Figure 3.8 and Table 3.2 respectively. In the case of the kinetic model derived by Di Serio, two different active sites have been considered. The first kind of active sites are the non-framework titanium open sites $Ti(SiO)_3OH$ and silanol groups Si-OH, also called "defective sites", which can catalyze the ring opening reactions of PO and form side products. The reaction rates of the defective sites are expressed by the reaction rates r_{d_1}, r_{d_2}, r_{d_3}

and r_{d_4} respectively. The second type of active sites are the framework $Ti(SiO)_4$ "effective sites" (or closed sites), which upon HP adsorption can catalyze not only the main epoxidation reaction but the ring opening reactions of PO as well. The reactions on the Ti effective sites are expressed by the rates r_1(TS-1), $r^*_{d_1}$(TS-1), $r^*_{d_2}$(TS-1), $r^*_{d_3}$(TS-1), $r^*_{d_4}$(TS-1). Also the competitive adsorption of PO, Pr and water on the Ti effective sites are considered. The isomers of methoxypropanol 1-MPOL and 2-MPOL were measured as a single component which is the sum of both, this component is referred as methoxypropanol (hereafter MPOL). Additionally further reactions of MPOL with PO to form di-methoxypropanol and oligomers were considered.

In the publication by Sulimov, no distinction between the different active species on the catalyst surface has been made and the rates r_1, r_2, r_3, r_4, r_5 have been derived assuming the catalyst surface homogeneous. Both isomers of methoxypropanol are measured separately and rate laws for each one of them were derived. The competitive adsorption of water and Pr on the Ti effective sites are considered negligible. Both publications arrive to similar results for the main epoxidation reaction in terms of activation energy which is about $4,50e4\ [J\,mol^{-1}]$. A straight forward comparison for the side products formation is not possible due the different mechanism of reaction assumed in each publication. While Di Serio proposed that side reactions on the Ti effective sites are promoted by the reaction of surface species formed by the adsorption of PO on $Ti \bullet OOH$ species, in the case of Sulimov, side reactions are promoted by surface species formed by the adsorption of PO on $Ti \bullet CH_3OH$ species. This can be reflected by the fact that the side products rate laws derived by Sulimov does not include the adsorption constant and concentration of HP.

A comprehensive publication that provides kinetic data and derived rate law expressions for the main epoxidation reaction and the formation of side products under industrial conditions with Pr in liquid phase still has not been published.

$$S + CH_3OH \overset{K_{CH_3OH}}{\rightleftharpoons} S^* \qquad S + CH_3OH \overset{K_{CH_3OH}}{\rightleftharpoons} S^*$$

$$S^* + H_2O_2 \overset{K_{H_2O_2}}{\rightleftharpoons} S^* \bullet H_2O_2 \qquad S^* + C_3H_6 \overset{K_{C_3H_6}}{\rightleftharpoons} S^* \bullet C_3H_6$$

$$S^* \bullet H_2O_2 + C_3H_6 \underset{k_r}{\overset{r_r}{\rightleftharpoons}} S^* \bullet C_3H_6O + H_2O \qquad S^* \bullet C_3H_6 + H_2O_2 \underset{k_r}{\overset{r_r}{\rightleftharpoons}} S^* \bullet C_3H_6O + H_2O$$

$$S^* \bullet C_3H_6O \overset{K^{-1}_{C_3H_6O}}{\rightleftharpoons} S^* + C_3H_6O \qquad S^* \bullet C_3H_6O \overset{K^{-1}_{C_3H_6O}}{\rightleftharpoons} S^* + C_3H_6O$$

Figure 3.6: Eley-Rideal mechanisms (left) HP adsorbed, Pr free. (right) Pr adsorbed, HP free

$$S + ROH \overset{K_{ROH}}{\rightleftharpoons} S^* \qquad S_1 + ROH \overset{K^1_{ROH}}{\rightleftharpoons} S_1^*$$

$$S^* + H_2O_2 \overset{K_{H_2O_2}}{\rightleftharpoons} S^* \bullet H_2O_2 \qquad S_2 + ROH \overset{K^2_{ROH}}{\rightleftharpoons} S_2^*$$

$$S^* + C_3H_6 \overset{K_{C_3H_6}}{\rightleftharpoons} S^* \bullet C_3H_6 \qquad S_1^* + H_2O_2 \overset{K_{H_2O_2}}{\rightleftharpoons} S_1^* \bullet H_2O_2$$

$$S^* \bullet H_2O_2 + S^* \bullet C_3H_6 \underset{k_r}{\overset{r_r}{\rightleftharpoons}} S^* + S^* \bullet C_3H_6O + H_2O \qquad S_2^* + C_3H_6 \overset{K_{C_3H_6}}{\rightleftharpoons} S_2^* \bullet C_3H_6$$

$$S^* \bullet C_3H_6O \overset{K^{-1}_{C_3H_6O}}{\rightleftharpoons} S^* + C_3H_6O \qquad S_1^* \bullet H_2O_2 + S_2^* \bullet C_3H_6 \underset{k_r}{\overset{r_r}{\rightleftharpoons}} S_1^* + S_2^* \bullet C_3H_6O + H_2O$$

$$S_2^* \bullet C_3H_6O \overset{K^{-1}_{C_3H_6O}}{\rightleftharpoons} S_2^* + C_3H_6O$$

Figure 3.7: Langmuir-Hinshelwood mechanisms (left) HP and Pr adsorbed on a single active site. (right) HP and Pr adsorbed on different active sites

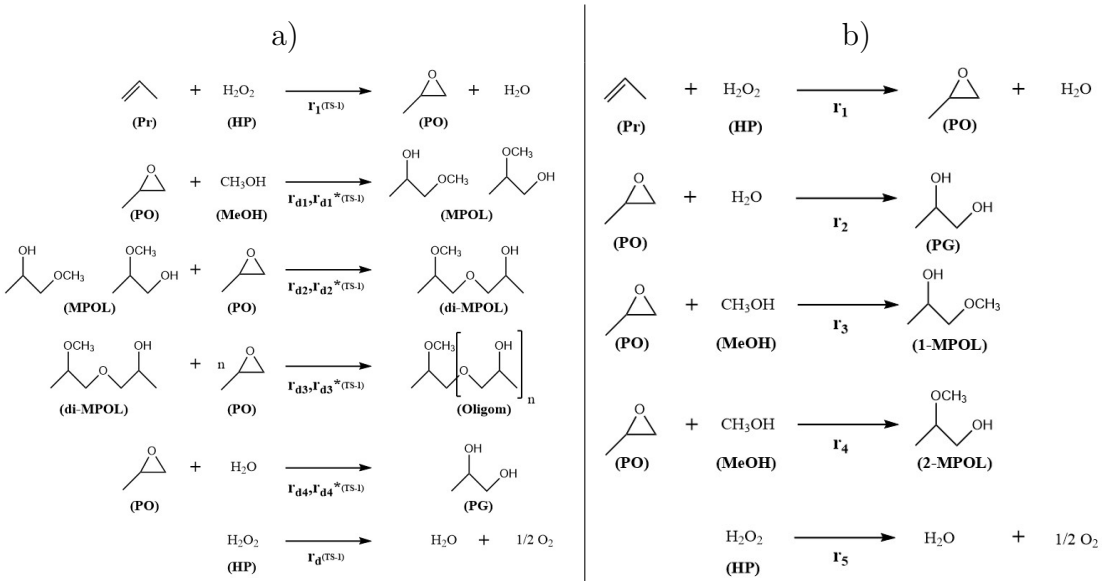

Figure 3.8: Reaction network and chemical species considered by a) Di Serio [83] b) Sulimov [84]

3.2.4 Reaction mechanism of the (HP-PO) reaction

Both in the scientific literature and the patent library only the mechanism for the main reaction of the (HP-PO) process has been studied. Through the years, significant effort has been made to measure and identify the detailed structure of the intermediates involved in the epoxidation reactions with HP over TS-1 catalyst. There is general agreement that the key factor for the epoxidation is the adsorption of HP on the Ti center forming a Ti-peroxo complex that reacts with Pr to form PO and water. Nevertheless, the nature and structure of these intermediates is still under debate.

The first insight into the structure of the Ti sites on the TS-1 catalyst was provided by Boccuti et.al [95]. By combining both IR and UV-vis reflectance spectroscopy was observed that the Ti sites are constituted by tetrahedral [TiO_4] units while previously proposed titanyl structures were unlikely [96]. In 1992 Clerici et.al [97] proposed the involvement of tetrahedral $Ti(SiO)_4$ framework units as active sites for the epoxidation reaction with HP on TS-1. Based on ^{17}O-, ^{18}O-labeled water MAS NMR and IR spectra was shown that the key factor for the epoxidation reaction is the reversible splitting of one Ti-OSi bond by HP with the resulting

Table 3.2: Kinetic models by Sulimov and Di Serio

1. **Model by Sulimov [84]**

$$r_1 = \frac{k_1 K_{H_2O_2} [H_2O_2] [C_3H_6] \rho_{bed}}{1 + K_{H_2O_2} [H_2O_2] + K_{C_3H_6O} [C_3H_6O]}$$

$$r_2 = \frac{k_2 K_{C_3H_6O} [C_3H_6O] [H_2O] \rho_{bed}}{1 + K_{H_2O_2} [H_2O_2] + K_{C_3H_6O} [C_3H_6O]}$$

$$r_3 = \frac{k_3 K_{C_3H_6O} [C_3H_6O] [CH_3OH] \rho_{bed}}{1 + K_{H_2O_2} [H_2O_2] + K_{C_3H_6O} [C_3H_6O]}$$

$$r_4 = \frac{k_4 K_{C_3H_6O} [C_3H_6O] [CH_3OH] \rho_{bed}}{1 + K_{H_2O_2} [H_2O_2] + K_{C_3H_6O} [C_3H_6O]}$$

$$r_5 = \frac{k_5 K_{H_2O_2} [H_2O_2] \rho_{bed}}{1 + K_{H_2O_2} [H_2O_2] + K_{C_3H_6O} [C_3H_6O]}$$

a. Van 't Hoff equation for adsorption constants

$$K_i = K_{i^\circ} * exp^{\left(\frac{H_i}{R*T}\right)}$$

2. **Model by Di Serio [83]**

a. Reactions in Ti-OOH sites

$$r_1 = \frac{k_1 K_{ads_1} [H_2O_2] [C_3H_6] \rho_{bed}}{1 + K_{ads_1} [H_2O_2] + K_{ads_2} [C_3H_6] + K_{ads_3} [H_2O] + K_{ads_4} [C_3H_6O]}$$

$$r_{d1^*} = \frac{k_{d1^*} K_{ads_1} [H_2O_2] [C_3H_6O] [CH_3OH] \rho_{bed}}{1 + K_{ads_1} [H_2O_2] + K_{ads_2} [C_3H_6] + K_{ads_3} [H_2O] + K_{ads_4} [C_3H_6O]}$$

$$r_{d2^*} = \frac{k_{d2^*} K_{ads_1} [H_2O_2] [C_3H_6O] [MPOL] \rho_{bed}}{1 + K_{ads_1} [H_2O_2] + K_{ads_2} [C_3H_6] + K_{ads_3} [H_2O] + K_{ads_4} [C_3H_6O]}$$

$$r_{d3^*} = \frac{k_{d4^*} K_{ads_1} [H_2O_2] [C_3H_6O] [H_2O] \rho_{bed}}{1 + K_{ads_1} [H_2O_2] + K_{ads_2} [C_3H_6] + K_{ads_3} [H_2O] + K_{ads_4} [C_3H_6O]}$$

$$r_{d4^*} = \frac{k_{d4^*} K_{ads_1} [H_2O_2] [C_3H_6O] [Oligom] \rho_{bed}}{1 + K_{ads_1} [H_2O_2] + K_{ads_2} [C_3H_6] + K_{ads_3} [H_2O] + K_{ads_4} [C_3H_6O]}$$

b. Reactions in Ti-OH and Si-OH sites

$$r_{d1} = k_{d1} [C_3H_6O] [CH_3OH] \rho_{bed}$$

$$r_{d2} = k_{d2} [C_3H_6O] [MPOL] \rho_{bed}$$

$$r_{d3} = k_{d3} [C_3H_6O] [H_2O] \rho_{bed}$$

$$r_{d4} = k_{d4} [C_3H_6O] [Oligom] \rho_{bed}$$

$$r_d = k_d [H_2O_2] \rho_{bed}$$

c. Modified Arrhenius equation with T_{ref} = 313.15 K

$$k_i = k_{i_{ref}} * exp^{\left(\frac{E_i}{R} * \left[\left(\frac{1}{T_{ref}}\right) - \left(\frac{1}{T}\right)\right]\right)}$$

formation of a $Ti \bullet OOH$ specie and the coadsorption of one alcohol or water molecule stabilizing the hydroperoxide through a five-membered ring shown in Figure 3.10 a). The epoxidation step takes place when the peroxy oxygen vecinal to the Ti attacks the double bond of Pr forming PO and a molecule of water. The catalytic cycle is completed with the desorption of the epoxide and the subsequent adsorption of HP on the tetrahedral $Ti(SiO)_4$ framework units to form again a $Ti \bullet OOH$ specie. The activity of the TS-1 was observed to be solvent dependent due to the role of the protic molecule in stabilizing the five-membered ring. Steric crowding inside the 0.5-0.6 nm pores of the TS-1 catalyst is dependent on the size of the solvent molecule which increases with the nature of the R-OH molecule used as media. Being MeOH the smallest alcohol molecule available, it is more likely to reach the Ti center and stabilize the five-membered ring were the epoxidation reaction takes place which results in a higher catalytic activity when compared with other solvents [92], [89], [93], [94]. Further investigation showed that when TS-1 catalyst is exposed to water, one $Si - O - Ti$ bridge will be hydrolyzed and defective species $Ti(SiO)_3OH$ will dominate the catalyst surface on hydrous conditions [98], [99], [100]. Based on this, defective $Ti(SiO)_3OH$ species were proposed as the actual catalytic sites [101], [64], [102].

In contrast to IR spectroscopy, when using UV-vis Raman spectroscopy there is no characterization problem caused by the presence of H_2O which is typically present in HP solutions. If the Raman experiment is performed using a exciting wavelength coincident or near to the wavelength of an electronic adsorption of the sample, such as a transition metal atom, a resonance effect can be achieve. Under these circumstances, the vibrational features of the immediate vicinity of the absorbing atom can be enhanced several orders of magnitude. This is particularly useful in the case of the TS-1 catalyst due to the high dilution of Ti centers into the MFI framework which is typically less than 3% [63]. By implementing this technique Bordiga et.al [103] in 2003, measured the resonance effect of the Ti center of the TS-1/H_2O/H_2O_2 system. Upon interaction with H_2O/H_2O_2 TS-1 shows an electronic adsorption at 385 nm due to the ligand to metal charge transfer between a neighbor oxygen to the central Ti atom. By using a exciting wavelength of 442 nm near the wavelength of the electronic adsorption a strong new band at 618 cm^{-1} shown in Figure 3.9 was observed. This band is attributed to the

Raman enhanced vibrational mode of the $Ti(O)_2$ ring which constitutes further experimental evidence for the formation of a $Ti \bullet OOH$ complex.

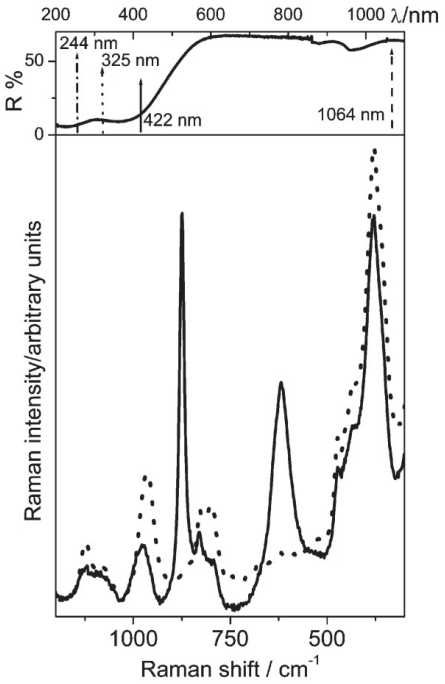

Figure 3.9: Resonance effect on the Ti-peroxo complex in a the TS-1/H_2O/H_2O_2 system taken from [103]: (Top) UV-vis diffusive reflectance spectroscopy spectra showing the electronic adsorption of the sample at 385 nm do to the ligand to metal charge transfer. (Bottom) Raman spectra measured with a 442 nm laser line before and after interaction with H_2O/H_2O_2, doted and solid lines respectively

Later on in 2012 Xiong et.al [101] supported by UV-vis Raman spectroscopy and DFT simulations, reported that rather than a five-membered ring a six-coordinated $Ti \bullet OOH$ center shown in Figure 3.10 b) is responsible for the epoxidation reaction. Additionally, 3 types of defective $Ti(SiO)_3OH$ sites shown on Figure 3.11 were proposed as Ti species in which $Ti \bullet OOH$ species can be formed. In the TS-1/HP/H_2O/CH_3OH Raman spectra a new band at 836 cm^{-1} was assigned to the O-O stretching of the 6-coordinated $Ti \bullet OOH$ (η^2) intermediates. By continuously flowing Pr through the reaction cell, a direct consistency between the intensity of the band at 836 cm^{-1} and the concentration of produced PO measured by GC was observed. The spectra of adsorbed Pr was not observed when HP was dropped on

the TS-1 sample in advance. This may be because water and peroxo species on the surface of the catalyst prevents the adsorption of Pr. Another possibility, is that Pr is adsorbed on the 6-coordinated $Ti \bullet OOH$ species but reacts very fast. Therefore, the concentration adsorbed Pr on the surface of the catalyst is very low and cannot be detected by Raman Spectroscopy. The five-membered ring proposed by Clerici was not detected in this work. Additionally, several density functional theory (DFT) studies have shown that the reaction occurs via a sequential pathway in which HP dissociatively adsorbs forming a hydroperoxy intermediate and a molecule of water that remains coordinated forming a $Ti \bullet OOH \bullet H_2O$ active complex. Then, weakly adsorbed Pr reacts via proximal oxygen abstraction as shown in Figure 3.12. The computational calculations showed that the formation of the hydroperoxo intermediate $Ti \bullet OOH \bullet H_2O$ by the adsorption/dissociation of HP is the rate determining step of the mechanism [104], [105], [106], [107].
Most recently in 2020, Gordon et.al [107] supported by $H_2{}^{17}O_2$ labeled solid state NMR and DFT simulations proposed that di-nuclear Ti sites shown in Figure 3.10 c) are more active and selective for the epoxidation of Pr than Ti(IV) isolated atoms in the framework of TS-1. This work does not claim that isolated Ti sites are not effective in the selective oxidation of Pr but rather emphasizes that di-nuclear Ti sites have superior performance and should be prepared by novel synthesis strategies. Even though there is general agreement that the active site for the epoxidation of Pr over TS-1 is formed by the adsorption of HP on a Ti center, the details of this intermediate is still under debate. Moreover, these studies are often performed far from industrial conditions. A detailed mechanistic study that includes experimental data about the intermediates formed not only for the main epoxidation reaction but also by the side reaction under industrial conditions is still not available in the literature.

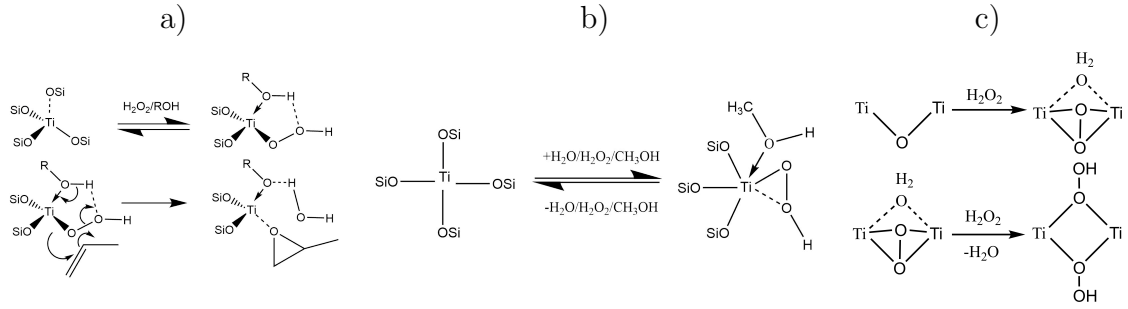

Figure 3.10: a) Five membered ring active site proposed by Clerici et. al. [97] b) 6-coordinated active site proposed by Xiong et. al. [108] c) Di-nuclear active site proposed by Gordon et. al. [107]

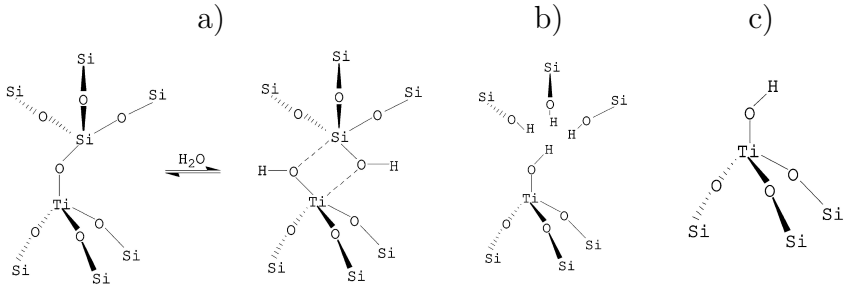

Figure 3.11: Three defective active sites proposed by Xiong et. al. [108]. a) Defective site from hydration of perfect tetrahedral $Ti(SiO)_4$, b) Defective site located in a Si vacancy c) Defective site located on the surface of the catalyst

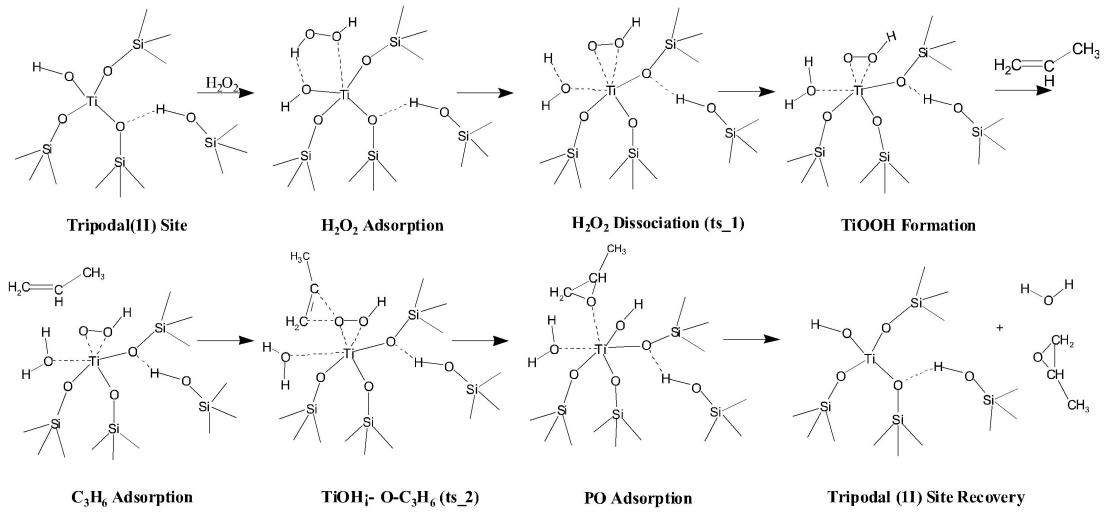

Figure 3.12: DFT stepwise mechanistic scheme of Pr epoxidation on tripodal (1I) site of TS-1 catalyst. Taken from [106]

.

3.2.5 Effects of reaction conditions: solvent, temperature and pressure

There is a general agreement that the protic solvent plays an important role in the stabilization of the $Ti \bullet OOH$ active specie, which explains the dependence of the catalytic activity on the media used. Several researches have shown that the best solvent is MeOH which has an effect in both epoxidation rate and PO selectivity [89], [93], [94], [92]. This can be explain by steric crowding inside the 0.5-0.6 nm pores of the TS-1 catalyst. Being MeOH the smallest alcohol molecule available, it is more likely to reach the Ti center and stabilize the active $Ti \bullet OOH$ specie. On Figure 3.13 the influence of different reaction media in the epoxidation is shown.

The temperature of reaction has to be carefully controlled since it has an impact on the HP conversion and PO selectivity. In the range of 30-50°C the HP conversion increases 1.3 times whereas PO selectivity decreases from 99% to 96% [69], [80]. An increase in the temperature increases the rate of formation of side products and in consequence decreases the selectivity of PO. Degussa (currently Evonik AG) reported the formation of hot spots inside of their packed bed reactor, the rate of heat generation is such that is not possible to operate the reaction under isothermal conditions on this type of reactor [109]. Also the reaction pressure has an impact on the reaction rate. On one hand, a high pressure increases the solubility of gaseous Pr in the reaction media. On the other hand, further increase causes the liquefaction of Pr. Therefore, the reaction system comprises either a gas-liquid-solid phase, liquid-solid phase or liquid-liquid-solid phase system depending on the concentration of Pr in the mixture. Upon liquefaction the point at which a secondary liquid phase is formed is given by the composition of the mixture as shown in the liquid-liquid equilibrium ternary diagram for the Pr/MeOH/Water mixture in Figure 3.14. The liquefaction pressure of Pr at 40 °C is 16 bar, therefore, HP-PO commercial processes usually operate at pressure higher than 16 bar and in a liquid-liquid-solid regime to ensure that the reactive phase is always saturated with Pr [13], [15].

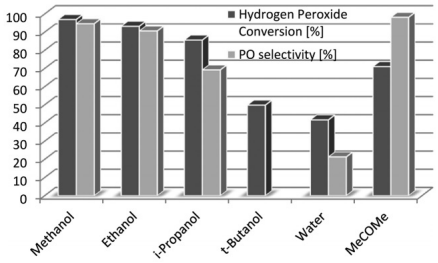

Figure 3.13: Influence of different reaction media on the epoxidation of Pr (taken from [92])

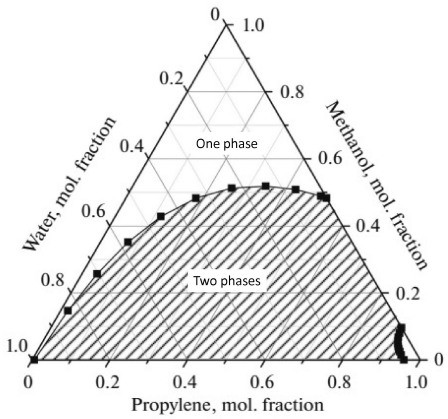

Figure 3.14: LLE diagram for the Pr-MeOH-Water mixture at 40°C (taken from [110])

3.3 Periodic Open Cell Structures (POCs)

An optimal design of a catalytic reactor considers the coupling between reaction kinetics and transport properties at both macro and micro scales. For applications that use solid catalysts fixed bed reactors are often preferred in the industry. In this reactor configuration, transport properties are controlled by the flow rate, pellets shape and the tube-to-particle size ratio. In this sense randomly packed bed features point-to-point contacts between each other or with the reactor wall, moreover, the materials often applied as catalyst support such α-alumina, γ-alumina, silica, titania and carbon have low thermal conductivity. To avoid losses of activity, selectivity and possible thermal runaway the reactors are operated at high specific mass flow rates to enhance the convective heat transfer [111]. This has an impact in both the pressure drop and the reactor design since longer tubes are needed to reach a significant conversion in kinetically limited processes. As alternative, catalyst beds are diluted with thermally conductive inert material to reduce the thermal load by diluting the active phase. In the specific case of the industrial scale epoxidation of Pr with HP over TS-1 catalyst both BASF/DOW and Evonik/Thyssenkrupp developed different technical solution to overcome the losses of activity and selectivity due to the formation of hotspots inside the catalyst bed. In the case of BASF/DOW, the epoxidation reaction is carried in a 2 step tubular fixed bed reactor with intermediate PO removal [62], [13], while

Evonik/Tyssenkrupp performs the reaction in a patented plate bundle reactor for efficient heat removal [61].
As a potential solution for process intensification structured reactors have been proposed due to the possibility of tailoring the transport properties of the catalytic reactor [112], [113]. Typical structured reactors are open-foam cells, honeycombs monoliths and most recently Periodic open cell structures. The characteristics and properties of these types of structured reactors are summarized in Figure 3.15.

	Randomly packed bed	Open-cell foam	Periodic open cellular structures	Honeycomb
State	state-of-the-art	development	research	state-of-the-art
	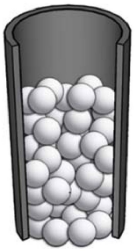		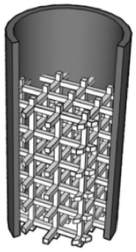	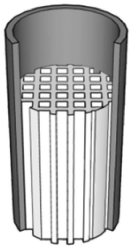
Flow pattern	crossmixed	crossmixed	crossmixed	no crossmixing
Radial transport				
- mass	high	high	high	none
- heat	low	high	high	high
Pressure drop	high	low	low	low
Morphology	irregular	irregular	regular	regular
Design freedom	barely	barely	high	barely

Figure 3.15: Comparison of different packed reactors and their properties taken from [114]

Additively manufactured POCs represent a new class of structured catalyst bed that can be designed with an almost unlimited range of different geometries when combined with computer design (CAD) and modern additive manufacturing methods (3D printing). Several parameters can be optimized for a particular application, namely, unit cell type, strut diameter d_s, cell length l_c, window diameter d_w and strut length l_s as shown in Figure 3.16. These parameters defines the volume-specific surface area and the external porosity of the structured POCs catalyst

bed. POCs exhibit interesting heat transfer and hydrodynamic properties compared with conventional packed catalyst beds [114], [115]. Ambrosetti et.al [116] showed that at low superficial mass velocities POCs made of highly conductive materials can offer a more effective heat transport when compared with randomly packed beds. This improvement on the heat transport shown on Figure 3.16 can be explained by the fact that at low superficial mass fluxes $(G)[kg\,m^{-2}\,s^{-1}]$, heat conduction dominates over heat convection, and therefore the enhanced thermal conductivity of the POCs and its interconnected matrix is able to provide an effective heat transport from the center of the reactor towards the cooled wall even at low superficial mass velocities. This feature is of particular importance in kinetically limited processes, since POCs offers the possibility of operating the reactor at low specific mass flow rates while still providing enough heat transfer to minimize losses of activity, selectivity, possible thermal runaways and reducing the reactor footprint.

Empirical correlations for assessing the thermal performance of POCs are avail-

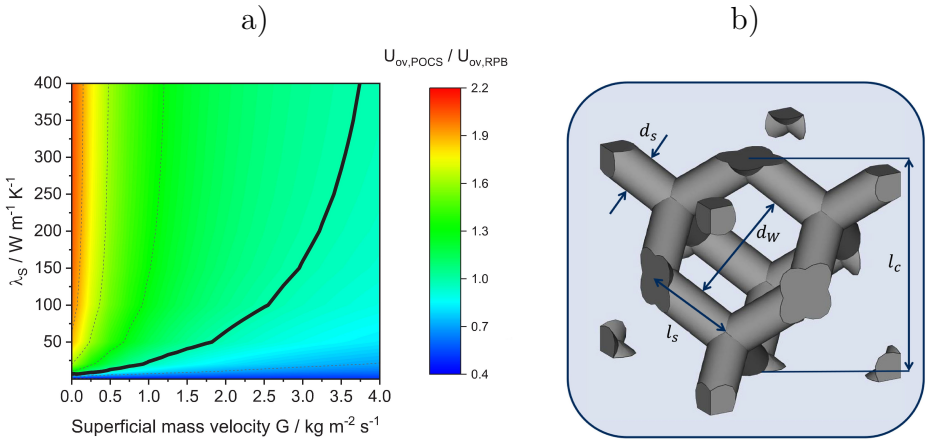

Figure 3.16: a)Comparison of the overall heat transfer coefficient of a diamond POCS and a randomly packed bed. b) Diamond unit cell with important geometric properties strut diameter d_s, cell length l_c, window diameter d_w, and strut length l_s. Figures taken from [116]

able in the literature, these correlations are based on the assumption that the macroscopic properties of the structure are determined by those of a representative unit cell. Then, the thermal properties of the POCs are lumped in a effective thermal conductivity term as shown in Equation 3.4.

$$\Lambda_r = \lambda_0 + \lambda_{rad} + \lambda_d \tag{3.4}$$

Where (Λ_r) is the effective radial thermal conductivity and (λ_0), (λ_{rad}), (λ_d) are the stagnant, radiative and dispersive thermal conductivities of the POCs. Radiation can be neglected for low temperature applications, therefore is not further discussed in this work. The stagnant thermal conductivity (λ_0) accounts for the contribution without fluid flow and depends strongly on the thermal conductivity of the solid material, the solid fraction and the material distribution along the strut. Bianchi et. al [115] reported that besides the obvious contribution of the solid fraction on the stagnant thermal conductivity, no significant effect was observed upon changing the geometry of the unit cell or the strut cross section. In this sense, the best thermal heat transfer performance was observed in cells that feature struts with constant cross section. Based on this observation Bianchi proposed a correlation shown in Equation 3.5 to estimate the maximal effective thermal conductivity that can be achieved at a given solid fraction for an ideal unit cell.

$$\lambda_0 = \frac{1-\epsilon_T}{\tau}\lambda_S \qquad \tau = (0.36 + [0.64(1-\epsilon_T)])^{-1} \tag{3.5}$$

Where (λ_S) is the thermal conductivity of the POCs material, (ϵ_T) is the total porosity and (τ) is the heat tortuous path through the cellular structure. The porosity can be estimated experimentally by standard pycnometry or analytically by the Klumpp equation [117], as shown in Equation 3.6.

$$\epsilon_T = 1 - \frac{3\frac{\pi}{4}\phi + K_N}{(\phi+1)^3} \qquad K_N = \frac{3}{4}\pi - \sqrt{2} \qquad \phi = \frac{l_w}{d_s} - 1 \tag{3.6}$$

Where (l_w) is the cell window length and (d_s) is the strut diameter. The morphology of the cell has an impact in the dispersive thermal conductivity (λ_d), nevertheless it as been found that this term has only limited influence on the resulting effective thermal conductivity (Λ_r) specially for highly conductive materials, and for this reason it has not been extensively investigated. Most publications proposed a linear dependency with the flow, mostly correlated by the Peclet

number [118], [119], [120]:

$$\frac{\lambda_d}{\lambda_f} = \frac{Pe_x}{K_r}$$

Where (x) represents a characteristic length and (K_r) is the radial dispersion coefficient which vary depending on the correlation used. Additionally, it has been found that the degree of coupling between the POCs and the wall of the reactor can have a significant role in assessing the heat transfer performance of a cellular structure. It has been reported 100% wall coupling can increase the heat transport by 3.5 fold when compared with an uncoupled structure [114]. Unfortunately, the determination of the wall heat transfer coefficient is associated with a high degree of uncertainty and correlations from the literature can have a broad range of error up to 40%. Correlations from the literature are based on a Nusselt-Reynolds approach [120], [121], [122], [123].

$$\frac{\alpha_w x}{\lambda_f} = Nu_{w,0} + Nu_{w,conv} = A + B\,Re_x^c$$

Where the $(Nu_{w,0})$ is the stagnant contribution which accounts for the conduction in the gap between structure and wall and $(Nu_{w,conv})$ is the dynamic contribution which describes the convective transport expressed as a function of the Reynolds number from which the characteristic length (x) depends on the correlation used for the estimation.

Due to these interesting properties, applications of POCs have been recently reported for the process intensification of NO oxidation [124] and for COx methanation [125], [126]. Additionally in the case of gas-liquid reactions, additively manufactured periodic open cells offer the opportunity of not only enhancing the heat transport but also of locally influencing the gas holdup and bubble distribution by locally tailoring the cell geometry [127], [128].

3.4 Spatial profile reactors

Several types of experimental reactor such as batch, semi-batch, continuous stirred tank reactors and plug flow reactor have been implemented for the measurement of catalytic reactions [129]. The rates are determined by measuring the changes of

concentration of chemical species or conversion, as a function of a property related to the amount of catalyst for a given set of reaction conditions (T,P) as shown in Equation 3.7.

$$R_{j,x} = \left(\frac{1}{\nu_i Q}\right)\frac{dn_i}{dt} \tag{3.7}$$

In the case of heterogeneous solid catalyst the amount Q is typically the mass of catalyst which is related to the volume of the reactor by the bulk density of the catalyst.

In a typical experimental test, a well measured mass of catalyst is loaded into the reactor with controlled internal conditions of pressure and temperature (P_0, T_0). The reactants are mixed and fed to the reactor $(C_{i,0}, \dot{V} = \sum \dot{V}_{i,0})$ where they are transformed into products. Then, the effluents of the reactor are measured by an analytical method to determine the change in concentration $(P_{out}, T_{out}, C_{i,out}, \dot{V_{out}} = \sum \dot{V}_{i,out})$ of the chemical species. Typically, the reactor is operated in differential mode with conversion lower than 5% , which allows the assumption that the rate of reaction is constant. Isothermal behavior is assumed $(T_0 = T_{out})$ to allow the assignment of the measured rates to the inlet concentrations. Differential conditions at high conversion can be achieve by implementing an integral reactor to achieve the desired conversion followed by a differential reactor. To investigate the reaction network the contact time $\tau = \frac{V_{cat}}{\dot{V}}$ has to be varied systematically which underlines and extensive amount of experimental work. Then, species consumption (R_i), production, reaction rates (r_j), reactants conversions (X_i), product selectivities $(S_{k,i})$and yields $(Y_{k,i})$ can be calculated from the difference between inlet and outlet variables.

$$r_j = \frac{\dot{n}_{i,out} - \dot{n}_{i,0}}{m_{cat}} \qquad X_i = \frac{\dot{n}_{i,o} - \dot{n}_{k,out}}{\dot{n}_{i,0}}$$

$$R_i = \sum_{j=1}^{j=m} \nu_{i,j} r_j \qquad S_{k,i} = \frac{\dot{n}_{k,0} - \dot{n}_{k,out}}{\dot{n}_{i,0} - \dot{n}_{i,out}} \frac{\nu_i}{\nu_k}$$

$$Y_{k,i} = X_i S_{k,i}$$

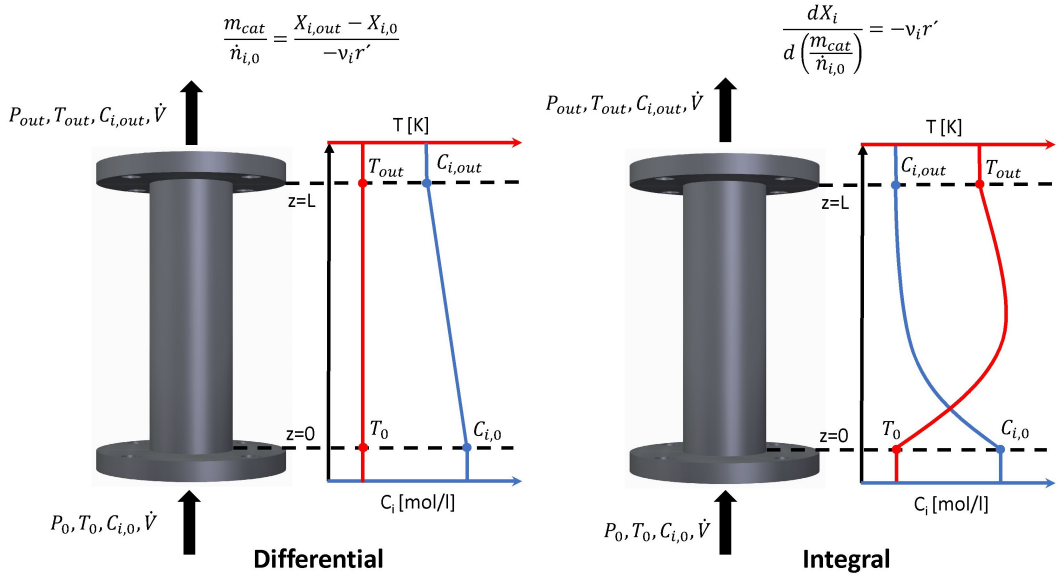

Figure 3.17: Differential and Integral experimental fixed bed reactors

The variables (R_i), (r_j), (X_i), $(S_{k,i})$ and $(Y_{k,i})$ depend on the values measured at the outlet and inlet of the reactor. In the case of the differential reactor, the gradients inside the reactor are considered negligible and the environment is assumed to be homogeneous across the catalyst bed. The drawback of this approach is that low conversions are not representative of the true operating conditions of an industrial application. Consequently, kinetic relationships derived from differential data can have limited applicability in broader applications outside the narrow range of analysis. In the case of an integral reactors, the concentration of reactants and products change significantly between the inlet and outlet of the reactor. In this case, the reaction rate changes across the length of the catalytic bed, and in consequence it is not possible to assign the measured reaction rate to the inlet variables. Moreover, the structure of the catalyst is modified by the local chemical potential of the reaction environment which changes widely across the reactor length. This local changes cannot be measured by inlet-outlet experimental approaches.
In experimental fixed bed reactors, time dependent changes of concentrations and temperature are translated into spatial variables. Under steady state conditions axial gradients provide information about the mechanism of reaction without the need of expensive isotopes typically used on transient experiments [130], [131],

[132]. The measurements of a spatially resolved profile is defined as the determination of kinetically relevant variables within the catalyst bed such as molar concentration of species or molar flow rates ($C_i(z)$), ($n_i(z)$) and temperature in the fluid phase ($T_f(z)$) as a function of the spatial coordinate (z). For the measurement of spatially resolved profiles within a reactor several approaches have been developed. The principle is based on the continuous movement of a thin sampling capillary along the axis of the reactor. This capillary continuously transfers a sample of the current position to an analytical device for analysis. The most robust and widely applied technique to measure spatial profiles inside catalytic fixed-bed reactors is the minimally invasive capillary sampling technique. This technique was developed independently and in different embodiments by various groups [7], [8], [9]. A comprehensive review of the evolution, as well the advantageous capabilities of spatially resolved techniques for the characterization of heterogeneously catalyzed reactions was published by Morgan et.al [133]. The spatially resolved capillary-inlet mass spectroscopy system (SpaciMS) shown in Figure 3.18 developed by Partridge et.al [7], [8] was used to resolve spatial profiles of chemical species and temperature in straight channels monoliths. In the Paul Scherrer Institute Bosco and Vogel [9] measured spatially resolved profiles of the CO methanation in a catalytic plate reactor with optical access shown in Figure 3.19. In contrast to the fore mentioned applications, the minimal invasive spatial sampling technique by Horn et.al [12], [4] uses a closed capillary design with a side sampling orifice. This design provides the sampling capillary enhanced mechanical stability, which opens a wide spectrum of applications in heterogeneous catalysis, most specifically in the measurement of spatially resolved kinetic and spectroscopic gradients in packed bed reactors where an open ended capillary would bend or break due to friction with the catalyst particles. A illustration of the measurement principle by Horn is shown in Figure 3.20. The sampling system is constituted by a sampling capillary (typically OD=0.8 mm) with a side orifice of 50-100 μm. A sample of the flow running continuously through the catalyst bed can be taken through the side orifice by applying a difference of pressure. Usually, the amount of sample is about 5-10% of the total flow to avoid disturbing the flow inside the reactor. The sample flow can be continuously directed to an analytical device, typically a Gas Chromatograph or a Mass Spectrometer for local

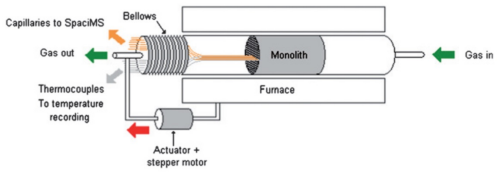

Figure 3.18: Sketch of SpaciMS Instrument (taken from [8])

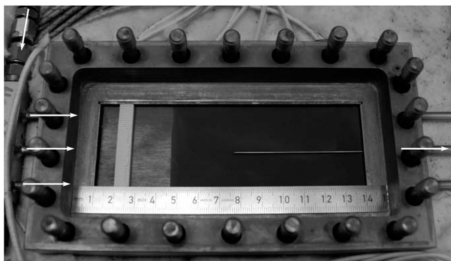

Figure 3.19: Picture of opened channel reactor with catalyst plate(taken from [9])

identification and quantification of chemical species. For the measurement of the fluid phase temperature, a thermocouple (usually 250-500 μm) is inserted inside the capillary and tip aligned with the sampling orifice. In this way it is possible to measure both the local concentration of species ($C_i(z)$) and temperature ($T(z)$) at the position were the orifice is located. Optionally, a pyrometer or a optical fiber can be used to measure either the temperature of the solid phase ($T_s(z)$) in case of high temperature reactions or spectroscopic information of surface species ($I_s(z)$) [12], [11]. Then, the sampling probe is translated along the axial coordinate (z) by a high precision step motor. Spatially resolved concentration and temperature profiles can be constructed by measuring at multiple positions along the reactor coordinate. Then, the conversion (X_z), selectivity (S_z) and differential rate $\left(r_{j_z}^{m_{cat}}\right)$ as a function of the coordinate (z) can be calculated as follows:

$$X_z = \frac{[C_i]_0 - [C_i]_z}{[C_i]_0} \times 100\%$$

$$S_z^k = \frac{[C_k]_0 - [C_k]_z}{[C_i]_0 - [C_i]_z} \frac{\nu_i}{\nu_k} x100\%$$

$$r_{j_z}^{m_{cat}} = \frac{1}{\nu_{ij}} U_0 \frac{\left(C_{ij_{z+\Delta z}} - C_{ij_z}\right)}{\Delta z} \frac{1}{\rho_{bed}}$$

Where ($r_{j,z}^{m_{cat}}$) is the mass based differential reaction rate of the reaction j at the position (z) in $[mol\ kg^{-1}\ s^{-1}]$, ν_{ij} is the stoichiometric coefficient of the specie i in the reaction j, C_{ij_z} is the concentration of the specie i in the reaction j at the coordinate (z) in $[mol\ m^{-3}]$, (U_0) is superficial flow velocity in $[m\ s^{-1}]$ and

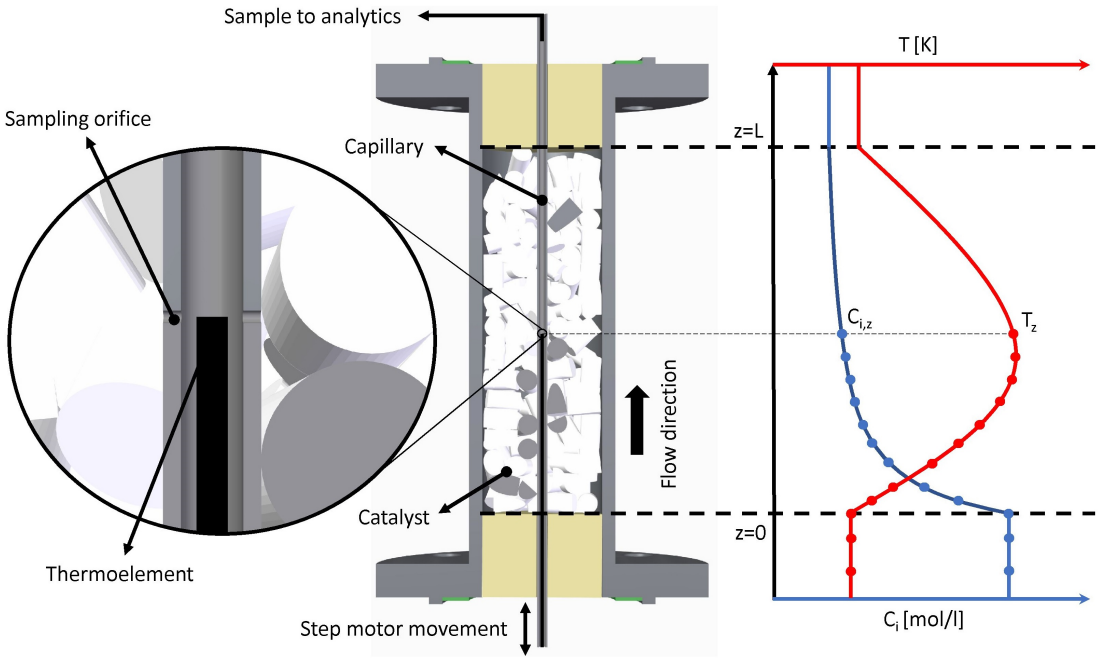

Figure 3.20: Spatial sampling principle by Horn: (Left) Magnified view of sampling arrangement for measurement of local concentration and temperature. (Center) Sectional view of a experimental spatial fixed bed reactor. (Right) Spatially resolved concentration and temperature profile.

(ρ_{bed}) is the bulk density of the catalyst bed in $[kg\ m^{-3}]$. The accuracy of the analytical method applied to measure the concentration of chemical species can have a big impact when calculating the differential rate of reaction. In this case, the concentration profiles can be smoothed to compensate for small variation on the concentration profiles, a typical method used is the Savitzky-Golay method. Since its development, the minimally invasive capillary sampling technique was applied to study several gas phase reactions such as methane catalytic partial oxidation on rhodium and platinum coated foam catalyst [134], [135], methane oxidative coupling in the gas phase [136] and oxidative dehydrogenation of ethane to ethylene on a supported molybdenum oxide catalyst [3]. So far, the minimal invasive spatial sampling technique has been restricted to gas phase heterogeneous catalytic reactions.

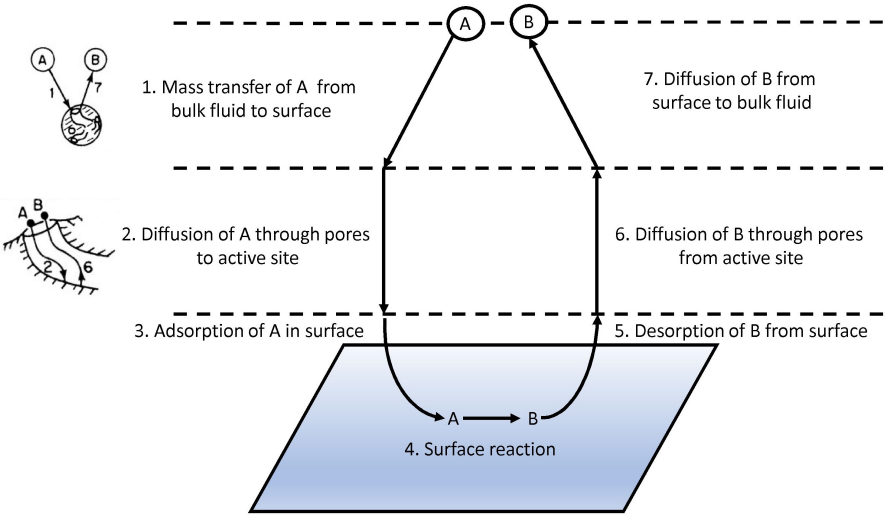

Figure 3.21: Steps in heterogeneous catalytic reaction

3.5 Measurements in experimental fixed bed reactors

Accurately performed measurements are crucial for kinetic studies on heterogeneous catalysis. There are several steps involved during a catalytic reaction on the surface of a solid shown in Figure 3.21. If any of these steps is slower than the surface reaction, the measured data can lead to inaccurate results. In consequence, to accurately measure kinetic data is important to verify that the system is free of heat and/or mass transport limitations. In order to reach the surface, the reactants in the bulk fluid phase must first diffuse through a stagnant boundary layer surrounding the catalyst particle [137]. When the mass transfer through this stagnant boundary layer becomes slower than the surface reaction, the measured rate will be masked by the film diffusion rate. Analogously, the same effect can be observed due to heat transfer limitations when the conduction of heat through the film is slower than the production/consumption of heat on the catalyst surface [138], [139]. External mass limitation can be analytically estimated by using the Mears criteria, which relates the measured reaction rate with the rate of trans-

port by diffusion in the bulk fluid:

$$\text{Mears criteria for external mass transfer limitations}$$
$$\frac{-R_{obs} r_p n}{k_c C_b} = \frac{\text{measured reaction rate}}{\text{rate at bulk fluid conditions}} \leq 0.15$$

Where $R_{obs}[mol\, m^{-3}\, s^{-1}]$ is the measured initial reaction rate, $r_p\,[m]$ is the radius of the catalyst particle, n is the reaction order, $k_c[m\, s^{-1}]$ is the mass transfer coefficient and $C_s[mol\, m^{-3}]$ is the concentration at the surface of the catalyst. Also external mass transfer limitations can be experimentally assessed as shown in Figure 3.22. In the presence of external mass transfer limitations the measured rate is dependent on the thickness of the stagnant boundary layer surrounding the catalyst particles. As the superficial velocity of the bulk fluid increases, the thickness of the boundary layer decreases until a point in which the rate of diffusion through the stagnant boundary layer becomes negligible compared to the rate of surface reaction. Under these conditions, the conversion for a given residence time becomes independent of the superficial velocity of the bulk fluid. Therefore, the test to evaluate external mass transfer limitations consist in measuring the conversion at a constant space time as a function of the volumetric flow. If the measured conversion is constant over a range of flow rates, it can be concluded that the effect of external mass transfer limitations are negligible [129].

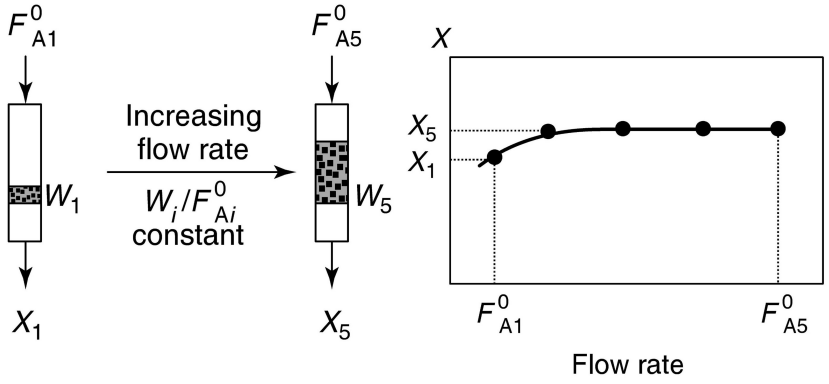

Figure 3.22: Experimental test for external mass transfer limitations

Analogously, external heat transport limitations can be evaluated by the Mears criteria for heat transport [140]:

Mears criteria for external heat transfer limitations

$$\frac{|\Delta H_r| R_{obs} r_p}{h T_b} \leq 0.15 \frac{T_b R}{E_a}$$

Where $\Delta H_r [J mol^{-1}]$ is the enthalpy of reaction, $h [W m^{-1} {}^\circ K^{-1}]$ is the heat transfer coefficient, $T_b [^\circ K]$ is the bulk temperature of the fluid, $R [J\, mol^{-1}\, {}^\circ K^{-1}]$ is the gas constant and $E_a [J\, mol^{-1}]$ is the activation energy of the reaction.
Usually, solid catalyst are porous materials that provide a high surface area per unit of mass. Most of the active sites in which the surface reaction occurs are located within the pore network of the material. Therefore, the diffusion of the reactant in the pore system of the catalyst has an influence on the measured rate. Internal heat and mass transport limitations can be assessed by evaluating the conversion achieved at constant space time and catalyst mass as a function of the catalyst particle size as shown in Figure 3.23. If the conversion decreases as the particle size increases it can be concluded that internal mass transport limitations are present.

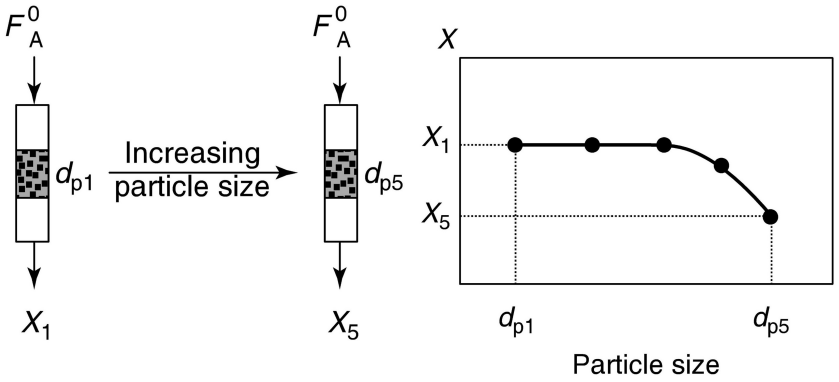

Figure 3.23: Experiment test for internal mass transfer limitations

For analytical determination of internal mass transport limitations the Weisz-Prater criteria can be calculated [141]. This dimensionless number compares the measured rate of reaction with the rate of pore diffusion. The rate of pore diffusion depends on the concentration of reactants at the surface of the catalyst which is

difficult to measure experimentally. Therefore, this criteria is usually calculated once external mass transfer limitations are excluded, since under these conditions the bulk and surface concentrations can be considered equal.

Weisz-Prater criteria for internal mass transfer limitations

$$\frac{R_{obs} r_p^2}{C_s D_{eff}} \leq 0.3$$

Where $D_{eff}[m^2\, s^{-1}]$ is the effective diffusion coefficient inside the pore structure of the catalyst particle. The effective diffusion coefficient can be calculated knowing the porosity and tortuosity of the catalyst particle. The porosity of many solid catalyst falls in the range of 0.3-0.7 and the tortuosity between 2-7, when information about the catalyst is not available a porosity of 0.5 and a tortuosity of 3 are often used as estimations [142]. Analogously, the predominance of intra-particle temperature gradients can be evaluated by the Anderson criteria [140]:

Anderson criteria for internal mass transfer limitations

$$\frac{|\Delta H_r| R_{obs} r_p^2}{\lambda T_s} \leq 0.75 \frac{T_s R}{E_a}$$

Where $T_s\,[^\circ K]$ is the temperature at the surface of the catalyst. Under the conditions in which external heat transport limitations can be considered negligible the surface temperature of the catalyst can be considered approximately equal to the bulk temperature of the fluid surrounding the catalyst particle.

4 Materials and Methods

4.1 List of chemicals used

Chemical	Supplier	Purity	CAS Nr.	Art. Nr.
Hydrogen Peroxide	Evonik AG	20-60 % wt	772-84-1	—
Methanol	Merk	Technical grade	67-56-1	8222839025
Propylene	Westfalen	Propen 3.7	115-071	G332126
Methyl Tert Butyl Ether	Merck	Emsure for analysis	1634-04-4	1018491000
1-Methoxy-2-Propanol	Alfa Aesar	>99 %	107-98-2	29094980
2-Methoxy-1-Propanol	TH Geyer	95 %	1589-47-5	11969317
Propylene Glycol	Sigma Aldrich	>99 %	57-65-6	134366-1L
Hydroxyacetone	Sigma Aldrich	90 %	116-09-6	138185-500G
Propylene Oxide	Merck	>99 %	75-56-9	8070271000
TS-1 catalyst	ACS Materials	Type A	12173-28-3	—
Lavasil CA413 PNM	AkzoNobel	39,98 % SiO_2	—	8019216

Table 4.1: List of Chemicals used

4.2 TS-1/SiO_2 catalyst preparation and characterization

TS-1 powder was bought from ACS Materials (390 $[m^2\ g^{-1}]$, Si/Ti≥25, type=A, particle size=0.3-0.5 μm).The extrusion process employed on this work is based on the generation of a homogeneous paste comprised by the catalyst powder, an inorganic support and organic binder [143]. The inorganic catalyst support provides the suitable physical strength, while the organic binder provides the required

plasticity for the extrusion process. As inorganic support precipitated silica Siper-nat 310 (700 $[m^2\ g^{-1}]$, particle size=8.5 μm, pH=6) was used, others commonly used inorganic supports such as alumina oxide are known to increase the acidity of the catalyst, and thereby the rate of ring opening reactions [144]. As organic binder methyl-cellulose ($3500-5600\times10^{-3}[Pa\,s]$ 2% water at 20°C) was used. The homogeneous paste was prepared in a ratio of 55/35/10 wt% (catalyst/inorganic binder/organic binder) and mixed with enough water to achieve the desired plas-ticity. Then, the paste was extruded and cut to 3 mm diameter and 3-5 mm length pieces. The extrudate pieces were calcinated at 500 °C with a low temperature ramp to avoid breakage while removing water and organic content. The calcina-tion temperature is such that no phase transition or alteration of the catalytic activity occurs [145]. A total 134 grams of catalyst extrudates were prepared. A fraction of the prepared extrudates were crushed to splits and sieved to be able to pack the catalyst in the compact profile reactor CPR. To determine the upper and lower limit of the sieving process the Bodenstein criteria was used. In this sense, if $Bo > 80$ the deviations from ideal plug flow are small and the reactor can be regarded as a cascade of N CSTRs.

$$N = \frac{Bo}{2} = \frac{Pe_{m,ax}}{2}\frac{l}{d_p} \qquad \text{(liquids, } \mathrm{Re_p}<100\text{)}$$

The maximal length of catalyst bed is L = 60 mm resulting in a particle size of $d_p < 375$ μm. Therefore, the particles were sieved between 300 μm and 400 μm. Both catalyst pellets and catalyst split used in the pilot scale (HP-PO) reactor and CPR are shown in Figure 4.1.

Standard powder X-ray diffraction (XRD) measurements for qualitative phase composition analysis were conducted using an Empyrean diffractometer from Malvern Panalytical. XRD patterns were recorded over a 2θ range from 10° to 35°using the Kα-lines of copper and a PIXcel1D detector HighScore Plus software and reference patterns from the ICDD database were used for qualitative phase analysis. To de-termine the surface area by physisorption of nitrogen at 77 K a Quantachrome autosorb IQ 2 (Anton Paar GmbH, Graz, Austria) was used. To asses the mor-phology of the catalyst powder, extrudates and splits were analyze by a Zeiss Supra 55 VP FEG-SEM with Variable Pressure Mode (VP-Mode). The FTIR

Figure 4.1: TS-1/SiO_2 pellets and TS-1/SiO_2 splits

spectrum of the catalyst was recorded between 400 and 4400 cm^{-1} in transmission mode (KBr disk method) on a Vertex70 spectrometer equipped with a KBr beam-splitter and a DTGS detector (Bruker, Billerica, USA) by adding 128 scans at a nominal resolution of 2 cm^{-1}.

4.3 Periodic Open Cells Coating Procedure

The catalyst coating procedure was based on dip-coating the POCs in a mixture of commercial TS-1 catalyst powder suspended in a solution of colloidal silica to form a uniform catalyst layer on the surface of the structures. Removal of the fluid phase, by for example drying, allows the silanol groups on the surface of the silica particles to react with each other by condensation as shown in Figure 4.3. This condensation reaction, causes the solution to form a continuous matrix of covalently bonded particles entrapping the suspended TS-1 catalyst particles within. Further drying forms a xerogel consisting of a porous amorphous silica structure. The device used to dip-coat the structures with reproducible speeds is shown in Figure 4.2 a) and b). The POCs shown in Figure 4.2 c) consisted in a 100 $[mm]$ length cubic periodic structure, with a overall diameter of 17 $[mm]$, a cell length l_c of 5 $[mm]$, a strut diameter of 0.6 $[mm]$ and a central channel of 1.7 $[mm]$ to accommodate the sampling capillary . The commercial Lavasil CA413 PNM colloidal silica solution used to suspend the catalyst powder was provided by AkzoNobel ($\rho = 1.286[g\,cm^{-3}]$, $SiO_2 = 39.98$ %wt, $NH_3 = 0.163$ %wt, $pH = 9.1$, $\mu = 9.8[mPa\,s]$). The coating mixture consisted in 75% colloidal silica solution

and 25% suspended catalyst powder.

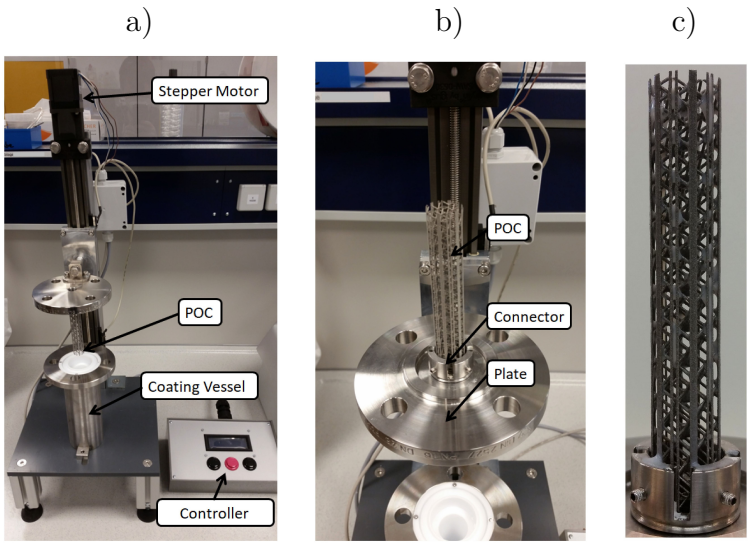

Figure 4.2: a) and b) POCs dip-coating device, c) Periodic open cell structure POCs. Taken from [146]

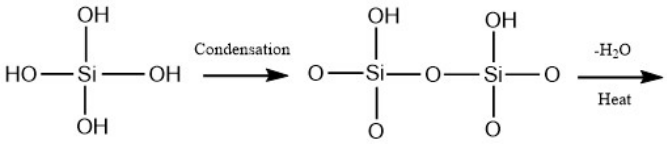

Figure 4.3: Condensation reaction of silanol groups on the surface of silica particles

Upon dipping, the extraction speed can affect the thickness of the coating [147]. In this case, the dipping velocity was set to 3 $[mm\ s^{-1}]$, while the extraction velocity was 1 $[mm\, s^{-1}]$. After each dip-coating cycle, the structures were dried at 50°C followed by a final calcination step at 350°C for 2 hours to remove the water and NH_3 content. Under the assumption that the coating mixture was perfectly mixed and homogeneous, the final dried solid composition is calculated to be 45% wt catalyst to 55 % wt dried colloidal silica.

4.4 Analytical Methods

To analyze the organic products of reaction an in-line modified Gas Chromatograph Agilent 7890B equipped with two flame ionization detector (FID), two micropacked columns 10% RTX-Stabilwax DIATO-WNAW 80/100 (Restek, 2 m x1.0 mm ID x 1/16" OD), a RT-Q-Bond column (Restek, 30 m x 0.32 mm ID and 1μm film) and a Stabilwax Column (Restek, 30 m x 0.32 mm ID and 1 μm film) were used. This analytical device is able analyze samples at reaction conditions, that is 20-30 bar pressure, with Pr entirely in liquid phase. In Figure 4.6 a diagram of the Gas Chromatograph with ON/OFF positions of the switching valves is shown. The calibration of the Gas Chromatograph was done using the internal standard method. This method is based on a reference compound called Internal standard (IS), in this case Methyl tert butyl ether (MTBE). The response of the component (i) is proportional to the response of the reference standard.

$$\frac{Ai}{[i]} = Ri\frac{A_{IS}}{[IS]} \quad ; \quad [i] = \frac{1}{Ri}Ai\frac{[IS]}{A_{IS}} \quad ; \quad \frac{[i]}{[IS]} = \frac{1}{Ri}\frac{Ai}{A_{IS}}$$

Where (A_i) is the area of measured peak of component i, ($[i]$) the concentration of component i in $[mol\, l^{-1}]$, (R_i) the response factor of component i, (A_{IS}) the area of measured peak of the internal standard and ($[IS]$) the concentration of internal standard in $[mol\, l^{-1}]$. For the identification of the side products of reaction by GC/MS Screeining an Agilent Gas Chromatograph 6890N coupled with a Mass Spectrometer MSD 5975 was used. The concentration of HP was measured using potentiometric titration with Cerium (IV) Sulfate in an Titration Unit TitroLine 7000 from SI Analytics. Cerium (IV) Sulfate solutions are remarkably stable over prolonged periods of time without appreciable change in concentration [148] and are suitable for samples that contain organic compounds [149].

$$Ce(SO_4) + H_2O \rightleftharpoons Ce_2(SO_4) + H_2SO_4 + O_2$$
$$H_2O_2 \rightleftharpoons O_2 + 2H^+ + 2e^- \qquad E^0_{ox} = -682mV$$
$$2Ce4+(SO_4)_2 + +2H^+ + 2e^- \rightleftharpoons Ce_2(SO_4)_3 + H_2SO_4 \qquad E^0_{red} = +1440mV$$

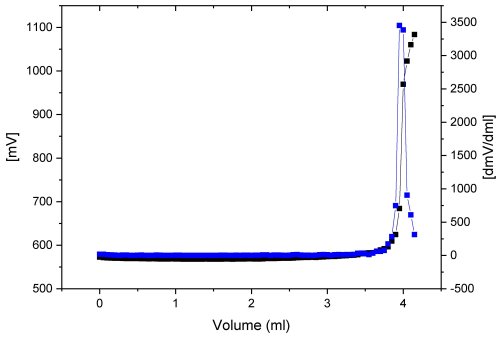

Figure 4.4: Typical sigmoidal titration curve and its first derivative as a function of titrant volume

In this reaction the Cerium (IV) Sulfate oxidizes the HP to form Cerium (III) Sulfate, sulphuric acid and oxygen. The amount of titrant that reacted with the amount of HP present in the sample can be determined by the end point of the titration. The end point can be determined by the inflexion point on the titration curve or by calculating the change in potential per unit volume of titrant $\Delta E/\Delta V$ (first derivative). A plot of the first derivative yields a curve with a maximum which corresponds to the inflection point and the end point of the titration as shown in Figure 4.4. Optionally, the second derivative can be calculated for more accuracy. Then, from the stoichiometry of the Equation 4.1 the concentration of HP in the sample taken at the position (z) can be calculated as follows:

$$[H_2O_2]_z = \frac{(X_{\text{end}} - X_{\text{blank}}) \cdot [Ce\,(IV)]}{2 \cdot W_{\text{sample}} \cdot \frac{1}{\rho_{\text{sample}}}}$$

Where $[H_2O_2]_z$ is the concentration of HP in the sample taken at the position (z) in $[mol\ l^{-1}]$, X_{end} the consumed volume of standard titrant solution by analyte sample in $[ml]$, X_{blank} the consumed volume of standard titrant solution by blank sample in $[ml]$, $[Ce(IV)]$ the concentration of standard titrant in $[mol\,l^{-1}]$, W_{sample} the mass of sample in $[g]$ and ρ_{sample} the density of the sample in $[g\,ml^{-1}]$.

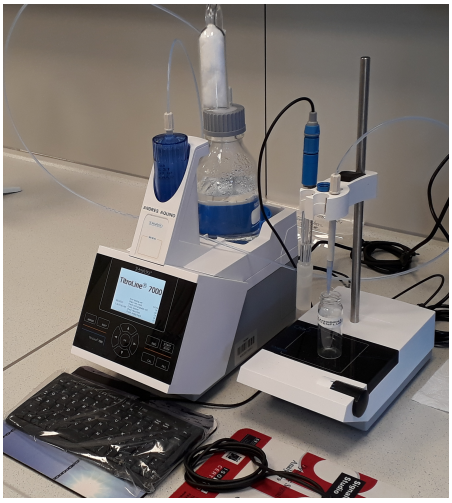

Figure 4.5: Potentiometric Titration Unit TitroLine 7000 SI Analytics

4.5 Modeling of fixed bed reactors

Due to the complex physical and chemical phenomena taking place in packed bed reactors, their exact description is either impossible or leads to very complex mathematical models. To reduce the computational demand required in the simulation of chemical reactors, is often desired to simplify the model in order to eliminate any unnecessary mechanisms and equations that are not essential to the overall performance of the process. The proper model should be simple but still contain sufficient representation of the essential mechanisms involved. In consequence, the type of model has to be selected taking in consideration the features and properties of the system under analysis. The different mathematical models used to simulate fixed be reactor are summarized in Figure 4.7.

One dimensional pseudo homogeneous models are often used when intra/external particle heat and mass transfer limitations can be consider negligible and only gradients on the axial direction are expected. In contrast, heterogeneous models are used when significant temperature and concentration gradients are expected between the phases. When a deviations from ideal flow are expected due to molecular diffusion, eddy diffusion or nonuniform distribution of the flow axial dispersion models are often implemented to describe the system. Two dimensional models are used when significant concentration and temperature gradients

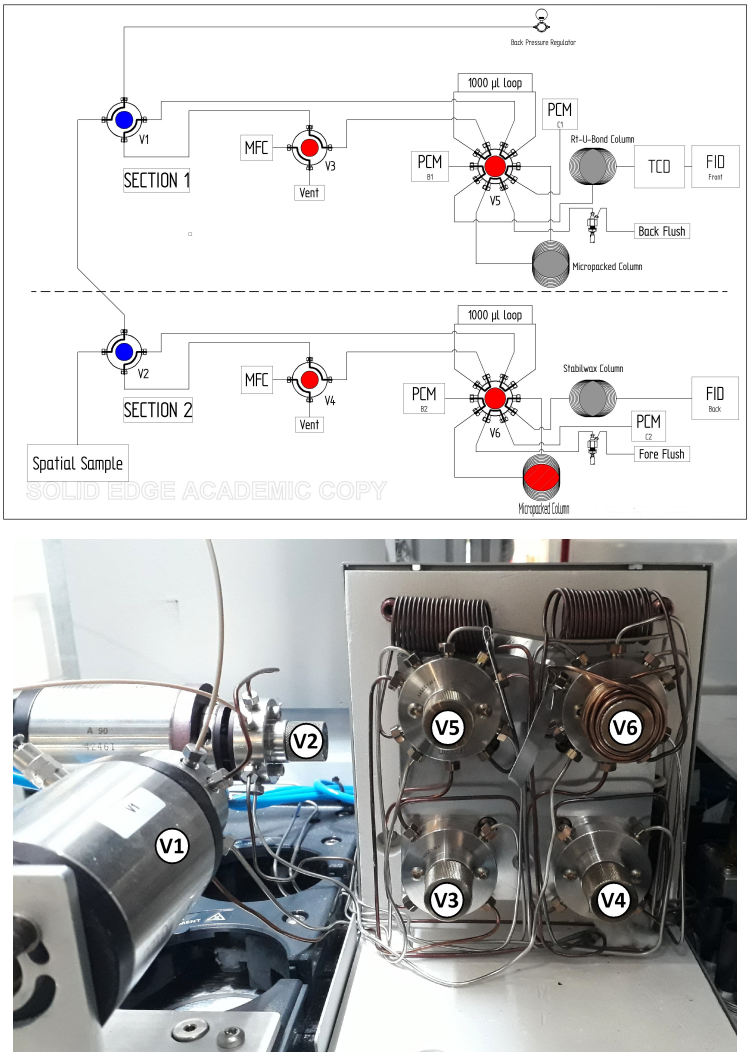

Figure 4.6: (Up) GC Diagram OFF Positions. Outside GC (Blue), red (Valve box), grey (Oven). (Down) GC injection valves arrangement

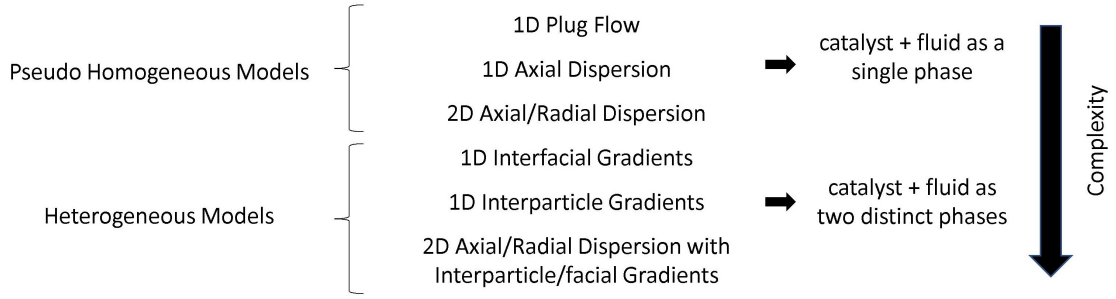

Figure 4.7: Classification of classical continuum models

are expected on the radial direction. Alternatively, computational fluid dynamics (CFD) simulation may be used to model in detail the flow fields within the fixed bed reactor for low tube-to-particle diameter ratio where channeling effects are expected [150]. Typically, measurements in experimental fixed bed reactors are conducted in the absence of internal and external transport limitations to ensure that the rate being measured is the surface reaction on the catalyst. Additionally, lab-scale reactors have typically small internal diameters which reduces the possibility of temperature and concentration gradients in the radial direction. In this case, 1-dimensional pseudo homogeneous models are sufficient and can be used instead of 2-dimensional heterogeneous models, if both the interfacial concentration gradients and the interfacial temperature gradients are small. Due to the very low specific flow rates used in this work required to achieve high conversion, deviations from the ideal plug flow behavior are expected. To determine if axial dispersion should be included in the model the Bodenstein criterion can be used:

$$N = \frac{Bo}{2} = \frac{Pe_{m,ax}}{2}\frac{l}{d_p} \qquad \text{(liquids, } \mathrm{Re_p}<100\text{)}$$

If $Bo > 80$, the deviations from ideal plug flow are small and the reactor can be regarded as a cascade of N CSTRs. In contrast, if $Bo < 80$ deviations from plug flow are expected and the 1D-pseudo-homogeneous model should include axial dispersion. The governing equations of an axial 1D-pseudo-homogeneous

dispersion model are shown in the following set of equations:

Mass Balance

$$u_s \frac{dC_i}{dz} - \epsilon D_{ax} \frac{d^2 C_i}{dz^2} + \sum_{j=1}^{j=m} a_{ij} \rho_b r_j = 0$$

Energy Balance

$$C_p \rho_l u_s \frac{\partial T}{\partial z} - \lambda_{ax} \frac{\partial^2 T}{\partial z^2} + \sum_{j=1}^{j=m} a_{ij} r_j \Delta H_{rj} = \frac{4 U_{ext}}{d_R} (T_{wall} - T)$$

Momentum Balance

$$\frac{P_0 - P_L}{L} = 150 \frac{\mu u_s}{d_p^2} \frac{(1-\epsilon)^2}{\epsilon^3} + \frac{7}{4} \frac{\rho_l u_s^2}{d_p} \frac{(1-\epsilon)}{\epsilon^3}$$

The particle dispersion coefficient for mass transfer (D_{ax}) can be determined graphically as a function of the Reynolds particle number based on the work of Wilhelm et. al shown in Figure 4.8. Alternatively, a wide range of correlations for the effective radial diffusivity [151], [152], [153], [154] and for the axial mass dispersion coefficient [155], [156], [157] in packed beds are available in the literature. Then, the reactor scale dispersion coefficient can be obtained by multiplying the obtained (D_{ax}) with the (L/d_p) ratio of the catalyst bed.

The dispersion coefficient for heat transport (Λ_{ax}) can be calculated following the work of Winterberg and Tsotsas et.al. [159].

$$\frac{\Lambda_{ax}}{\lambda_f} = \frac{\lambda_{bed}}{\lambda_f} + \frac{Pe_{ax,h}}{K_{ax}} \qquad K_{ax} = 2$$

$$Pe_{ax,h} = \frac{u_0 \rho_f C p_f d_p}{\lambda_f}$$

Where (λ_f) is the heat conductivity of the fluid and (λ_{bed}) is the heat conductivity of the packed bed without fluid flow both in $[W\ m^{-1}\ K^{-1}]$. For high reactor tube-to-particle diameter ratios it has been shown that the bed porosity (ϵ) oscillates between 0.36 and 0.42 and for practical purposes can be approximated to

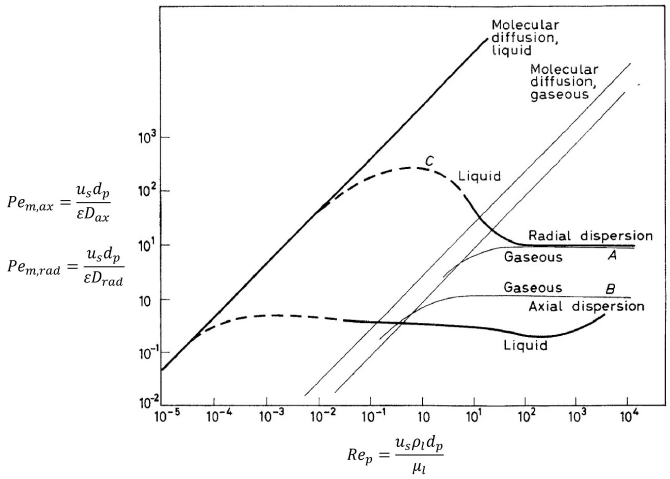

Figure 4.8: Axial and Radial Peclet numbers as a function of the particle Reynolds number for packed beds, take from [158]

a constant value of 0.4 [160], [161]. The thermal conductivity of the packed bed without flow (λ_{bed}), can be calculated by the following set of equation based on the the model of Zehner/Bauer/Schloender take from [162]. Because the reaction studied in this work is a low temperature liquid phase reaction, the contribution of the secondary parameters of the model can be neglected.

$$k_{bed} = 1 - \sqrt{1-\epsilon} + \sqrt{1-\epsilon} k_c \qquad k_{bed} = \frac{\lambda_{bed}}{\lambda_f} \tag{4.1}$$

$$k_c = \frac{2}{N}\left(\frac{B}{N^2}\frac{k_p - 1}{k_p}\ln\frac{k_p}{B} - \frac{B+1}{2} - \frac{B-1}{N}\right)$$

$$N = 1 - \frac{B}{k_p} \qquad B = 1.25\left(\frac{1-\epsilon}{\epsilon}\right)^{\frac{10}{9}} \qquad k_p = \frac{\lambda_p}{\lambda_f}$$

Where (λ_p) is the heat conductivity of the catalyst particles in $[W\,m^{-1}\,K^{-1}]$. The fluid-particle heat transfer can be calculated by the work of Gnielinski [163]. The coefficient can be estimated by implementing a form factor f_a and a Nusselt number

equation that applies for a flow over a single catalyst particle.

$$Nu = f_a Nu_p$$
$$Nu_p = 2 + \sqrt{Nu_{lam}^2 + Nu_{turb}^2}$$
$$Nu_{lam} = 0.664\sqrt{Re_\epsilon}\sqrt[3]{Pr}$$
$$Nu_{turb} = \frac{0.037 Re_\epsilon^{0.8} Pr}{1 + 2.443 Re_\epsilon^{-0.1}(Pr^{\frac{2}{3}} - 1)}$$
$$Nu = \frac{\alpha_f d_s}{\lambda_f}$$
$$Re_\epsilon = \frac{U_0 d_s}{\mu_f}$$
$$Pr = \frac{\mu_f C_p}{k}$$
$$d_s = \sqrt{\frac{A_p}{\pi}}$$

Where (α_f) is the fluid-particle heat transfer coefficient in $[W\ m^{-2}\ K^{-1}]$, (d_s) is the diameter of a sphere of the same area as that of a catalyst particle in $[m]$, (λ_f) is the conductivity of the fluid in $[W\ m^{-1}\ K^{-1}]$, U_0 is the superficial velocity in $[m\ s^{-1}]$, (μ_f) is the fluid viscosity in $[kg\ m^{-1}\, s^{-1}]$ and (C_p) is the liquid heat capacity in $[J\ kg^{-1}\ K^{-1}]$. In this case, the catalyst splits are assumed to approximate a cylindrical shape, therefore the form factor is $f_a = 1,6$. The physical properties of the fluid are evaluated at the inlet temperature. In the reaction studied in this work the term related to turbulent flow can be neglected, since the reactor is operated under laminar regime. The diffusion coefficients for the chemicals species through the bulk solvent MeOH can be estimated by the Wilke-Chang equation for diffusion in liquids [164]. In the case of diffusion in liquids, molecules are tightly packed together when compare to gases, and they are more likely to collide with each other than with the pore walls. In consequence, Knudsen diffusion is not considered relevant in liquid phase reactions [165]. The system of partial differential equations was solved in the software COMSOL Multiphysics 5.5 by the finite element method [166]. Due to the low specific flow rate required to achieve high conversion and the fact that pre and post reactions zones were packed with an inert material (quartz wool), it is assumed that axial dispersion occurs not only

in the reaction zone but also in the pre and post reaction zones of the simulation domain. Then, the Dirichlet boundary conditions were used to solve the system of differential equation.

$z = 0, \forall r$	$C_i = C_{i,0}$	$T = T_0$
$z = L, \forall r$	$\frac{\partial C_i}{\partial z} = 0$	$\frac{\partial T}{\partial z} = 0$

Table 4.2: Boundary conditions of axial 1D pseudo-homogenous dispersion model

4.6 Profile data fitting

Several previous publications have shown that the minimal invasive spatial sampling technique can provide a significant amount of kinetic data which can be used to validate kinetic models. This technique has been used in combination with numerical simulations to study methane partial oxidation on rhodium [134] and on platinum [135], dry reforming of methane combined with particle resolved CFD simulation [167], methane combustion on a platinum gauze [168], CO oxidation on Pt nanoparticles supported on an $\alpha - Al_2O_3$ foam monolith combined with microtomography-based CFD [169] and n-butane oxidation to maleic anhydride on vanadyl pyrophosphate catalyst pellets [170]. For validation of kinetic models the usual approach is to fit the model to the experimental data followed by a qualitative and quantitative analysis of the model correlation with the experimental data. The fitting of the model can be done by either linear or non-linear regression depending on the complexity of the derived rate law. Linear regression has the particular advantage that no initial values are required for the regression. However, non-linear regression is available in several simulation softwares and is increasingly being used as standard method. Taking as example a Langmuir-Hinshelwood model for a irreversible surface reaction:

$$A + B \xrightarrow{\text{catalyst}} AB$$

The derived rate law is:

$$r_a = \frac{k_r K_a K_b [A][B]}{(1 + K_a [A] + K_b [B])}$$

The model parameters are $k_r = k_{r,0} e^{\frac{-E_r}{RT}}$, $K_a = K_{a,0} e^{\frac{\Delta H_a}{RT}}$ and $K_b = K_{b,0} e^{\frac{\Delta H_b}{RT}}$. Then, the sum of squares of differences between the proposed kinetic model and experimentally observed values can be defined as:

$$f(p) = min_p || r_{a,calc}(p, [A]_{k,calc}, [B]_{k,calc}) - r_{a,data}([A]_{data}, [B]_{data}) || = \\ min_p \sum_{k=1}^{k} [r_{a,calc}(p, [A]_{k,calc}, [B]_{k,calc}) - r_{a,data}([A]_{data}, [B]_{data})]^2 \quad (4.2)$$

Where the parameters vector $p = (k_{r,0}, K_{a,0}, K_{b,0}, E_r, \Delta H_a, \Delta H_b)$ contains the control variables. The objective of a non-linear regression, is to find a set of control variables for the vector (p) which minimize the difference in Equation 4.2 for the k number of experimental data points. There are several numerical method to solve non-linear least square problems, such as the Nelder-Mead Simplex algorithm, conjugate gradients algorithm, newton methods, etc [171], [172]. The optimization module of the software COMSOL Multiphysics uses the Levenberg-Marquardt algorithm in Equation 4.3 to solve this type of iterative numerical problems. This algorithm combines the Gradient Decent in Equation 4.5 and Newton method in Equation 4.4 in a single equation.

$$p_{n+1} = p_n - \left[\nabla^2 g(p) + \lambda I\right]^{-1} \nabla g(p) \quad (4.3)$$

$$\text{when} \quad \lambda \to 0 \quad ; \quad \left[\nabla^2 f(p_n) + \lambda I\right]^{-1} \to \left(\nabla^2 f(p)\right)^{-1}$$
$$f_{p+1} = p_n - \left(\nabla^2 f(p_n)\right)^{-1} \nabla f(p_n) \quad (4.4)$$

$$\text{when} \quad \lambda \to \infty \quad ; \quad \left[\nabla^2 f(p_n) + \lambda I\right]^{-1} \to (\lambda I)^{-1} = \frac{1}{\lambda} I = \mu I$$
$$p_{n+1} = p_n - \mu \nabla f(p_n) \quad (4.5)$$

The method convergence depends on the initial values of the control variables contained in the vector (p). For the validation of a existing kinetic model from the scientific literature the kinetic parameters of the model can be used as initial guess for the vector (p) to solve least squares minimization problem. In the case of validation of a proposed kinetic model the initial values for the vector (p), namely the activation energies, frequency factors and adsorption constants have to be first determined experimentally or can be taken from the available literature. Typically, the reactions activation energies and frequency factors can be obtained by measuring the initial reactions rate at different temperatures of reaction and constructing an Arrhenius plot. The adsorption constants can be estimated by thermodynamic calculation. This approach is used for relatively simple system of reacting gases at lower pressure. For complex mixtures far from ideal conditions thermodynamic calculations becomes increasingly difficult. In this case, the adsorption constant can be experimentally determined by systematically varying the initial concentration of reactants/products and plotting the dependence of the initial reaction rate on said concentration [173], [137], [174].
To preform a quantitative statistical analysis, the variance and the $F_C - test$ are typically used to discriminate between different proposed models:

$$\sum_{i=1}^{n} S_i^2 = \frac{\sum_{i=1}^{n} \left(C_{i,exp} - C_{i,model}\right)^2}{n-p}$$

$$F_{C_i} = \frac{\frac{\sum_{i=1}^{n}(C_{i,exp}-C_{i,model})^2 - \sum_{i=1}^{n_e}(C_{i,exp}-\bar{C}_{i,exp})^2}{n-p-n_e+1}}{\frac{\sum_{i=1}^{n_e}(C_{i,exp}-\bar{C}_{i,exp})^2}{n_e-1}}$$

$$\sum_{i=1}^{n} F_{C_i} \leqslant \sum_{i=1}^{n} F(n-p-n_e+1, n_e-1, 1-\alpha)$$

Where $(C_{i,exp})$ is the experimental concentration, $(C_{i,model})$ is the concentration of the chemical species i calculated by the model, $(\bar{C}_{i,exp})$ is the mean of the experimental concentration in $[mol\,l^{-1}]$, (n) is the number of experimental data points in the concentration profile, (p) is the number of parameters of the model, (n_e) is the number of repetitions per experimental data point and (α) is the significance level of the F-test. Since several species profiles are simulated simultaneously in this

work, the overall summatory of the variance ($\sum_{i=1}^{n} S_i^2$) and $F_C - Value$ ($\sum_{i=1}^{n} F_{C_i}$) for each experimental profile against its respective simulated value are used as statistical criteria.

5 Results and Discussion

In this chapter, the first application of the minimal invasive capillary spatial sampling technique to study a liquid phase reaction is presented. The results on Section 5.6, Section 5.7, Section 5.9 and Section 5.10 have been previously published in the Industrial & Engineering Chemistry Research Journal [175] and are extended with complementary results and measurements. The construction of the CPR experimental setup in Section 5.1.2 and the determination of products of reaction and mass balance of the reaction system in Section 5.4 were part from a previous work [176]. The experiments performed in the pilot scale spatial profile reactor in Section 5.11 have been conducted by Philip Wosiek and have been published in his master thesis [146].

5.1 Liquid phase spatial profile reactors

For the measurement of spatially resolved profiles of the Pr selective oxidation to PO with HP over TS-1 catalyst two liquid phase spatial profile reactor were designed, built, and brought into operation as part of this work. A pilot scale spatial profile reactor with a internal diameter comparable to a single tube in a technical scale (HP-PO) reactor was implemented to study the reaction with catalyst extrudates with dimension similar to those used in industrial applications. Additionally, the reactor was packed with additively manufactured catalyst-coated open cell structures as substitute approach for the conventional randomly packed bed reactor. A compact profile reactor (CPR) provided by Reacnostics GmbH was integrated in parallel to the pilot scale profile reactor. The compact reactor allows to perform kinetics studies of the reaction with low consumption of chemicals and safe operation due to the small reacting volume. A simplified flow diagram of the

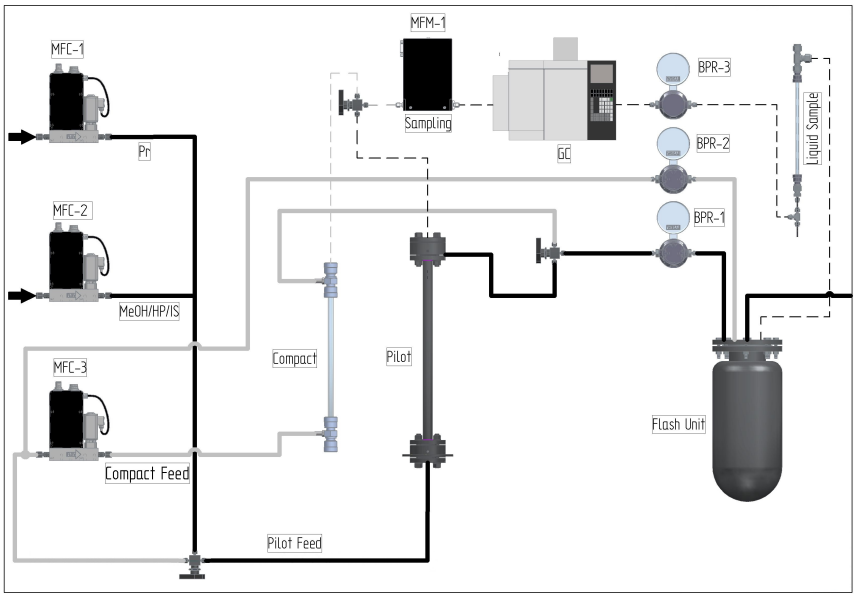

Figure 5.1: Simplified flow diagram of experimental setup

experimental setup is shown in Figure 5.1. In the following section the details of both state of the art experimental spatial profile reactors will be highlighted.

5.1.1 Pilot scale spatial profile reactor

The pilot scale profile reactor shown in Figure 5.2 (left) is a 18 mm ID, 22 OD mm and 1000 mm length jacket tube in which 3 mm diameter and 5 mm length catalyst extrudates are packed. The reaction temperature is controlled by cooling water circulating through the jacket of the reactor using a recirculation chiller set to the reaction temperature of 40 °C. Alternatively, the cooling jacket feed can be automatically changed by a set of magnetic valves to a secondary source of cooling water 25 °C colder. The secondary cooling system is used to quench the rate of reaction avoiding any potential thermal runaway. The pressure of the reactor is controlled by a back pressure regulator BPR-1 which sets the reaction pressure to e.g: 25-30 bar. Additionally, to avoid any increase of pressure beyond the tolerance of the equipments, relief valves and rupture discs were assembled in both bottom and top flanges of the reactor.
Through the central axis of the reactor runs a sampling PEEK tubing (1.6 mm

OD (1/16"), 0.8 mm ID) with a side sampling orifice of 200 μm. A 0.5 mm thermocouple type K, tip aligned with the orifice sits inside the sampling tubing. The sampling tubing is assembled on a high precision step motor which changes the position of the sampling orifice/thermocouple relative to the catalyst bed. The sampling line is sealed by a sealing system specially designed for this purpose shown in Figure 5.2 (middle). The developed sealing concept is based on a front plug and a back ferrule made of two materials with different hardness, in this application silicon rubber and teflon (PTFE). When the nut of the fitting is tighten the back ferrule is pushed against the softer front plug deforming it in the horizontal direction. The deformation of the front plug seals the sampling capillary with enough tightness to hold the reaction pressure (e.g: 30 bar) but still allowing the movement of the sampling system in the axial direction. The reactor is mounted in a ventilated rack to avoid any accumulation of flammable/explosive chemicals such as Pr. The main characteristics of the pilot scale liquid phase spatial reactor are summarized in Table 5.1 while the actual experimental setup in the experimental hall of the Hamburg University of Technology is shown in Figure 5.2 (right).

Table 5.1: Main Characteristics of pilot scale (HP-PO) reactor

HPPO reactor	Value	
Dimensions	18x22x1000 [mm] (IDxODxL)	
Max. Pressure	57.2 [bar]	
Temp. range	-10 to 80 [°C]	
Material	Stainless Steel: 1.4404	
Range of Residence Time (LHSV)	0.5-3.5 $[h^{-1}]$	
Manufacturer	Halmosi GmbH	
Additional features	Value	Supplier (Art.Nr.)
Relief valves	24.51.5 [bar]	Ham-let group (H900HPSSL1/4B)
Rupture discs	40-45 [bar]	Wehberg safety (11-1726-00)
Recirculating chiller	Cooling cap. 250 [W] at 20 °C	Fisher Scientific (Accel 250 LC 123 26 323)
Aux. cooling	18 [°C]	-
Step motor	Sub millimeter spatial resolution, 1000 $[mm]$	Festo (EGC-80-1000-BS-10P-KF-0H-ML-GV)

Note: residence time range is calculated based on the max/min ranges of MFC-2, a 500 [mm] bed and with ρ_{feed}= .875 $\frac{g}{ml}$

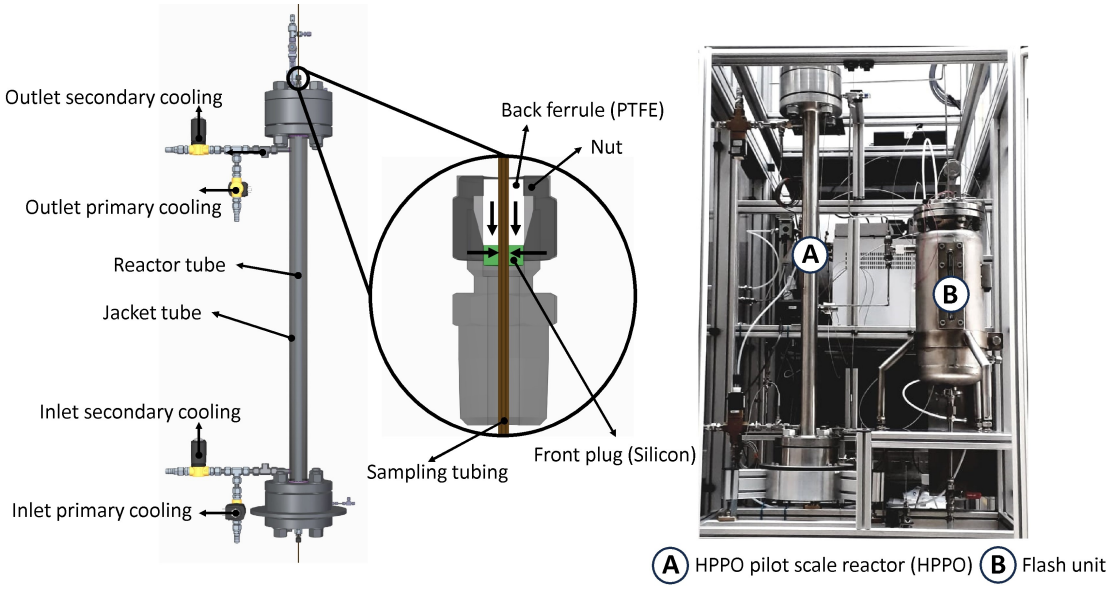

Figure 5.2: (left) Scheme of the pilot scale liquid phase profile reactor (middle) Sectional cut of the spatial sealing concept (right) Pilot scale profile reactor

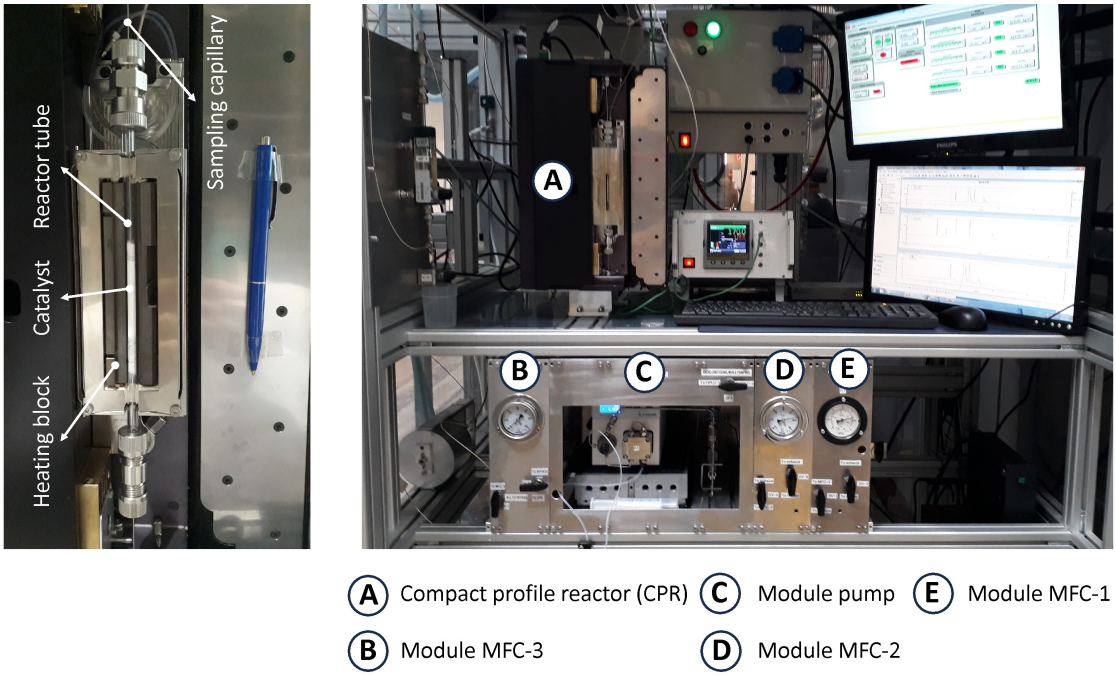

Figure 5.3: (left) Compact profile reactor (right) Feed modules

5.1.2 Compact profile reactor (CPR)

The CPR provided by Reacnostics GmbH was assembled next to the (HP-PO) pilot scale profile reactor. The compact reactor shown in Figure 5.3 is a 180 mm long quartz tube with 6 mm OD and 4 mm ID in which the catalyst splits are packed. The tube sits in a heating block with two heating cartridges that regulate the temperature of reaction. Through the central axis of the tube, runs a sampling capillary (0.75 mm OD, 0.5 mm ID) with a side-sampling orifice of 75 μm. A 0.25 mm thermocouple, tip-aligned with the orifice sits inside the sampling capillary. Both the sampling capillary and the thermocouple are fixed in space while a high precision step motor translates the reactor tube-heating block assembly in the axial direction (z). This axial movement changes the sampling position by moving the catalyst bed relative to the fixed spatial coordinate of the sampling orifice. The pressure of the reactor is controlled by a back pressure regulator BPR-1 usually set to the reaction pressure 20-30 bar. The main characteristics of the compact profile reactor are summarized in Table 5.2.

Table 5.2: Main Characteristics of CPR reactor

CPR reactor	Value
Dimensions	4x6x180 [mm] (IDxODxL)
Max. Pressure	25 [bar]
Temp. range	25 to 500 [°C]
Max. catalyst bed	60 [mm]
Range of Residence Time (LHSV)	0.29-29 $[h^{-1}]$
Manufacturer	Reacnostics GmbH

Note: residence time range is calculated based on the max/min ranges of MFC-3, a 40 [mm] bed and with ρ_{feed}= .875 $\frac{g}{ml}$

5.1.3 Dosing system and sampling

The chemicals dosing system is constituted by 3 feed modules, MFC-1, MFC-2 and MFC-3 and a pump module shown in Figure 5.4 a), b), c) and d) respectively. Pr in a dual valve gas cylinder is pressurized to reaction pressure by means of an inert gas piston injected in the head space of the gas bottle. The liquid port of the dual valve is connected directly to the module MFC-1 shown in the Figure 5.4 a). A Equilibar back pressure regulator able to handle both gas and liquids is used as pilot valve for the mass flow controller due to the presence of small traces of dissolved inert gas in the liquid media.

A mixture of MeOH/HP/IS with the desired concentration was pressurized to reaction pressure by a HPLC Knauer pump Azura P4.1S located in the pump module shown in Figure 5.4 d). The overflow of the pump is released by a relief valve set to desire pressure. The high pressure side of the relief valve is connected to the module MFC-2 shown in Figure 5.4 b) which doses a fraction of the overall pump output flow to the process. The excess flow of the pump is relief through the low pressure side of the relief valve against ambient pressure and recycled back to the HPLC bottle.

The module MFC-3 shown in Figure 5.4 c) is used when experiments are carried in the CPR. Both MFC-1 and MFC-2 flows are set to achieve a desired inlet composition. Then, the overall flow of mixed MeOH/HP/IS and Pr is directed to the module MFC-3. A small fraction of the overall flow is dosed to the CPR by

the MFC-3 to obtain the desired contact time in the CPR, while the excess flow is expanded in a flash unit and disposed. The pressure of the feed to the module MFC-3 is regulated by a back pressure regulator BPR-2.
The sampling in both reactor is achieved by a small pressure difference between the reactor and the sampling line which leads a fraction of the flow (usually below 10% of the total flow) continuously through the analytic system. The pressure drop in the sampling line is controlled by an additional back pressure regulator BPR-3. The sample flow is continuously monitored by a mass flow meter MFM-1. All sampling lines are 400 μm ID to minimize dead volumes. The sampling proceeds from the outlet of the reactor and is moved progressively towards the inlet. The pressure in the sampling line is kept always well above 17 bar to ensure that the Pr remains entirely in the liquid phase. After chromatographic analysis, the liquid sample is expanded in a small vessel and the liquid is collected for determination of the HP concentration by Potentiometric Titration with Cerium (IV) Sulfate and the identification of side products by GC/MS screening. In the case of the CPR, the HP concentration is determined at the inlet and outlet of the catalytic bed while the middle points are calculated by stoichiometry. After reaction the unconverted Pr, HP, products of reaction and spatial sample are expanded in a flash unit against atmospheric pressure. The off-gas is treated in a catalytic afterburner while the liquids are collected and disposed.

5.2 Catalyst Characterization

In Figure 5.5 a) the diffraction patterns of the catalyst TS-1/SiO_2 is shown. The peaks at 24.4° and 29.3° show the incorporation of the Ti atoms into the MFI framework and the change from monoclinic symmetry of Silicalite-1 to an orthorhombic symmetry of Titanium Silicalite-1 [63, 69]. In Figure 5.5 b) the FT-IR spectrum of the TS-1 catalyst powder is shown. The band at 960 cm^{-1} is related to the incorporation of Ti into the framework and has been assigned to the asymmetric stretching of the [TiO_4] units [70]. The BET analysis of the adsorption isotherms shows that the surface area of the pure catalyst powder is 422 m^2/g, the surface area of the pure inorganic SiO_2 support is 623 m^2/g and the TS-1/SiO_2 catalyst splits is 451 m^2/g. The slightly higher surface area of the catalyst splits

Table 5.3: Main Characteristics of feed modules

MFC-1 Module	Value	Supplier (Art.Nr.)
Cori-Flow mass flow controller	1-50 $[\frac{g}{h}]$	Bronkhorst (ML120V00-RAD-11-0-S)
Control valve (reference gas)	40 - 17,35 [bar] (back-fore pressure)	Bronkhorst (C2I-IIU-11-K)
Equilibar	51.7 [bar] , 175 [°C] (max P,T)	Pressure control solutions (LF1SNN12B-NSMP750T175G10VVB)
Dosing fluid	Liquefied Pr	-
MFC-2 Module	Value	Supplier (Art.Nr.)
Cori-Flow mass flow controller	8-400 $[\frac{g}{h}]$	Bronkhorst (ML120V00-RAD-11-0-S)
Control valve (reference gas)	40 - 17,35 [bar] (back-fore pressure)	Bronkhorst (C2I-IIU-11-K)
Dosing fluid	Mixture MeOH/HP/IS	-
MFC-3 Module	Value	Supplier (Art.Nr.)
Cori-Flow mass flow controller	0.125-12.5 $[\frac{g}{h}]$	Bronkhorst (ML120V00-RAD-C1-0-S)
Control valve (reference gas)	40 - 17,35 [bar] (back-fore pressure)	Bronkhorst (C2I-IIU-1C-K)
Dosing fluid	Mixture MeOH/HP/IS/Pr	-
Pump Module	Value	Supplier (Art.Nr.)
HPLC Pump	0-10 $[\frac{ml}{min}]$	Knauer (Azura P 4.1S)
MFM-1 Module	Value	Supplier (Art.Nr.)
Cori-Flow mass flow meter	0.05-5.0 $[\frac{g}{h}]$	Bronkhorst (ML120V00-RAD-CC-0-S)
Dosing fluid	Spatial sample	-

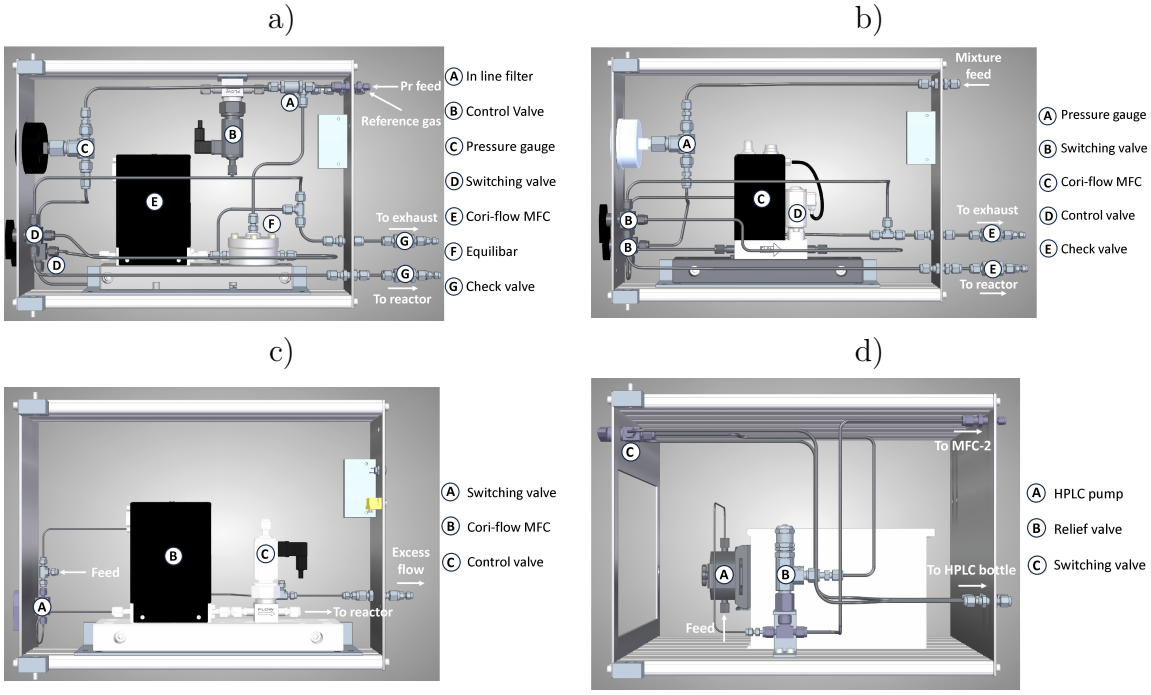

Figure 5.4: 3D model of MFC-1, MFC-2, MFC-3 and pump modules

relative to the pure catalyst powder is attributed to the higher surface area of the support. In Figure 5.6 a), b), c) SEM images of the catalyst extrudates, pure TS-1 particles and catalyst splits are respectively shown.

5.3 POC Coating

In Figure 5.7 and Figure 5.8 the POCs dip coating cycles followed by a drying step at 50°C are shown. A total of 6 coating cycles were performed (3 coatings per side). The weight of the POCs were measured before and after coating/drying to be able to determine the mass of the deposited layer. Upon calcination only a wight loss of 2%-3% was measured. Under the assumption that the ratio of catalyst powder to colloidal silica of the prepared coating solution remained constant during the dip-coating procedure the amount of catalyst loading was calculated. The results of the dip-coating procedure are summarized in Table 5.4.

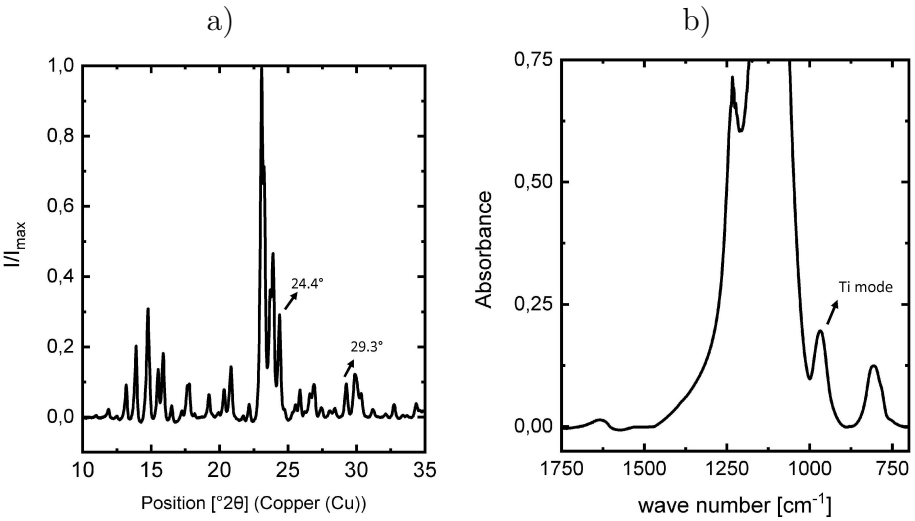

Figure 5.5: a) TS-1/SiO_2 catalyst diffraction pattern, b) FT-IR spectrum of the TS-1 catalyst powder

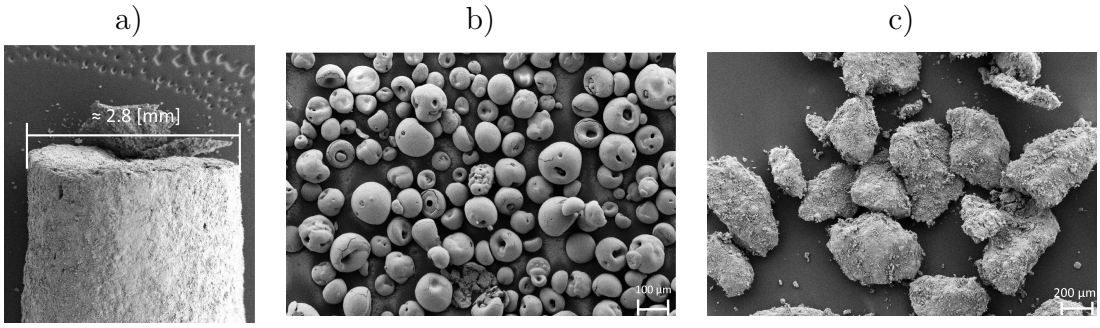

Figure 5.6: SEM images of a) Catalyst pellet b) TS-1 agglomerated particles c) Catalyst splits

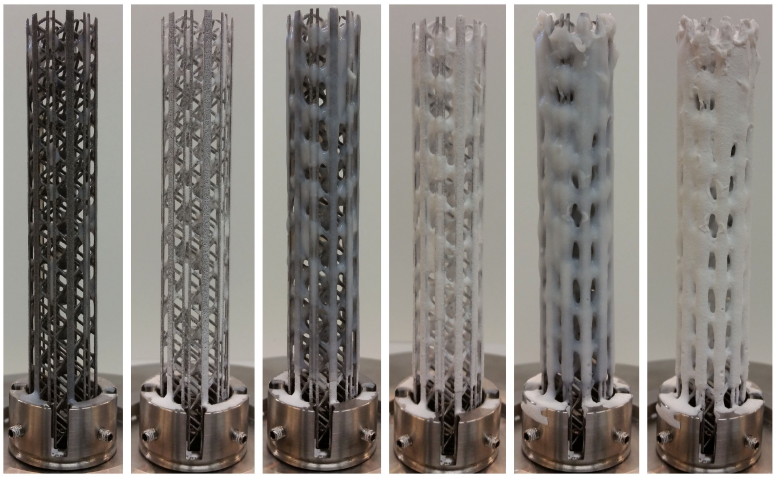

Figure 5.7: Dip coating cycles 1 to 3. Taken from [146]

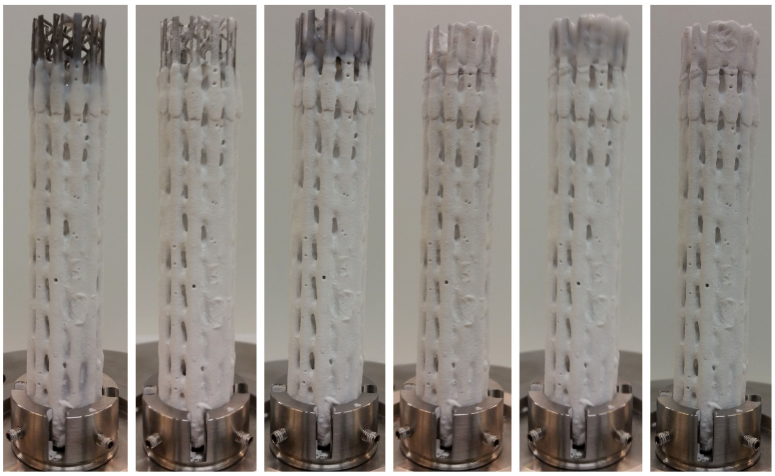

Figure 5.8: Dip coating cycles 4 to 6. Taken from [146]

Table 5.4: Results of dip-coating procedures. Taken from [146]

	Total weight POCs [g]	Coated layer weight [g]	Catalyst loading [g]
POC-1	17,85	9,13	4,1
POC-2	20,46	11,77	5,3

5.4 Determination of products of reaction, mass balance

For the determination of the products of reaction, a experimental run was performed on the pilot scale spatial profile reactor with the parameters highlighted in Table 5.5. This reactor allows to perform the reaction with long contact times (e.g: LHSV$\approx$0.7 h^{-1}). The aim is to intentionally promote the side reaction of PO to acquire information about the reaction network and products formed. During the experiment samples of the reactor effluents were taken at different times and analyzed by GC/MS screening. An example GC chromatogram with the identified peaks via MS-screening is shown in Figure 5.9.

Table 5.5: List of parameters of experiment GC/MS

Experiment	T,P [°C, bar]	[Pr]	[HP]	LHSV $[h^{-1}]$	m_{cat} [g], (L mm)	m_{MFC-1} [g/h]	m_{MFC-2} [g/h]	m_{MFC-3} [g/h]	Feed wt%	SS [h]
GC/MS	40, 30	0.6	2.0	0.7	33 (400)	2	64	-	73/24/3	12

Feed composition in (MeOH/HP/Pr) [wt%]. SS= Steady state

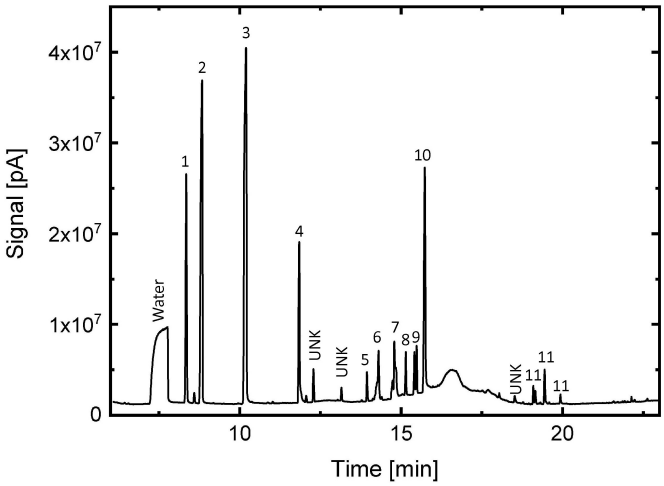

Figure 5.9: GC/MS data, taken from [176]

The acquired data in Figure 5.9 from the Agilent Gas Chromatograph 6890N in combination with the Mass Spectrometer MSD 5975 shows that the side products of reaction are (1) methoxyacetone, (2) 1-methoxy-2-propanol, (3) 2-methoxy-1-propanol, (4) hydroxyacetone and (10) propylene glycol. Also in lower amount (7) formic acid, (5) methylformate, (6, 8, 9) dipropyleneglycol methylether isomers and (11) dipropyleneglycol isomers were detected. Based on the GC-MS screening data, the main peaks seen in the chromatograph data, the availability of chemicals and the reactions network previously reported in the scientific literature the following reactions were considered to perform a mass balance of the system.

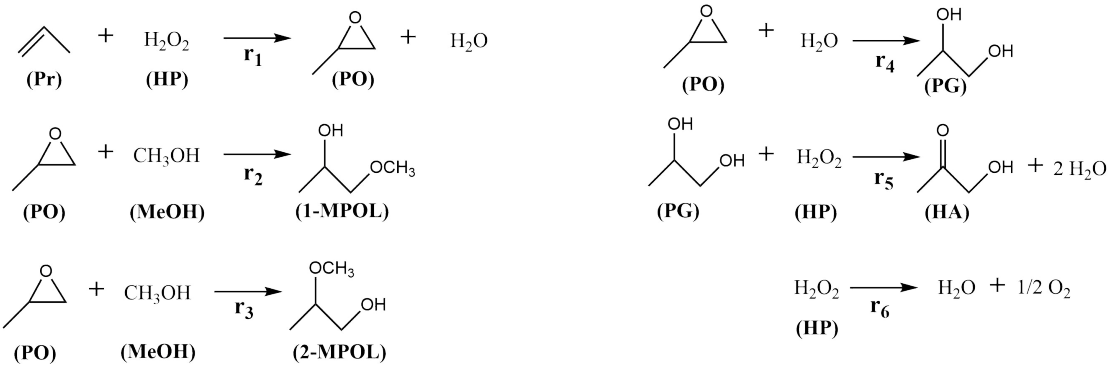

Eq. 5.1: Considered Reactions for Mass Balance

In this case, a new reaction for the formation of HA was added (reaction r_5). This reaction is not reported in the scientific literature, but is one of the secondary side products detected by our GC/MS screening. Based on this proposed reaction system, the following stoichiometric analysis was done:

$$\nu_{\mathrm{ij}} \cdot \dot{\xi}_{\mathrm{jv}} = \Delta[C_i] = \begin{array}{c} \\ \mathrm{Pr} \\ \mathrm{HP} \\ \mathrm{PO} \\ \text{1-MPOL} \\ \text{2-MPOL} \\ \mathrm{PG} \\ \mathrm{HA} \\ \mathrm{H_2O} \\ \mathrm{O_2} \\ \mathrm{MeOH} \end{array} \begin{array}{c} \begin{array}{cccccc} \mathrm{r_1} & \mathrm{r_2} & \mathrm{r_3} & \mathrm{r_4} & \mathrm{r_5} & \mathrm{r_6} \end{array} \\ \begin{pmatrix} -1 & 0 & 0 & 0 & 0 & 0 \\ -1 & 0 & 0 & 0 & -1 & -1 \\ 1 & -1 & -1 & -1 & 0 & 0 \\ 0 & 1 & 0 & 0 & 0 & 0 \\ 0 & 0 & 1 & 0 & 0 & 0 \\ 0 & 0 & 0 & 1 & -1 & 0 \\ 0 & 0 & 0 & 0 & 1 & 0 \\ 1 & 0 & 0 & -1 & 2 & 1 \\ 0 & 0 & 0 & 0 & 0 & 1/2 \\ 0 & -1 & -1 & 0 & 0 & 0 \end{pmatrix} \end{array} \cdot \begin{pmatrix} \dot{\xi}_{\mathrm{v1}} \\ \dot{\xi}_{\mathrm{v2}} \\ \dot{\xi}_{\mathrm{v3}} \\ \dot{\xi}_{\mathrm{v4}} \\ \dot{\xi}_{\mathrm{v5}} \\ \dot{\xi}_{\mathrm{v6}} \end{pmatrix} = \begin{pmatrix} \Delta[Pr] \\ \Delta[HP] \\ \Delta[PO] \\ \Delta[1MPOL] \\ \Delta[2MPOL] \\ \Delta[PG] \\ \Delta[HA] \\ \Delta[H_2O] \\ \Delta[O_2] \\ \Delta[MeOH] \end{pmatrix}$$

Where j = reactions 1 to 6, i = chemical species 1 to 10, ν_{ij} = stoichiometric coefficient matrix of component i in reaction j, $\dot{\xi}_{jv}$ = volume based extent of reaction of reaction j = $\frac{\dot{\xi}_j}{\dot{V}}$ in $[mol\ l^{-1}]$, $\dot{\xi}_j = \frac{\Delta \dot{n}_i}{\nu_{ij}}$ in $[mol\ s^{-1}]$ is the extent of reaction, $\Delta\,[C_i]$ = change in molar concentration of component i = $\frac{\dot{n}}{\dot{V}}$ in $[mol\,l^{-1}]$,

$\dot{V}$ = volumetric flow in $[l\ s^{-1}]$ and $\dot{n}_i$ = is the molar flow of component i in $[mol\ s^{-1}]$. The concentration change of every chemical species can be calculated based on the extent of the reactions in which they are involved

$$\Delta[Pr]=-\dot{\xi}_{v1}$$
$$\Delta[HP]=-\dot{\xi}_{v1}-\dot{\xi}_{v5}-\dot{\xi}_{v6}$$
$$\Delta[PO]=\dot{\xi}_{v1}-\dot{\xi}_{v2}-\dot{\xi}_{v3}-\dot{\xi}_{v4}$$
$$\Delta[1MPOL]=\dot{\xi}_{v2}$$
$$\Delta[2MPOL]=\dot{\xi}_{v3}$$
$$\Delta[PG]=\dot{\xi}_{v4}-\dot{\xi}_{v5}$$
$$\Delta[HA]=\dot{\xi}_{v5}$$
$$\Delta[H_2O]=\dot{\xi}_{v1}-\dot{\xi}_{v4}+2\dot{\xi}_{v5}+\dot{\xi}_{v6}$$
$$\Delta[MeOH]=-\dot{\xi}_{v2}-\dot{\xi}_{v3}$$

And the extent of reaction of each of the considered reactions are:

$$\dot{\xi}_{v1}=-\Delta[Pr]$$
$$\dot{\xi}_{v2}=\Delta[1MPOL]$$
$$\dot{\xi}_{v3}=\Delta[2MPOL]$$
$$\dot{\xi}_{v4}=\Delta[PG]+\Delta[HA]$$
$$\dot{\xi}_{v5}=\Delta[HA]$$
$$\dot{\xi}_{v6}=-\Delta[HP]+\Delta[Pr]-\Delta[HA]$$

If the reactions considered are enough to describe the process, then the following conditions should be fulfilled:

$$ESM \cdot \Delta[i] \approx 0$$

$$\begin{array}{c} \\ \text{C} \\ \text{H} \\ \text{O} \end{array} \begin{array}{c} \begin{array}{cccccccccc} \text{Pr} & \text{HP} & \text{PO} & \text{1-MPOL} & \text{2-MPOL} & \text{PG} & \text{HA} & \text{H}_2\text{O} & \text{O}_2 & \text{MeOH} \end{array} \\ \begin{pmatrix} 3 & 0 & 3 & 4 & 4 & 3 & 3 & 0 & 0 & 1 \\ 6 & 2 & 6 & 10 & 10 & 8 & 6 & 2 & 0 & 4 \\ 0 & 2 & 1 & 2 & 2 & 2 & 2 & 1 & 2 & 1 \end{pmatrix} \end{array} \cdot \begin{pmatrix} \Delta[Pr] \\ \Delta[HP] \\ \Delta[PO] \\ \Delta[1MPOL] \\ \Delta[2MPOL] \\ \Delta[PG] \\ \Delta[HA] \\ \Delta[H_2O] \\ \Delta[O_2] \\ \Delta[MeOH] \end{pmatrix} \approx \begin{pmatrix} 0 \\ 0 \\ 0 \end{pmatrix}$$

Then, the carbon balance at each measured position as percentage of the total moles of carbon atoms fed to the reactor can be calculated as follows:

$$\%\text{Carbon balance}_z = \frac{\Delta\text{Carbon}_z}{\text{Carbon}_0} \times 100$$

This percentage gives an estimation of how near is the calculated carbon balance at the coordinate (z) from closure and is used as criterion for determining the validity of the experiments and analytical methods.

Table 5.6: Main parameters of experimental runs

Experiment	T,P [°C, bar]	[Pr]	[HP]	LHSV [h^{-1}]	m_{cat} [g], (L [mm])	m_{MFC-1} [g/h]	m_{MFC-2} [g/h]	m_{MFC-3} [g/h]	Feed wt%	SS [h]
Ext. Lim.	40, 20	0.6	0.3	3.0	0.19 (42)	1.6	48	1.2	93/4/3	18.0
Fresh Cat.	40, 20	0.6	2.0	3.0	0.15 (37)	2	64	1.1	73/24/3	75.5
CPR-1	40, 20	0.6	2.0	3.0	0.15 (37)	2	64	1.1	73/24/3	22.3
CPR-2	40, 20	0.6	2.0	6.0	0.15 (34)	2	64	2.1	73/24/3	18.0
CPR-3	40, 20	0.6	2.0	12.0	0.15 (35)	1.5	48	4.35	73/24/3	28.3

Feed composition in (MeOH/HP/Pr) [wt%]. SS= Steady state

5.5 Experimental measurements in compact profile reactor (CPR)

In Figure 5.10 a) a typical packing in a CPR is shown. For liquid phase reactions, the flow is fed from bottom to top to avoid channeling of the liquid which provides a uniform flooding of the reactor. The back shield length is usually longer to provide a pre-mixing and pre-heating of the chemicals until the reaction temperature. The front shield is used to compact the catalyst bed and fix it in position. The total effective measuring range of the CPR is 60 [mm]. The reactor coordinate $z = 0$ corresponds to the start of the catalyst bed, while negative coordinates corresponds to the back shield. The set of experimental runs and their relevant experimental parameters are summarized in Table 5.6. In all experiments shown in this work, the feed composition is such that the reaction is conducted on a single liquid phase regime as shown in Figure 5.10 b).

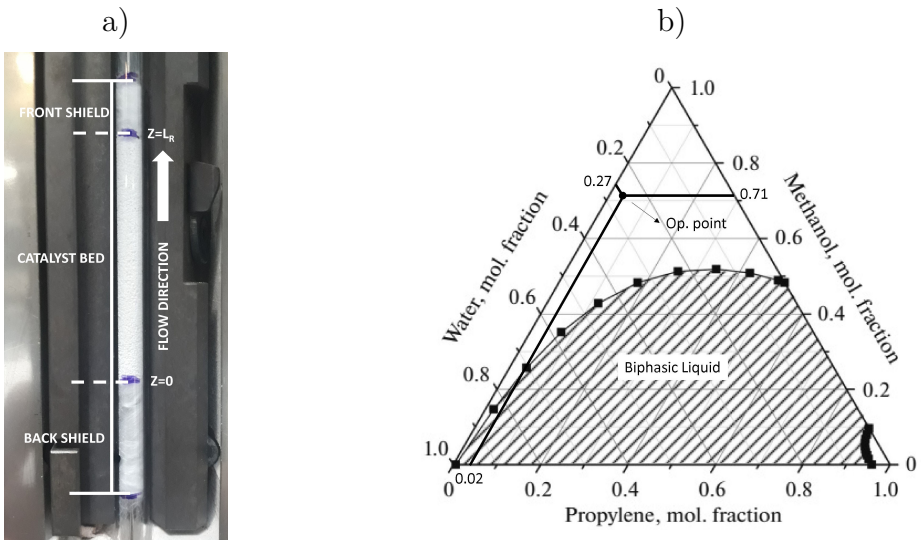

Figure 5.10: a) CPR Reactor geometry and b) Typical operation point of experimental runs.

5.6 Experimental determination of external mass transfer limitations

To experimentally determine if the measurements are free of film transport limitations that may dominate over the reaction rate, the volumetric flow was systematically varied while maintaining the space time constant. The main parameters of the experiment are shown in Table 5.6 for the Ext. Lim. experimental run. In a conventional fixed bed reactor, varying the volumetric flow while keeping the space time constant requires a systematic change of the catalyst mass. Therefore, the experimental determination of external mass transfer limitations requires several experimental runs, one per each bed length. In contrast to the conventional approach, in a spatial profile reactor this kind of experiment can be performed in a single measurement. The length of the reactor can be systematically changed by simply moving the sampling position to a different coordinate of the reactor. Then, the volumetric flow can be modified accordingly to maintain a constant space time. The procedure of this experimental run is highlighted in Figure 5.11.

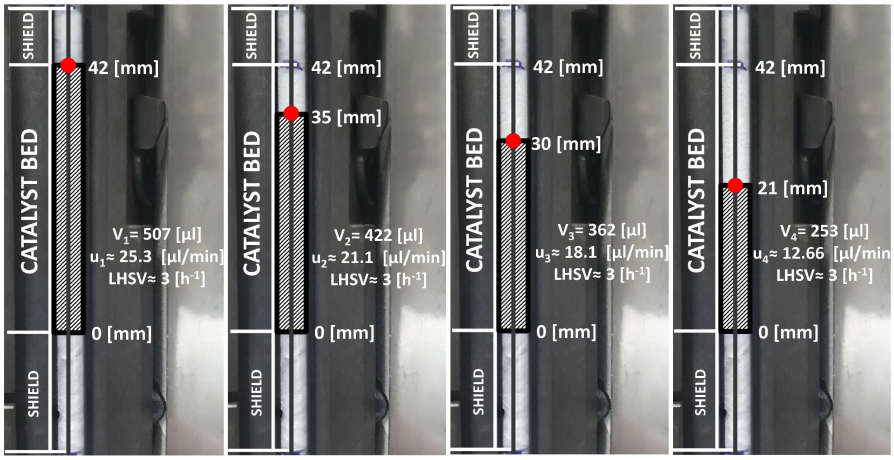

Figure 5.11: Mass Transfer limitation experiment, 3 hours between each measurement

For the measurement of HP via potentiometric titration at least 500 μl of sample are required. The small specific flow rate required to achieve the necessary contact time restricts the measurement of HP concentration to positions at which the sampling orifice is located for a long period of time, namely the inlet and outlet of the reactor. In contrast, measuring Pr concentration via gas chromatography requires a smaller sample volume. For this reason, in this experiment Pr was fed to the reactor in stoichiometric excess with respect to HP which allowed fast monitoring of the conversion with minimal sample amount as the volumetric flow was systematically varied.

In Figure 5.12 a) the conversion of Pr and HP as a function of the volumetric flow at constant space time of $LHSV = 3.0\,[h^{-1}]$ is shown. Between each measured point a total of 3 hours was waited for the stabilization of the reaction to the newly set volumetric flow. Both the conversion of Pr and HP shown in Figure 5.12 a) remained relatively constant for the whole extent of volumetric flows investigated in the experiment. Because the conversion is independent of the superficial velocity of the bulk fluid it is concluded that the external mass transport limitations under the experimental conditions can be considered negligible. In Figure 5.12 b) the concentration of the species involved in the main epoxidation reaction are shown. It can be observed that both the concentration of Pr and HP remained constant. A different behavior can be observed in the case of PO, in which its concentration decreases as the superficial velocity decreases. This can be explained by the fact

that the rate of side products formation increases with the temperature of reaction. The heat transport coefficient inside of the reactor depends on the superficial velocity of the bulk fluid, in consequence a decrease of the superficial velocity underlines a worsening of the heat transport and an increase of the temperature.

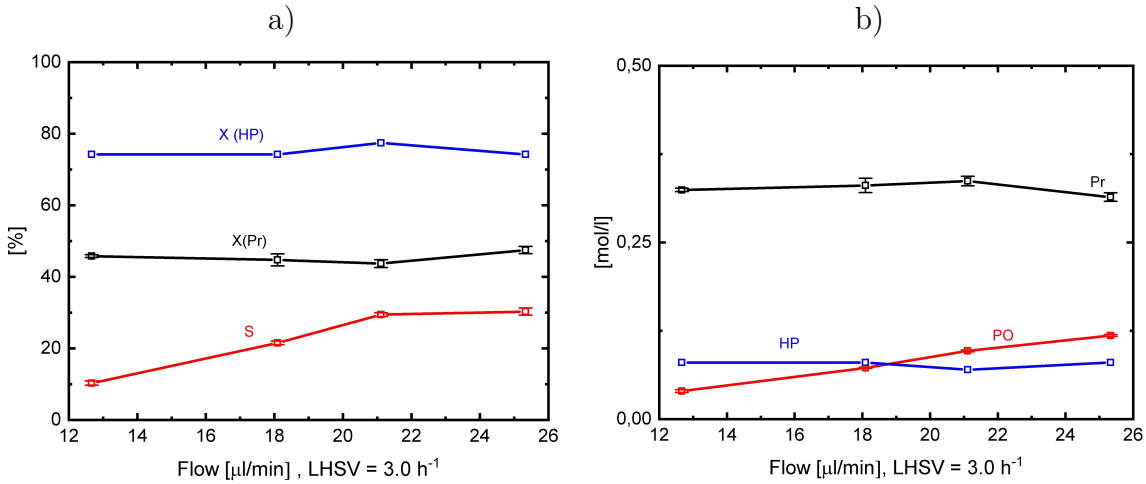

Figure 5.12: Experimental data Ext. Lim.. a) HP conversion (X_{HP}), Pr conversion (X_{Pr}) and PO selectivity (S) , b) Main products concentrations. Measured at constant space time LHSV = 3 [h^{-1}], 40°C and 20 bar pressure

The analytical evaluation of the criteria for external/internal heat and mass transport limitations as well deviations from ideal plug flow behavior are provided in the Appendix Section 7.1.

5.7 Determination of steady state

At the beginning of each experimental run the products distribution at the outlet of the catalyst bed was continuously monitored to determine at which point the reaction can be considered in steady state. In Figure 5.13 the Pr conversion (X), PO selectivity (S), the carbon balance closure and the products distribution as a function of time for a fresh catalyst sample are shown while the experimental parameters can be found in Table 5.6 Fresh Cat.. From the data, it can be observed that the catalyst undergoes an induction or activation period for a extent 75 [h]. In Figure 5.13 a) it can be observed that during the whole extent of this

period, the carbon molar flow measured at the outlet of the reactor is not equal to the carbon molar flow being fed to the reactor leading to a discrepancy in the carbon balance closure that reaches a minimum of 20 % after about 75 [h]. In other words, while the amount of fed carbon atoms from Pr are being completely converted there is no direct measurement of products of reaction that contain said converted carbon atoms at the outlet of the reactor. This may suggest that the moles of carbon being fed to the reactor are being accumulated in the system in the form of side products entrapped within the catalyst pore system. It is possible to estimate the mass accumulated in the system for the extent of the experiment by calculating the difference between the fed mass flow rate and the mass flow at the outlet of the catalyst bed ($\Delta\dot{m}[g\ h^{-1}] = \dot{m}_{outlet} - \dot{m}_{inlet}$) as a function of the induction/activation time and integrating it over time as shown in Figure 5.17 a). For the experimental run Fresh Cat. this amount corresponds to about 1.08 [g] in the time interval of 75 [h] that takes the carbon balance closure to reach 20 %. The average mass of catalyst used during the experiments is about 0.15 [g]. The estimated amount of 1.08 [g] is about 7.2 times larger than the total mass of catalyst used in this experiment, therefore a filling of the pores by products of reaction as only underlying mechanism to explain the observed phenomena is unlikely. Nevertheless, the reported pore volume of the TS-1 catalyst is 0.42 [$cm^3\,g^{-1}$] [86], which implies that for the mass of catalyst used in this experiment about 0.063 [cm^3] of free volume in the pores is available for products of reaction to be accumulated. The product of reaction with the highest density is PG being 1.04 [$g\ cm^{-3}$]. Hence, the amount of mass of PG that could be accumulated in the pore volume of the catalyst is about 0.065 [g]. In consequence, this explanation cannot fully elucidate the mechanism during the induction/activation period. Another possibility is that during the observed induction/activation period, products are formed that cannot be measured by the analytical system used in these experiments e.g: oligomers from PG and MPOL with high boiling point. The inlet of the GC system used on this study can reach a maximal temperature of 220 °C, which means that if there is any product of reaction in the analyte mixture with a boiling point higher than 220 °C, said product cannot be vaporize before being injected into the GC columns. Most likely, the observed behavior for the fresh catalyst sample can be attributed to both the accumulation of products of reaction in the pores of the

catalyst and the formation of products that cannot be measured by the analytical system used in this work.

In Figure 5.13 b) the products distribution during the induction/activation period is shown. The side products of reaction 1-MPOL, 2-MPOL, PG reach their maximal concentration after about $5\,[h]$ of reaction time and then slowly start to decrease during the remaining time of the experiment. In particular, the observed discontinuities on the concentration of 2-MPOL can be attributed to the fact that the peak of this product is near the tail of the solvent peak making its quantification difficult. The retention time difference between these two peaks was extended for the following measurements in this study. In contrast to the concentrations of side products, the concentration of the main product PO increases slowly and steadily. After about $65\,[h]$ of reaction time, the rate of increase of concentration of PO starts to slow down and becomes asymptotic to a maximum value of $[PO] = 0.42[mol\ l^{-1}]$. This slow increase on the PO concentration may suggest that, during this induction/activation period the fresh catalyst sample slowly and progressively starts to catalyze the target reaction. The selectivity (S) and the carbon balance closure strongly depend on the PO concentration, and for this reason, these two parameters exhibit the same trend as for PO. Due to the fact that after $75\,[h]$ of reaction time the carbon balance closure did not reached an acceptable value of less than 10 % the experiment was suspended.

An interesting behavior is observed once the catalyst undergoes a long induction/activation period, or in simple words when the catalyst sample is not fresh and was previously in contact with the reactive mixture. In Figure 5.14, Figure 5.15, Figure 5.16 the Pr conversion (X), PO selectivity (S), the carbon balance closure and the products distribution as a function of time for the experimental runs CPR-1, CPR-2 and CPR-3 are shown. The relevant parameters for these experimental runs can be found on Table 5.6 under the same name respectively. For these experimental runs the same catalyst than for Fresh Cat. was used. From the data, it can be observed that once the catalyst has been subjected to a long induction/activation period of $75\,[h]$, the successive measurements CPR-1, CPR-2 and CPR-3 require in average approximately 24 hours for the carbon balance closure to reach an acceptable value of less than 10%. Nonetheless, the mechanism is the same and the difference of mass between the inlet and outlet of the reactor

shown in Figure 5.17 a), b) and Figure 5.18 a), b) cannot be fully explained solely by an accumulation mechanism in the pores of the catalyst. The fact that catalyst samples previously exposed to the reaction mixture exhibited a significant shorter induction/activation time may suggest that the catalyst requires a pretreatment before performing the reaction. The exact mechanism of this induction/activation period remains unclear and requires further experimental investigation.
Previously reported required time to reach steady state was about 2 hours [90] or 5-7 reactor volumes [110]. In our study the reaction was considered in steady state when the carbon balance closure was equal or below 10 %, which required about 24 hours of reaction time for a catalyst sample previously in contact with the reactive mixture.
The mechanism observed during the induction/activation period is not fully understood and requires further experimental data. Most likely, the observed behavior can be attributed to both contributions of accumulation of products of reaction in the pores of the catalyst and the formation of products that cannot be measured by the analytical system used in this work.

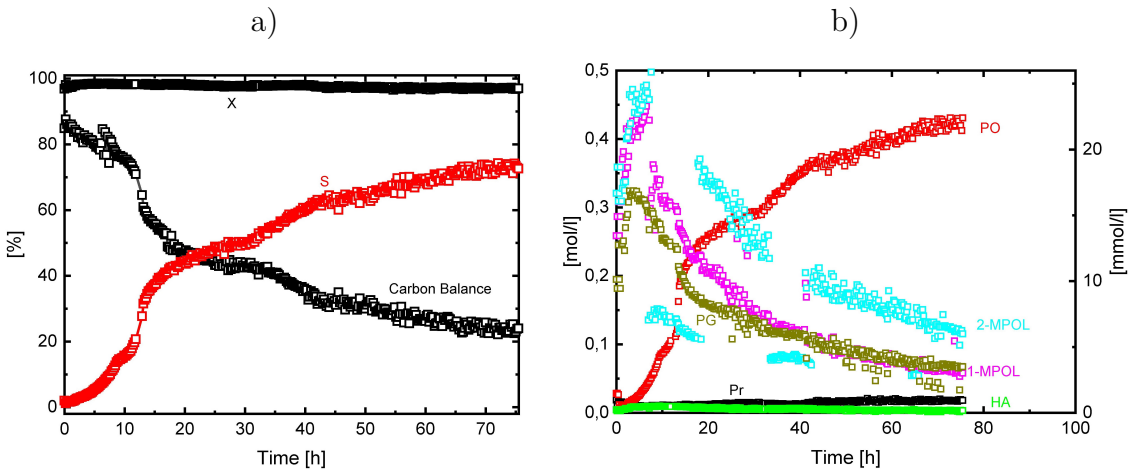

Figure 5.13: Transition towards steady state for Fresh Cat.: Pr conversion (X), PO selectivity (S), carbon balance closure and products distribution. Measured at 40°C and 20 bar pressure. Note: main products Pr and PO in $[mol\ l^{-1}]$ (left axis), side products 1-MPOL, 2-MPOL, PG and HA in $[mmol\ l^{-1}]$ (right axis).

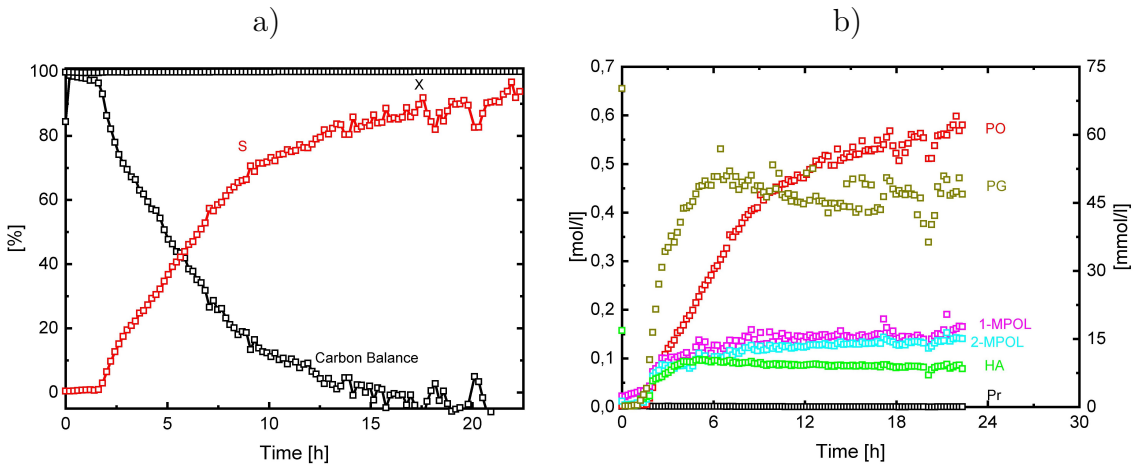

Figure 5.14: Transition towards steady state for CPR-1: Pr conversion (X), PO selectivity (S), carbon balance closure and products distribution. Measured at 40°C and 20 bar pressure. Note: main products Pr and PO in $[mol\ l^{-1}]$ (left axis), side products 1-MPOL, 2-MPOL, PG and HA in $[mmol\ l^{-1}]$ (right axis).

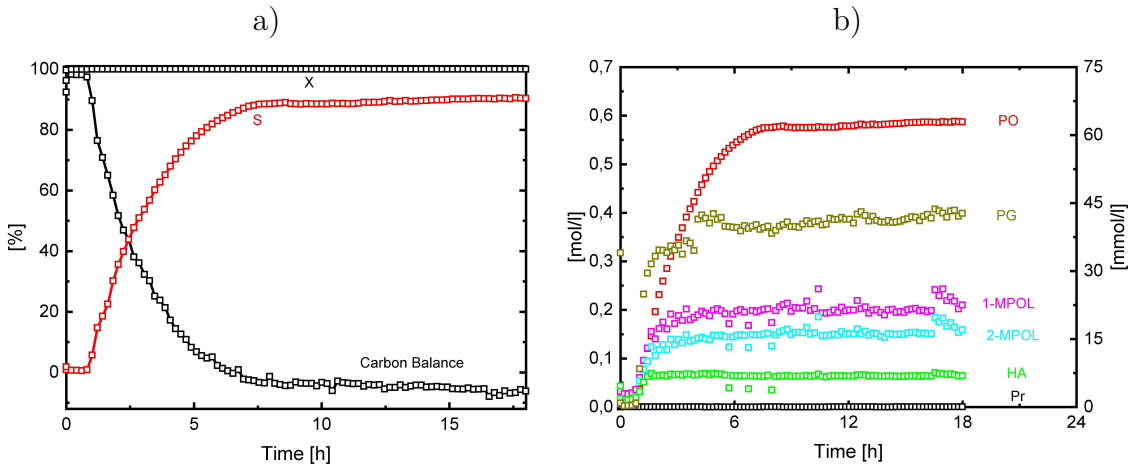

Figure 5.15: Transition towards steady state for CPR-2: Pr conversion (X), PO selectivity (S), carbon balance closure and products distribution. Measured at 40°C and 20 bar pressure. Note: main products Pr and PO in $[mol\ l^{-1}]$ (left axis), side products 1-MPOL, 2-MPOL, PG and HA in $[mmol\ l^{-1}]$ (right axis).

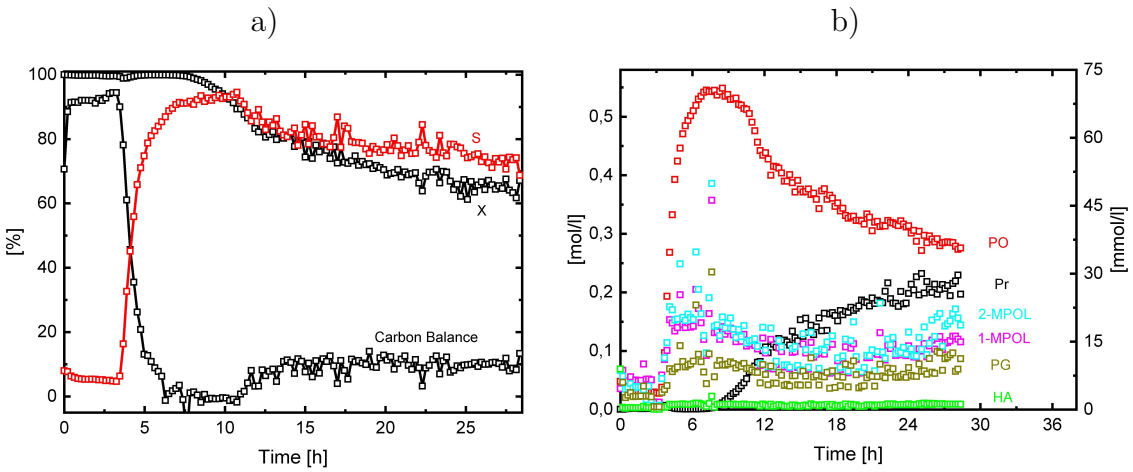

Figure 5.16: Transition towards steady state for CPR-3: Pr conversion (X), PO selectivity (S), carbon balance closure and products distribution. Measured at 40°C and 20 bar pressure. Note: main products Pr and PO in $[mol\ l^{-1}]$ (left axis), side products 1-MPOL, 2-MPOL, PG and HA in $[mmol\ l^{-1}]$ (right axis).

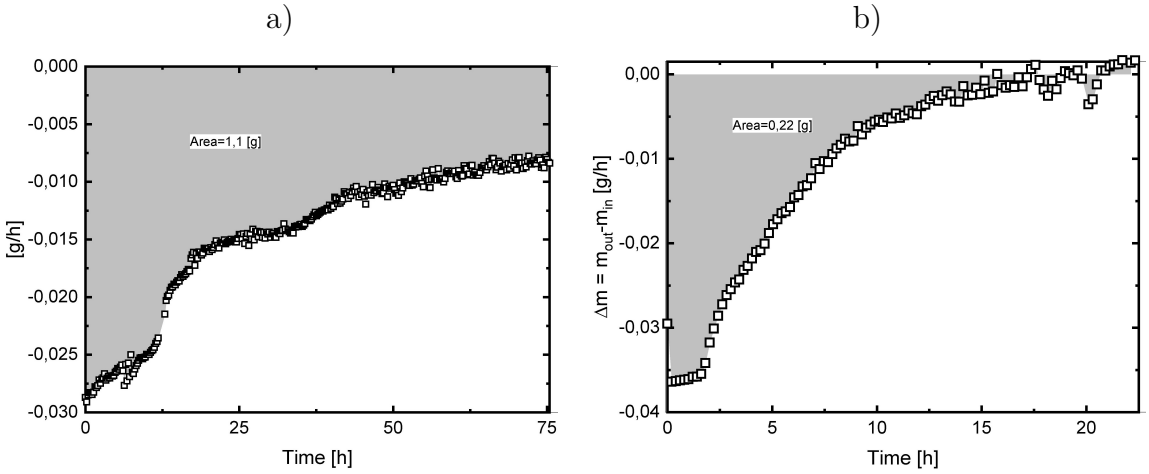

Figure 5.17: Difference between outlet and inlet mass flow rates $\Delta\dot{m} = \dot{m}_{outlet} - \dot{m}_{inlet}$ as a function of time during the transition towards steady state. a) Fresh Cat, b) CPR-1. Measured at 40°C and 20 bar pressure.

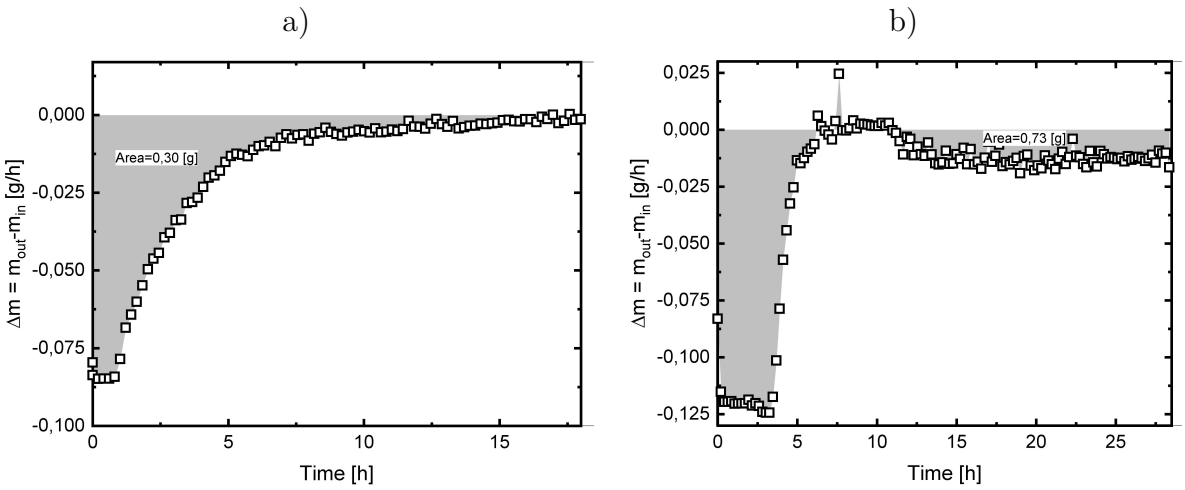

Figure 5.18: Difference between outlet and inlet mass flow rates $\Delta\dot{m} = \dot{m}_{outlet} - \dot{m}_{inlet}$ as a function of time during the transition towards steady state. a) CPR-2, b) CPR-3. Measured at 40°C and 20 bar pressure.

5.8 Spatially resolved concentration profiles

After the criterion for the steady state was reached, the spatially resolved concentration profiles of the experimental runs CPR-1, CPR-2 and CPR-3 were measured. These experimental runs were measured at the same reaction conditions, while systematically varying the space time from $LHSV = 3.0[h^{-1}]$, $LHSV = 6.0[h^{-1}]$ and $LHSV = 12.0[h^{-1}]$ respectively.

In Figure 5.19 and Figure 5.20 the data for experimental runs CPR-1 and CPR-2 is shown. In both cases, the concentration profile for the main epoxidation reaction shows that Pr is completely consumed while HP is about 32% converted with a selectivity towards PO of 86 % and 88 % for CPR-1 and CPR-2 respectively. The loss of selectivity as the contact time increases from $LHSV = 6.0[h^{-1}]$ to $LHSV = 3.0[h^{-1}]$ can be attributed to a longer contact time of PO with the surface of the catalyst were can undergo ring opening reactions and to an increase on the local temperature due the reduction of the superficial flow velocity. In both cases the predominant side product is PG. In Figure 5.21 the measured data for CPR-3 at $LHSV = 12.0[h^{-1}]$ is shown. In this case Pr reaches about 63 % conversion while HP is about 17 % converted with a PO selectivity of 86 %. The

predominant side products in this case are the isomers of MPOL.
An interesting observation is that in all cases a pseudo-zeroth-order behavior of the main epoxidation reaction is observed. Several DFT simulations have found that the rate determining step in the Pr epoxidation is the adsorption and successive dissociation of HP on $Ti(SiO)_3OH$ sites [104–107]. Clerici in 1991 observed that the reaction approximates a zeroth-order behavior for high HP concentrations [80]. As pointed out by Taramasso in 1983, the amount of Ti atoms that can be inserted in the framework of the catalyst is limited to 3 %wt TiO_2 [63]. Additionally, not all Ti sites are accessible by the chemicals which means that the amount of molecules of HP and Pr far exceed the number of available Ti sites. If the reaction rate is given by the dissociative adsorption of HP and the concentration of HP molecules far exceed the number of available Ti sites on the surface of the catalyst, the epoxidation rate will be limited by the maximal speed at which available Ti sites can adsorb and dissociate HP molecules, which can explain the observed pseudo-zeroth-order behavior. Moreover, it is interesting to notice that the slope of the pseudo-zeroth-order reaction remains constant independently of the local concentration of PO. In this sense, the change in the rate of reaction occurs only at the end of the catalyst bed when Pr approaches total consumption. This observation may indicate that, under the conditions in which the experiments were performed, the competitive adsorption of PO does not play a significant role in the epoxidation rate. Regarding the formation of side products it can be seen in Figure 5.19 b) for CPR-1 and Figure 5.20 b) for CPR-2 that in the first 5-15 $[mm]$ of the catalyst bed the initial rate of formation is faster for the species 1-MPOL and 2-MPOL. As the reaction progress there is a switch and PG starts to be formed predominantly. In the case of Figure 5.21 b) for CPR-3, the side products concentrations are so low that this behavior could not be measured. Previous publications reported that the predominant side products are 1-MPOL and 2-MPOL [84], [83].
In Figure 5.19 d) for CPR-1, Figure 5.20 d) for CPR-2 and Figure 5.21 d) for CPR-3 the carbon balance closure as a function of the coordinate (z) is shown. It can be observed that for the experimental run CPR-1 the carbon balance closure is well below 10 %, and remains more or less constant for the whole length of the reactor. In contrast, for CPR-2 and CPR-3 the carbon balance closure is also

below 10% but increases toward the outlet of the catalyst bed. This increase in the carbon balance closure can be attributed to a small leakage on the sample injection valves of the analytical device used in this study, possibly after the experimental measurement CPR-1. Through this leakage a small flow of sample at reaction pressure can flow continuously to the low pressure side of the analytical device. In this case, low boilers such as Pr and PO can be easily removed by the flow of hot carrier gas continuously purging the loops, but higher boilers such as PG, the isomers of MPOL and oligomers may be retained for a longer period of time before being purged leading to the observed behavior. For CPR-2 and CPR-3 the carbon balance closure decreases for coordinates near the start of the catalyst bed. At these coordinates the concentration of side products such as PG, the isomers of MPOL and oligomers are at their lowest value. The TS-1 catalyst powder bought for this study has an average particle size of $0.3 - 0.5$ μm. The leakage was most likely caused by small catalyst particles scratching the surface of the sample injection valves. Suspended catalyst particles can be caused by the abrasive movement of the sampling capillary against the catalyst bed, which can cause small catalyst particles to detach from the support. These small particles are transported by the sampling flow and can damage downstream devices or clog the sampling capillary stopping the experiment. In this sense, it was found that it is necessary to use a quartz liner between the sampling capillary and the catalyst bed to avoid contact between both, the sampling capillary and the catalyst bed, during the movement of the spatial sampling system.

In all cases the selectivity remained more or less constant throughout the catalyst bed and has been extrapolated back for coordinates corresponding to the beginning of the reactor as shown by the dashed lines in the plots c) in Figure 5.19 for CPR-1, Figure 5.20 for CPR-2 and Figure 5.21 for CPR-3 respectively. As shown in the reaction network in Equation 3.2, the formation of side products are consecutive reactions to the formation of PO. In this sense, PO has to be first produced in order for the consecutive reactions to take place, therefore for coordinates near to the start of the catalytic bed a selectivity of 100% is expected. Nevertheless, the calculated selectivity from the analytical data tends to have lower values. This can be attributed to two factors. The first factor is the dispersion of the concentrations in axial direction due to the low specific flow rate. The second factor is the com-

plexity of the analyte mixture. The chemical species present in the mixture have a wide range of vapor pressures, being the most volatile compound Pr with 1158 kPa and the least volatile PG with 0.017 kPa at 25°C. The sample loops from the modified GC Agilent 7890B have a venting system that allows cleaning of the loops with hot carrier gas between measurements to avoid sample cross contamination. It was observed that less volatile components such as PG remained in the loops in trace amounts for a long period of time until they are completely purged out of the system. Due to the difference in volatility of the different chemical species and the fact that the sampling starts from the outlet of the bed and moves progressively towards the inlet, these trace amounts are carried over to coordinates corresponding to the beginning of the bed, which results in a lower selectivity.
The Pr epoxidation with HP is an exothermic reaction. Degussa (today Evonik AG) reported that it is not possible to work under isothermal conditions in a jacketed packed bed reactor and hotspots are formed inside the bed, thus increasing the rate of side product formation. [109]. In the experimental runs CPR-1, CPR-2 and CPR-3, no appreciable changes in the temperature along the reactor central axis were measured. This can be attributed to the conduction of heat through the stainless steel sampling capillary, which can flatten the temperature profile by providing an additional surface from which heat can be transported out of the system. To enable the measurement of spatially resolved temperature profiles, the material of the sampling capillary should be substituted by a material with low thermal conductivity such as fused silica.
Additionally, during the experimental runs liquid samples where taken at different reaction times for analysis via GC/MS screening. The data shows as primary side products of 1-MPOL, 2-MPOL and PG, and as secondary products HA and MA. The formation of HA and MA can be attributed to the reaction of both methoxypropanol isomers MPOL and PG with HP. Also formic acid, methylformate, dipropyleneglycol methylether isomers and dipropyleneglycol isomers were detected in trace amounts.

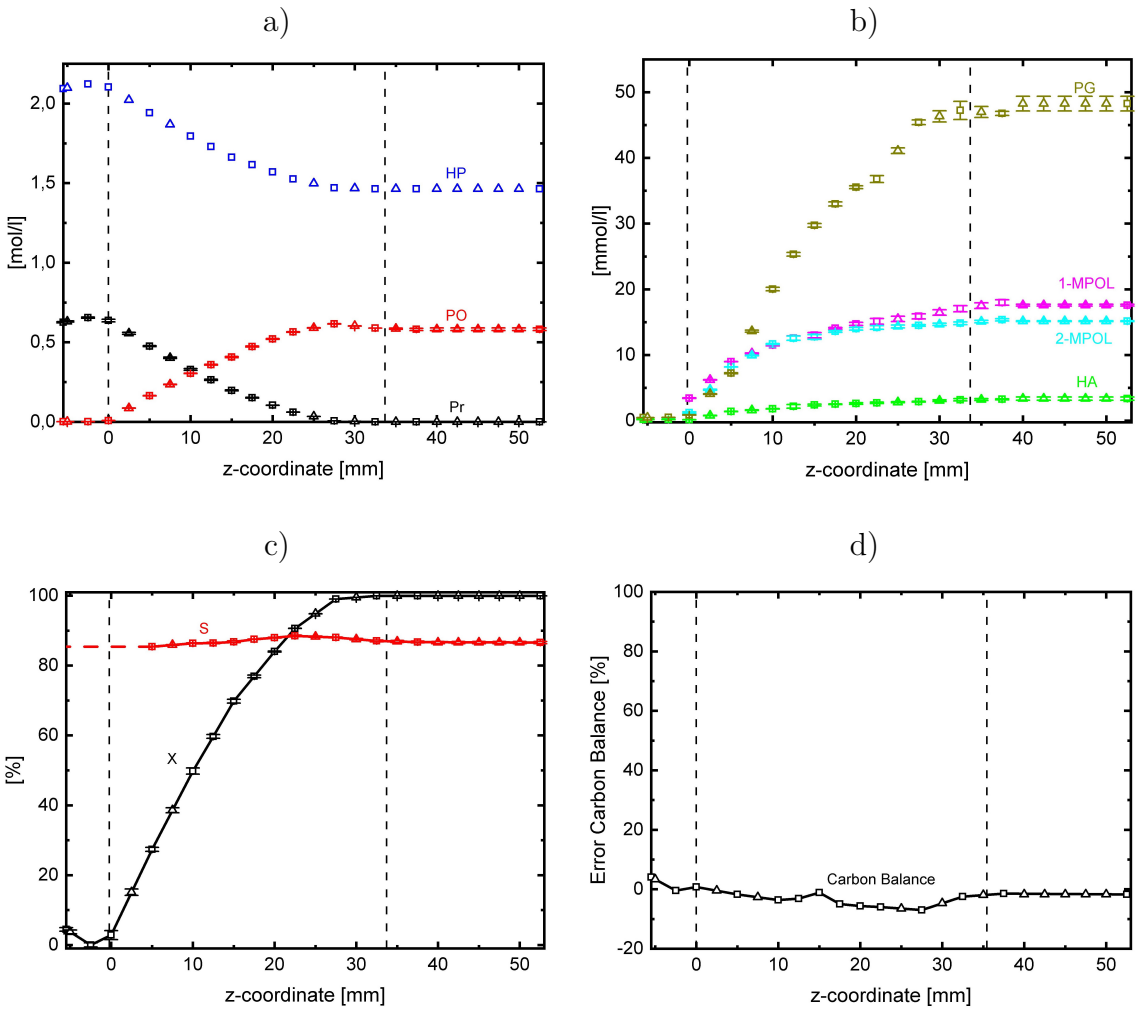

Figure 5.19: Experimental data CPR-1: a) Main epoxidation reaction concentration profile, b) Side reactions concentration profiles, c) PO selectivity (S) and Pr conversion (X), d) Carbon balance closure as a function of coordinate (z). Measured at 40°C and 20 bar pressure. Note: Triangle data point: interpolated data, square data point: measured data.

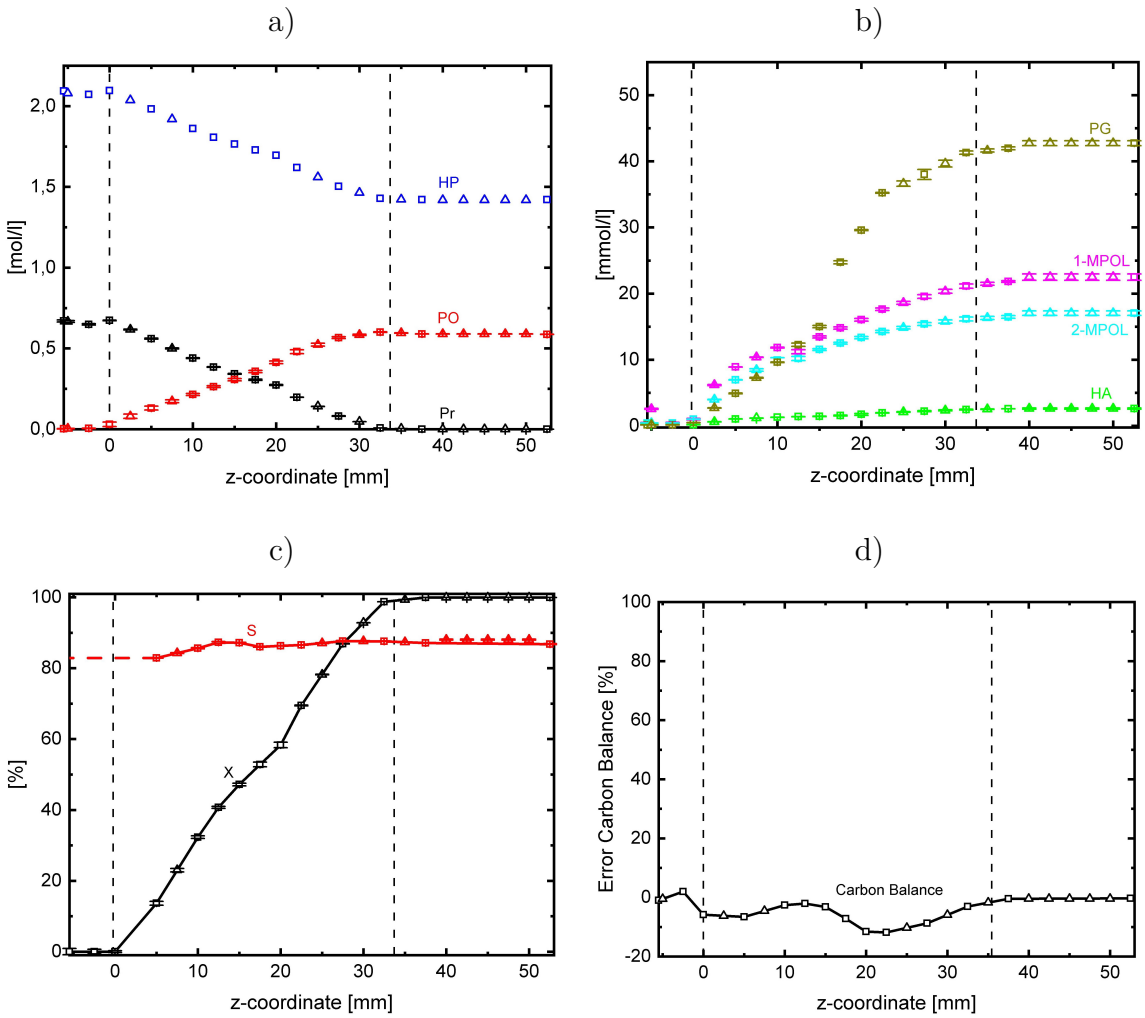

Figure 5.20: Experimental data CPR-2: a) Main epoxidation reaction concentration profile, b) Side reactions concentration profiles, c) PO selectivity (S) and Pr conversion (X), d) Carbon balance closure as a function of coordinate (z). Measured at 40°C and 20 bar pressure. Note: Triangle data point: interpolated data, square data point: measured data.

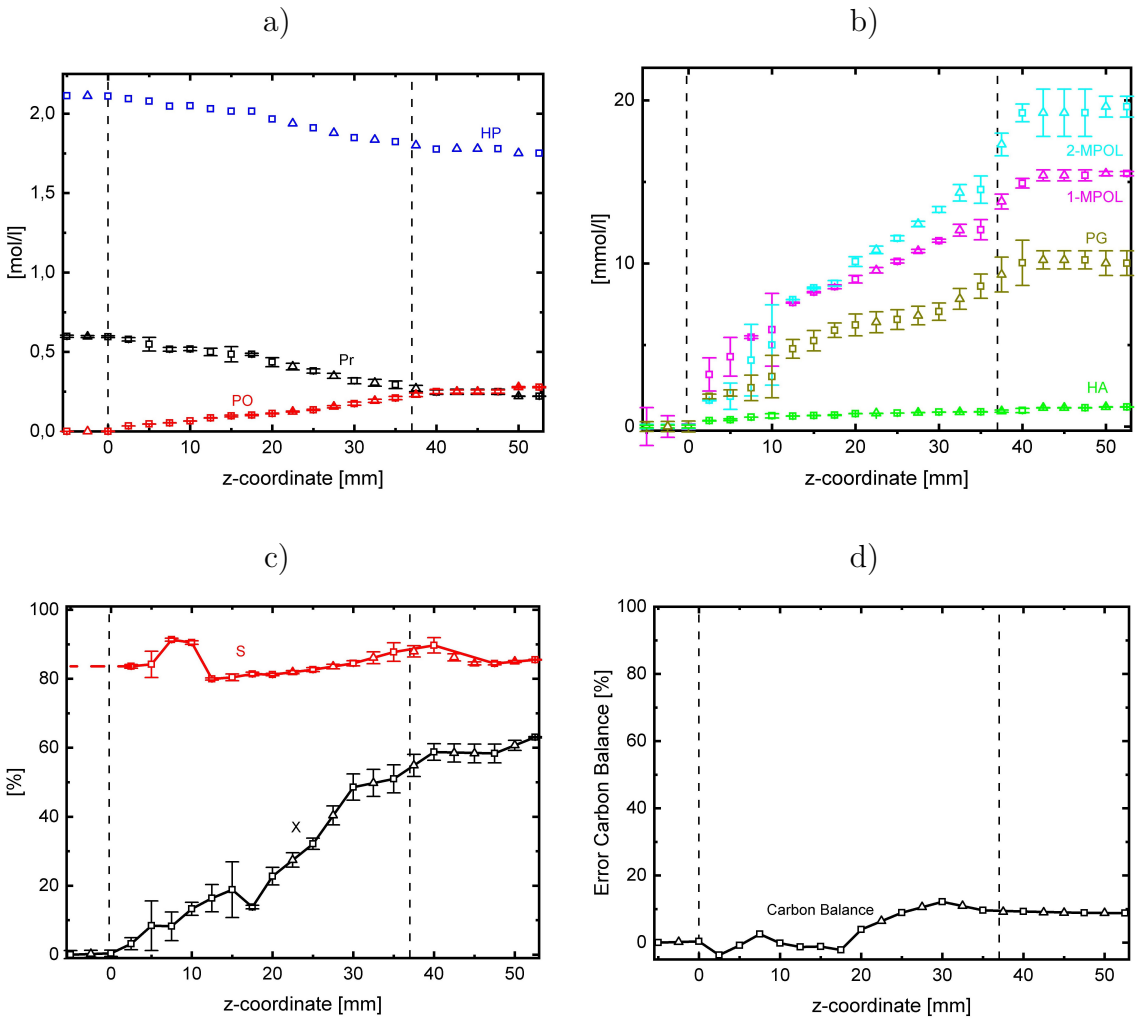

Figure 5.21: Experimental data CPR-3: a) Main epoxidation reaction concentration profile, b) Side reactions concentration profiles, c) PO selectivity (S) and Pr conversion (X) , d) Carbon balance closure as a function of coordinate **(z)**. Measured at 40°C and 20 bar pressure. Note: Triangle data point: interpolated data, square data point: measured data.

5.9 Validation of kinetic models from literature

As shown in Table 3.1 only a limited number of publication regarding the kinetics of the Pr epoxidation with HP over TS-1 catalyst are available in the scientific literature. From this limited number of publication only two of them developed rate law equations not only for the main epoxidation reaction but for the side reactions

as well [83], [84]. In all cases the studies performed the reaction at conditions far from the ones used in industrial scale applications. In the industry, both BASF/DOW and Evonik/Thyssenkrupp perform the epoxidation reaction in fixed bed reactors with extruded TS-1 catalyst at pressures higher than 15 bar with Pr in liquid phase [13], [15] which rises the question if these studies are representative of a industrial scale (HP-PO) reactor. To asses this question, the two fore mentioned studies were used to simulate and fit the experimental measurement CPR-1. Then, the results are used to compare qualitatively the models correlation with the experimental concentration profiles. The parameters of both models can be found in the Appendix section Table 7.3 and Table 7.4, respectively.
The calculation of the Bodenstein criterion to determine if axial dispersion should be included in the reactor model can be found in the Appendix Section 7.1. In Figure 5.22 a) the concentration profile of the main epoxidation reaction simulated with the model from Di Serio [83] is shown. It can be observed that the model is not able to capture the pseudo-zeroth-order behavior of the concentration profile of the main reaction, but is able to predict the final values of HP, Pr and PO at the outlet of the catalytic bed. In the case of the side products in Figure 5.22 b) it is possible to see that the model is able to follow the shape of the concentration curves of PG and MPOL and their final concentrations. The predicted amount of di-methoxypropanol and oligomers are negligible, which also matches our experimental data as these chemicals species are detectable via GC-MS screening, but in trace amount. In the case of the kinetic model from Sulimov [84], it can be observed in Figure 5.23 a) that the model is able to partially follow the overall trend of the main epoxidation reaction but both simulated final concentrations of Pr and PO underestimate the final values of the measured concentration profiles. In the case of the side product formation there is a mismatch between the simulated profiles and the experimental data in terms of overall trend and final concentration, as can be seen in Figure 5.23 b). By comparing both fitted main epoxidation reaction profiles, Figure 5.22 a) and Figure 5.23 a) respectively, there is an evident qualitative difference between both models. While Di Serio model predicts a steep gradient in the first 10 [mm] of the bed, reaching total conversion of Pr, the model of Sulimov predicts a less steep gradients similar to the ones measured experimentally. Nonetheless, both models are not able to predict the pseudo-zeroth-order

behavior. This might be explain by the fact that both models assume that the surface reaction of Pr with $Ti \bullet OOH$ active specie is the rate determining step. Several DFT studies have shown that the rate determining step of the reaction sequence is the adsorption and dissociation of HP to form an $Ti \bullet OOH$ active specie [107], [105], [106], [104]. For the same reaction conditions the model of Di Serio predicts an initial epoxidation reaction rate of about 10 $[mol\ m^{-3}\ s^{-1}]$ whereas the model of Sulimov initial reaction rate is about 2.2 $[mol\ m^{-3}\ s^{-1}]$. The experimentally measured reaction rate for the main epoxidation reaction is approximately 1.02 $[mol\ m^{-3}\ s^{-1}]$.

Regarding the side products formation, the model of Di Serio can predict better the experimental profiles than the model of Sulimov, as can be seen in Figure 5.22 b) and Figure 5.23 b) respectively. The two models proposed different mechanism for the side products formation. Di Serio proposed that side reactions on the Ti closed sites are promoted by the reaction of surface species formed by the adsorption of PO on $Ti \bullet OOH$ species or $Ti \bullet OOH \bullet C_3H_6O$, but in the case of Sulimov, side reactions are promoted by surface species formed by the adsorption of PO on $Ti \bullet CH_3OH$ species or $Ti \bullet CH_3OH \bullet C_3H_6O$. This can be observed in the derived rate laws equations for the side products of both models shown in Table 3.2. While the side products rate laws from the Di Serio model are dependent on the adsorption and local concentration of HP, the side products rate laws from Sulimov are independent of these parameters.

Both models predict the formation of a hot spot inside of the catalytic bed. While the model of Di Serio predicts a maximal temperature of about 60°C, Sulimov maximal temperature in the catalytic bed reaches about 50°C. An interesting observation is that in both cases the temperature starts to increase before the start of the catalytic bed, which is indicated by the vertical dashed lines. This can be attributed to contribution of the axial dispersion in the temperature profile. In both cases the simulated selectivity does not reach 100% for coordinates before the catalytic bed. For the numerical simulation the initial concentration of products of reaction were set to a very small value, but nonetheless distinct from zero, to avoid problems while solving the system of differential equations. This numerical artifice leads to a lower simulated selectivity near the entrance of the catalyst bed. In our experiments, the decomposition of HP was found to be negligible. The

measured concentration of HP at the outlet of the reactor matched the calculated concentration of HP by stoichiometry using the experimentally measured concentration of Pr and HA. In other words, the concentration changes of HP as a function of the reactor coordinate are due manly to the main epoxidation reaction and the formation of HA. Neither of the two models derived a rate law for the formation of HA.

The decomposition of HP by each model can be estimated indirectly with the oxygen simulated concentration profile. In the case of the model of Di Serio, the formation of oxygen follows the measured profile of HA, as can be seen in Figure 5.22 b) . This is due to the fact that the Levenberg-Marquardt algorithm tries to minimize the error between the HP experimental concentration and the model. The model does not include other sources that consume HP apart from the main epoxidation reaction and the decomposition of HP. Once the main reaction has reached its final value determined by the profiles of Pr and PO the algorithm further minimizes the difference of experimental and simulated HP profiles by increasing the rate of decomposition of HP in such a manner that the final value matches with the experimental data. In the case of the Sulimov model a similar behavior can be observed. In the Figure 5.23 a) both Pr and PO final concentrations are underestimated by the model, but in the case of HP the final value predicted by the model matches the experimental value. In Figure 5.23 b) it can be seen that in this case the amount of oxygen formed is higher than the predicted amount of oxygen by the model of Di Serio. This is because the algorithm has to compensate not only the consumption of HP by formation of HA, but also the underestimation of the main epoxidation reaction. Therefore, in both models the oxygen concentration profiles are a consequence of the algorithm trying to minimize the difference between the model and the experimental HP concentration profile and attributing said difference to the only source of consumption of HP beside the main epoxidation reaction, which is the decomposition reaction. The determination and quantification of HA and MA is important from the safety point of view. These species consume HP, and therefore not quantifying their concentration can lead to an erroneous estimation of the extent of decomposition of HP. An accurate estimation of the decomposition of HP under reaction conditions is important for industrial applications due to the fact that oxygen can form explo-

sive mixtures with Pr.

For the simulated profiles the model of Sulimov has better qualitative agreement with the experimentally measured concentration profiles of the main epoxidation reaction. This model was used to simulate the whole range of residence times investigated in this study. The results are shown in Figure 5.24 and Figure 5.25.

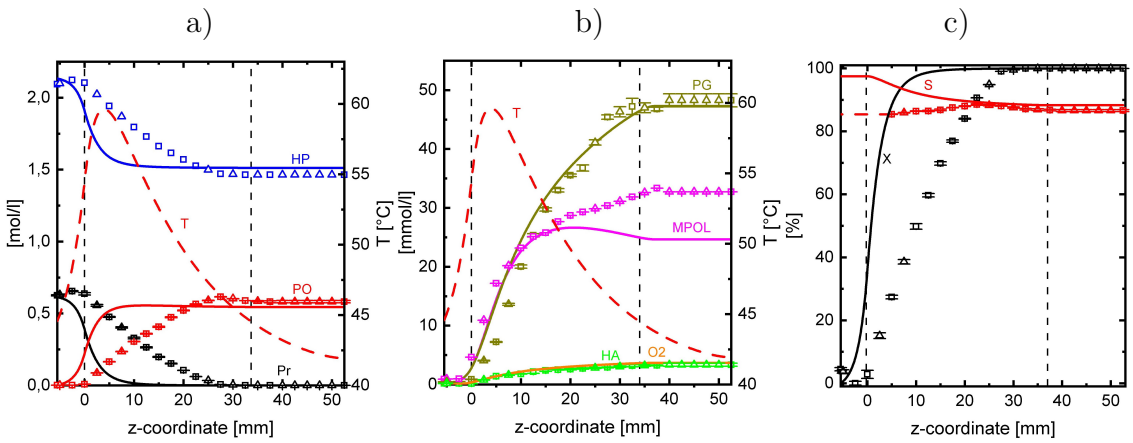

Figure 5.22: Simulated concentration, temperature, Pr conversion (X) and PO selectivity (S) profiles for data set CPR-1 by Di Serio [83]. Note: Numerical simulation (solid lines). Experimental data (squares with error bars).

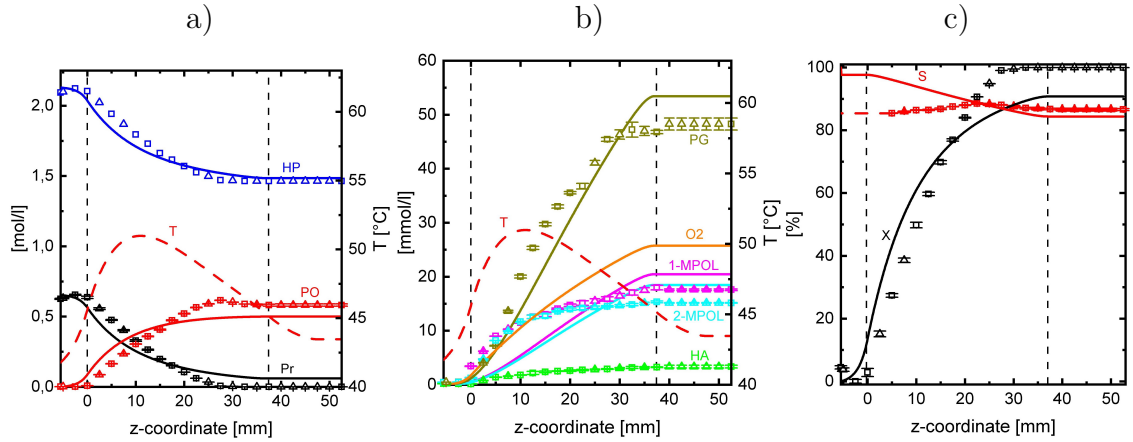

Figure 5.23: Simulated concentration, temperature, Pr conversion (X) and PO selectivity (S) profiles for data set CPR-1 by Sulimov [84]. Note: Numerical simulation (solid lines). Experimental data (squares with error bars).

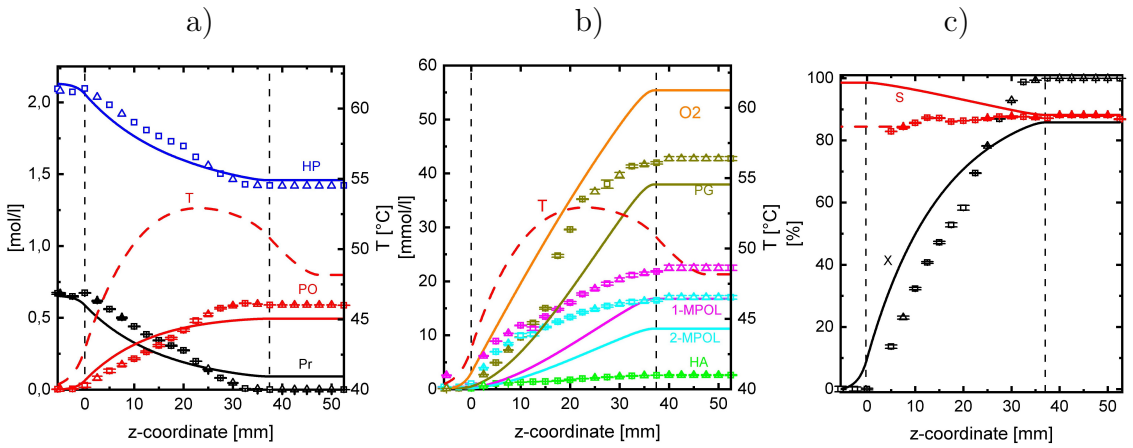

Figure 5.24: Simulated concentration, temperature, Pr conversion (X) and PO selectivity (S) profiles for data set CPR-2 by Sulimov [84]. Note: Numerical simulation (solid lines). Experimental data (squares with error bars).

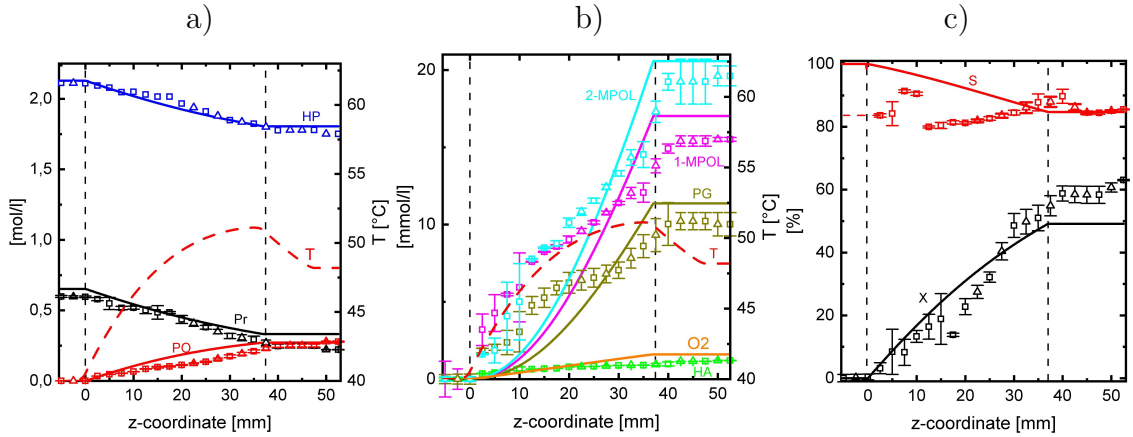

Figure 5.25: Simulated concentration, temperature, Pr conversion (X) and PO selectivity (S) profiles for data set CPR-3 by Sulimov [84]. Note: Numerical simulation (solid lines). Experimental data (squares with error bars).

5.10 Development of kinetic model

The measured spatially resolved profiles shown in Figure 5.19, Figure 5.20 and Figure 5.21 exhibit a pseudo-zeroth-order behavior. Previous models have been

developed based on the assumption that the rate determining step in the epoxidation reaction sequence is the reaction of Pr with the $Ti \bullet OOH$ active specie in the surface of the catalyst. Several DFT simulations have shown that the rate determining step in the epoxidation of Pr with HP is the dissociative adsorption of HP on a $Ti(SiO)_3OH$ site forming an $Ti(SiO)_3OOH \bullet H_2O$ active specie and a molecule of water that remains coordinated to the Ti atom [107], [105], [106], [104]. Additionally, Clerici et.al [80] observed experimentally that the epoxidation reaction approximates a pseudo-zeroth-order behavior for high HP concentrations. The maximal amount of Ti atoms that can be inserted into the catalyst framework is limited to about 3%wt TiO_2 [63], from which not all Ti sites are accessible by the molecules of HP and Pr. In this sense, the amount of molecules of reagents far exceed the number of accessible Ti sites. Under these conditions, if the rate determining step is the dissociative adsorption of HP to form an $Ti \bullet OOH \bullet H_2O$ active site, the rate will limited by the maximal speed at which $Ti(SiO)_3 \bullet OH$ site(s) can adsorb and dissociate HP molecules leading to the measured pseudo-zeroth-order behavior. Based on the experimental data and the aforementioned observations, an additional model is proposed. The main assumptions are:

1. *Bordiga et.al [177] pointed out that water molecules are responsible for the hydrolysis of one Si-O-Ti bridge in the perfect tetrahedral Ti(SiO)4 units. Additionally, both experiments [97], [98], [178] and QM/MM studies [64], [102] have shown that when TS-1 is exposed to water one Ti-O-Si bridge will be hydrolyzed and defective Ti moieties will dominate in hydrous conditions. Therefore when water is present in the reaction mixture, the dominant Ti surface species are hydrated Ti defective sites or* $Ti(SiO)_3OH$.

2. *MeOH is the media, therefore there are no* $Ti(SiO)_3OH$ *free sites, all sites can be assumed to have MeOH coordinated on them. Sites with MeOH adsorbed on them are denoted as* $Ti^*(SiO)_3OH$. *Then,* $Ti(SiO)_3OH \approx 0$.

3. *The rate determining step is the adsorption/dissociation of HP on* $Ti^*(SiO)_3OH$ *units forming a* $Ti^*(SiO)_3OOH \bullet H_2O$ *active species and a molecule of water that remains coordinated to the Ti atom [107], [105], [106], [104]. This step is considered to be an irreversible chemisorption.*

4. *Pr is weakly adsorbed on the* $Ti^*(SiO)_3OOH \bullet H_2O$ *site and reacts very fast. Xiong et al. [101] did not detect the Raman spectra of adsorbed Pr when the catalyst sample was previously treated with HP. In contrast, the spectra of physisorbed Pr was recorded successfully on untreated TS-1 samples. This may indicate that the life time of the reaction intermediate* $Ti(SiO)_3OOH \bullet C_3H_6 \bullet H_2O$ *is short and cannot be detected by Raman spectroscopy. Therefore, the formation of this intermediate can be considered kinetically irrelevant and the reaction can be assumed to follow an Eley-Rideal mechanism, then* $Ti^*(SiO_3)OOH \bullet C_3H_6 \bullet H_2O \approx 0$. *Moreover, if the catalyst is previously treated with HP solutions, then* $Ti^*(SiO)_3OH \bullet C_3H_6 \approx 0$.

5. *If Pr reacts weakly adsorbed, then PO will be also weakly adsorbed and desorbs easily. Thus,* $Ti^*(SiO)_3OH \bullet C_3H_6O \bullet H_2O \approx 0$.

6. *The experimentally measured slope of the pseudo-zeroth-order epoxidation reaction remains constant independently of the local concentration of PO as can be observed in Figure 5.19 a), Figure 5.20 a) and Figure 5.21 a). This observation may indicate that under the conditions in which the experiments were performed, the competitive adsorption of PO does not play a significant role in the epoxidation rate. Therefore, the competitive adsorption of PO can be neglected and* $Ti^*(SiO)_3OH \bullet C_3H_6O \approx 0$.

7. *The co-solvent water does not inhibit the catalytic activity of the TS-1 catalyst and plays a fundamental role on the hydration of the tetrahedral* $Ti(SiO)_4$ *units forming* $Ti(SiO)_3OH$ *species [98], [99], [100]. Therefore,* $Ti^*(SiO)_3OH \bullet H_2O \approx 0$.

Based on these assumptions the mechanism shown on Table 5.7 is proposed. From this proposed reaction mechanism it is possible to derive a rate law equation for each reaction involved. The balance of surface species expressed as surface coverages is:

$$1 = \theta_{Ti(SiO)_3OH} + \theta_{Ti^*(SiO)_3OH} + \theta_{Ti^*(SiO)_3OOH\bullet H_2O} + \theta_{Ti^*(SiO)_3OOH\bullet C_3H_6\bullet H_2O}$$
$$+\theta_{Ti^*(SiO)_3OH\bullet C_3H_6O\bullet H_2O} + \theta_{Ti^*(SiO)_3OH\bullet C_3H_6} + \theta_{Ti^*(SiO)_3OH\bullet H_2O} + \theta_{Ti^*(SiO)_3OH\bullet C_3H_6O}$$

The balance can be simplified by assuming that there are no $Ti(SiO)_3OH$ free sites and all sites have MeOH coordinated on them, therefore $Ti(SiO)_3OH \approx 0$.

Table 5.7: Proposed reaction mechanism

1.	$Ti(SiO)_3OH + CH_3OH \overset{K_1}{\rightleftharpoons} Ti^*(SiO)_3OH$
2.	$Ti^*(SiO)_3OH + H_2O_2 \xrightarrow{k_2} Ti^*(SiO)_3OOH \bullet H_2O$
3.	$Ti^*(SiO)_3OOH \bullet H_2O + C_3H_6 \xrightarrow{k_3} Ti^*(SiO)_3OH \bullet C_3H_6O \bullet H_2O$
4.	$Ti^*(SiO)_3OH \bullet C_3H_6O \bullet H_2O + H_2O \xrightarrow{k_4} Ti^*(SiO)_3OH + C_3H_8O_2 + H_2O$
5.	$Ti^*(SiO)_3OH \bullet C_3H_6O \bullet H_2O + CH_3OH \xrightarrow{k_5} Ti^*(SiO)_3OH + 1 - C_4H_{10}O_2 + H_2O$
6.	$Ti^*(SiO)_3OH \bullet C_3H_6O \bullet H_2O + CH_3OH \xrightarrow{k_6} Ti^*(SiO)_3OH + 2 - C_4H_{10}O_2 + H_2O$
7.	$Ti^*(SiO)_3OH \bullet C_3H_6O \bullet H_2O \xrightarrow{K_7'^-} Ti^*(SiO)_3OH + C_3H_6O + H_2O$
8.	$Ti^*(SiO)_3OOH \bullet H_2O \xrightarrow{k_8} Ti^*(SiO)_3OH + H_2O + \frac{1}{2}O_2$
9.	$Ti^*(SiO)_3OH + H_2O \overset{K_9}{\rightleftharpoons} Ti^*(SiO)_3OH \bullet H_2O$
10.	$Ti^*(SiO)_3OH + C_3H_6 \overset{K_{10}}{\rightleftharpoons} Ti^*(SiO)_3OH \bullet C_3H_6$
11.	$Ti^*(SiO)_3OH + C_3H_6O \overset{K_{11}}{\rightleftharpoons} Ti^*(SiO)_3OH \bullet C_3H_6O$

Additionally, Pr is weakly adsorbed on the active site and reacts very fast, thus the formation of the surface specie $Ti^*(SiO)_3OOH \bullet C_3H_6 \bullet H_2O$ is kinetically irrelevant and an Eley-Rideal mechanism can be assumed, therefore $Ti^*(SiO)_3OOH \bullet C_3H_6 \bullet H_2O \approx 0$. The catalyst is previously treated with HP before the introduction of Pr into the reaction mixture, thus $Ti^*(SiO)_3OH \bullet C_3H_6 \approx 0$. If Pr reacts weakly adsorbed, then PO will be also weakly adsorbed and desorbs easily, thus $Ti^*(SiO)_3OH \bullet C_3H_6O \bullet H_2O \approx 0$. The slope of the epoxidation pseudo-zeroth-order reaction is independent of the local PO concentration, this may suggest that the competitive adsorption of PO has a negligible effect on the epoxidation rate, therefore $Ti^*(SiO)_3OH \bullet C_3H_6O \approx 0$. Lastly, the co-solvent water does not inhibit the catalytic activity of the TS-1 catalyst and participates on the formation of $Ti(SiO)_3OH$ hydrated species. Therefore, $Ti^*(SiO)_3OH \bullet H_2O \approx 0$. With these

assumptions the balance of surface species can be reduced to:

$$1 = \theta_{Ti^*(SiO)_3OH} + \theta_{Ti^*(SiO)_3OOH\bullet H_2O}$$
$$\theta_{Ti^*(SiO)_3OOH\bullet H_2O} = 1 - \theta_{Ti^*(SiO)_3OH}$$
$$\theta_{Ti^*(SiO)_3OH} = 1 - \theta_{Ti^*(SiO)_3OOH\bullet H_2O}$$

The reactor is operated under steady state conditions, therefore the surface coverage of chemical species at a certain position in the catalyst bed is independent of time. Then, the system of differential equations can be transformed into a algebraic system which can be solved analytically as follows:

$$\frac{d\theta_{Ti^*(SiO)_3OOH\bullet H_2O}}{dt} \approx 0$$
$$k_2\theta_{Ti^*(SiO)_3OH}[H_2O_2] - k_3\theta_{Ti^*(SiO)_3OOH\bullet H_2O}[C_3H_6] \approx 0$$
$$k_2\theta_{Ti^*(SiO)_3OH}[H_2O_2] - k_3[C_3H_6]\left(1 - \theta_{Ti^*(SiO)_3OH}\right) \approx 0$$
$$k_2\theta_{Ti^*(SiO)_3OH}[H_2O_2] - k_3[C_3H_6] + k_3\theta_{Ti^*(SiO)_3OH}[C_3H_6] \approx 0$$
$$k_3[C_3H_6] = k_2\theta_{Ti^*(SiO)_3OH}[H_2O_2] + k_3\theta_{Ti^*(SiO)_3OH}[C_3H_6]$$
$$k_3[C_3H_6] = \theta_{Ti^*(SiO)_3OH}\left(k_2[H_2O_2] + k_3[C_3H_6]\right)$$
$$\theta_{Ti^*(SiO)_3OH} = \frac{k_3[C_3H_6]}{(k_2[H_2O_2] + k_3[C_3H_6])}$$
$$\theta_{Ti^*(SiO)_3OOH\bullet H_2O} = \frac{k_2[H_2O_2]}{(k_2[H_2O_2] + k_3[C_3H_6])}$$

$$\frac{d\theta_{Ti^*(SiO)_3OH\bullet C_3H_6O\bullet H_2O}}{dt} \approx 0$$
$$k_3\theta_{Ti^*(SiO)_3OOH\bullet H_2O}[C_3H_6] - K_7'^{-}\theta_{Ti^*(SiO)_3OH\bullet C_3H_6O\bullet H_2O} - k_4\theta_{Ti^*(SiO)_3OH\bullet C_3H_6O\bullet H_2O}[H_2O]$$
$$- k_5\theta_{Ti^*(SiO)_3OH\bullet C_3H_6O\bullet H_2O}[CH_3OH] - k_6\theta_{Ti^*(SiO)_3OH\bullet C_3H_6O\bullet H_2O}[CH_3OH] \approx 0$$
$$k_3\theta_{Ti^*(SiO)_3OOH\bullet H_2O}[C_3H_6] =$$
$$\theta_{Ti^*(SiO)_3OH\bullet C_3H_6O\bullet H_2O}(K_7'^{-} + k_4[H_2O] + k_5[CH_3OH] + k_6[CH_3OH])$$

Since MeOH and water are the solvent and co-solvent their concentration is high and can be regarded as a constant values. Then, these concentrations can be

incorporated into the side reactions rate constants.

$$k_3\theta_{Ti^*(SiO)_3OOH\bullet H_2O}[C_3H_6] = \theta_{Ti^*(SiO)_3OH\bullet C_3H_6O\bullet H_2O}(K_7'^{-} + k_4' + k_5' + k_6')$$
$$k_3\theta_{Ti^*(SiO)_3OOH\bullet H_2O}[C_3H_6] = \theta_{Ti^*(SiO)_3OH\bullet C_3H_6O\bullet H_2O}\, K_7^{-1}$$
$$\theta_{Ti^*(SiO)_3OH\bullet C_3H_6O\bullet H_2O} = \frac{K_7 k_2 k_3[H_2O_2][C_3H_6]}{(k_2[H_2O_2] + k_3[C_3H_6])}$$

Where $K_7 = 1/(K_7'^{-} + k_4' + k_5' + k_6')$. Then, by assuming that the rate determining step for the main epoxidation reaction is the adsorption/dissociation of HP on $Ti^*(SiO)_3OH$ species, while for the ring opening reaction it is the surface reaction, each rate can be written as follows:

$$r_2 = k_2\theta_{Ti^*(SiO)_3OH}[H_2O_2] \rightarrow r_2 = \frac{k_2 k_3[H_2O_2][C_3H_6]}{(k_2[H_2O_2] + k_3[C_3H_6])}$$
$$r_4 = k_4\theta_{Ti^*(SiO)_3OH\bullet C_3H_6O\bullet H_2O}[H_2O] \rightarrow r_4 = \frac{K_7 k_4 k_2 k_3[H_2O_2][C_3H_6][H_2O]}{(k_2[H_2O_2] + k_3[C_3H_6])}$$
$$r_5 = k_5\theta_{Ti^*(SiO)_3OH\bullet C_3H_6O\bullet H_2O}[CH_3OH] \rightarrow r_5 = \frac{K_7 k_5 k_2 k_3[H_2O_2][C_3H_6][CH_3OH]}{(k_2[H_2O_2] + k_3[C_3H_6])}$$
$$r_6 = k_6\theta_{Ti^*(SiO)_3OH\bullet C_3H_6O\bullet H_2O}[CH_3OH] \rightarrow r_6 = \frac{K_7 k_6 k_2 k_3[H_2O_2][C_3H_6][CH_3OH]}{(k_2[H_2O_2] + k_3[C_3H_6])}$$
$$r_8 = k_8\theta_{Ti^*(SiO)_3OOH\bullet H_2O} \rightarrow r_8 = \frac{k_8 k_2[H_2O_2]}{(k_2[H_2O_2] + k_3[C_3H_6])}$$

The derived rate law equation for the main epoxidation reaction (r_2) can be linearized as follows:

$$\frac{[C_3H_6]}{r_2} = \frac{1}{k_2}\frac{[C_3H_6]}{[H_2O_2]} + \frac{1}{k_3}$$

Additionally, the side reactions (r_4), (r_5) and (r_6) can be linearized according to:

$$\frac{[C_3H_6]}{r_n} = \frac{1}{K_7 k_2 k_n'}\frac{[C_3H_6]}{[H_2O_2]} + \frac{1}{K_7 k_3 k_n'}$$

Where (k_n') can be equal to ($k_4' = k_4\,[H_2O]$), ($k_5' = k_5\,[CH_3OH]$) or ($k_6' = k_6\,[CH_3OH]$) depending on the side reaction rate being linearized. The rate of

decomposition of HP (r_8) can be also linearized as follows:

$$\frac{1}{r_8} = \frac{k_3}{k_8 k_2}\frac{[C_3H_6]}{[H_2O_2]} + \frac{1}{k_8 k_2}$$

If in fact, the derived equation is able to describe the experimental data for the main epoxidation reaction, a plot of the measured $[C_3H_6]/r_2$ as a function of $[C_3H_6]/[H_2O_2]$ should give a straight line with a slope equal to the inverse of the adsorption/dissociation constant of HP ($1/k_2$) and intersection with the y-axis equal to the reciprocal of the rate constant of the reaction of Pr with the $Ti^*(SiO)_3OH \bullet OOH \bullet H_2O$ active specie ($1/k_3$). For the calculation of the experimental differential rates the data was smoothed with the Savitzky-Golay method with a polynomial order of two.

As can be observed in Figure 5.26 a) and b) the plots of the experimental data of the linearized main epoxidation reaction ($[C_3H_6]/r_2 = f([C_3H_6]/[H_2O_2])$) follows a straight line with a $R^2 = 0.99$ and $R^2 = 0.98$, respectively. The small deviation from linear behavior of the experimental differential rate can be explain by the fact that the parameters (k_2) and (k_3) are not truly constant values, as adsorption and reaction constants depend also on the local temperature. In the plotted range of $[Pr]/[HP]$ from 0.3-0 temperature is most likely increasing due to the exothermic epoxidation reaction, thus causing variation in the fore mentioned parameters.

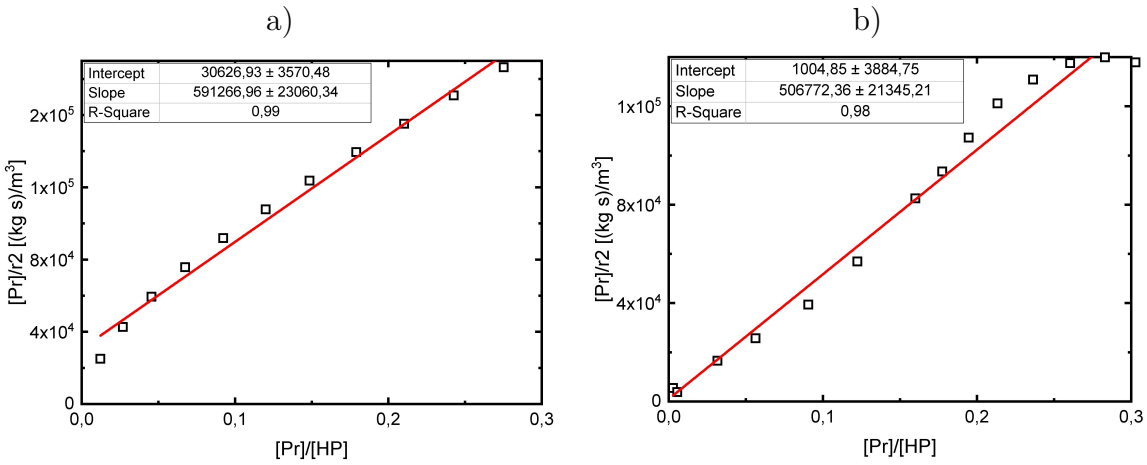

Figure 5.26: Experimental $[C_3H_6]/r_2$ as a function of $[C_3H_6]/[H_2O_2]$ a) CPR-1, b) CPR-2

A stronger deviation from linearity is observed in the case of the side reactions (r_4), (r_5) and (r_6) when plotted according to their linearized form as shown Figure 5.27 for the measurement CPR-1. It has been reported that the rate of side production formation strongly depends on the reactor temperature, in this sense the deviation can be attributed to the strong dependence of the parameters (K_7), (k'_4), (k'_5) and (k'_6) with the local temperature. Due to this, the linearization of the side reactions yields broad error ranges or inconsistent physical units (negative values). Nonetheless, the rates (r_4) and (r_5) exhibit a higher degree of linearity $(R^2 = 0.84, R^2 = 0.71)$ than (r_6) $(R^2 = 0.19)$. This may suggest that the parameter (k'_6) related to the formation of 2-MPOL depends much stronger on the local temperature than (k'_4) and (k'_5).

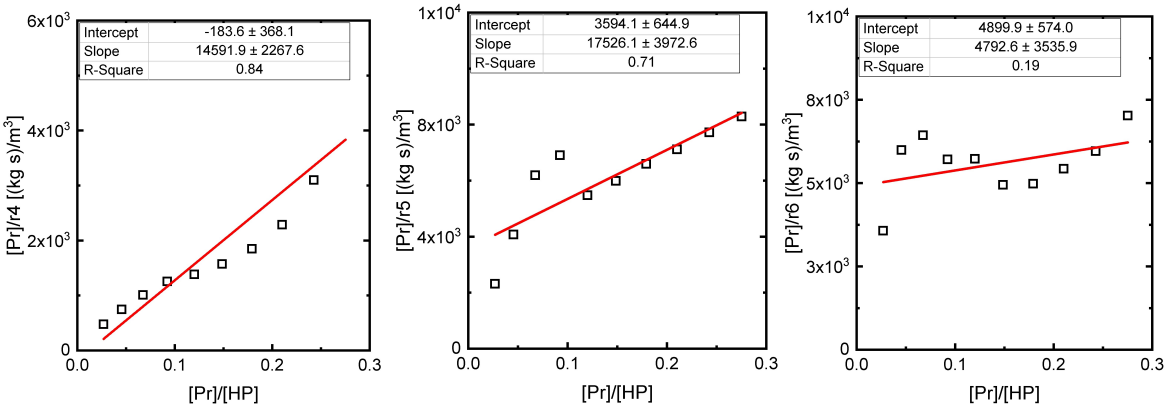

Figure 5.27: Experimental $[C_3H_6]/r_n$ as a function of $[C_3H_6]/[H_2O_2]$ for (r_4), (r_5) and (r_6)

In the case of the HP decomposition rate (r_8), no significant extent of decomposition of HP has been measured in the experiments performed in this work, therefore the pre-exponential factor and the activation energy for (k_8) were adopted directly from the model of Sulimov.

From the linearized rate laws it is possible to derive the dimensional units of the model parameters with $k_2 - k_6[m^3\, kg^{-1}\, s^{-1}]$, $K_7[kg\, s\, mol^{-1}]$ and $k_8[mol\, kg^{-1}\, s^{-1}]$. The values obtained from the linear fit of the experimental differential reaction rate (r_2) and the parameters obtained by Sulimov et al. [84] for (k_4), (k_5), (k_6) and (k_8) were used as initial guess for a minimization of the sum of squares of differences

between the experimental data and the values predicted by the model. As can be observed in Figure 5.28 a), d) and g) the derived Eley-Rideal model shows a linear trend in agreement with the experimentally measured pseudo-zeroth-order behavior of the main epoxidation reaction. In the case of the ring opening reactions in Figure 5.28 b), e) and h) the model is able to estimate the final value and shape of the profiles for high concentration of side products. Nonetheless, for low concentration of side products at the beginning of the catalyst bed, the model is not able to fully capture the non-linear trend. These non-linear trends can be attributed to pronounced temperature variations within the first 10-15 mm of the reactor. As discussed in Section 5.8, temperature profiles could not be measured due to the conduction of heat through the stainless steel sampling capillary, in this sense the simulated temperature profiles requires experimental validation. Nonetheless, the simulated temperature profile within the catalyst bed shows a sharp increase of the temperature in the first half of the reactor. Temperature dependent parameters such activation energies and adsorption enthalpies were adopted from the model of Sulimov, which may explain the small deviations of the side products concentration for this section of the catalyst bed. In this sense, these parameters should be experimentally determined by acquiring further temperature dependent experimental data.

The pseudo-zeroth-order behavior of the model for high concentration of reagents can be explained by analyzing the derived rate law for the main epoxidation reaction which exhibit two limiting behaviors. When the reaction starts the concentration of Pr is high and the surface reaction is much faster than the adsorption/dissociation of HP ($k_3[C_3H_6] >>> k_2[H_2O_2]$). Under these conditions the rate approximates the rate of adsorption/dissociation of HP.

$$r_2 = \frac{k_2 k_3 [H_2O_2][C_3H_6]}{(k_2[H_2O_2] + k_3[C_3H_6])} \xrightarrow{k_3[C_3H_6] >>> k_2[H_2O_2]}$$
$$r_2 = \frac{k_2[H_2O_2]\cancel{k_3[C_3H_6]}}{\cancel{k_3[C_3H_6]}} \rightarrow \boxed{r_2 = k_2[H_2O_2]}$$

This is consistent with the DFT studies that showed that the rate determining step of the reaction mechanism is the formation an $Ti(SiO)_3 \bullet OOH \bullet H_2O$ intermediate by the HP adsorption and subsequent dissociation. Thus, if the experiment

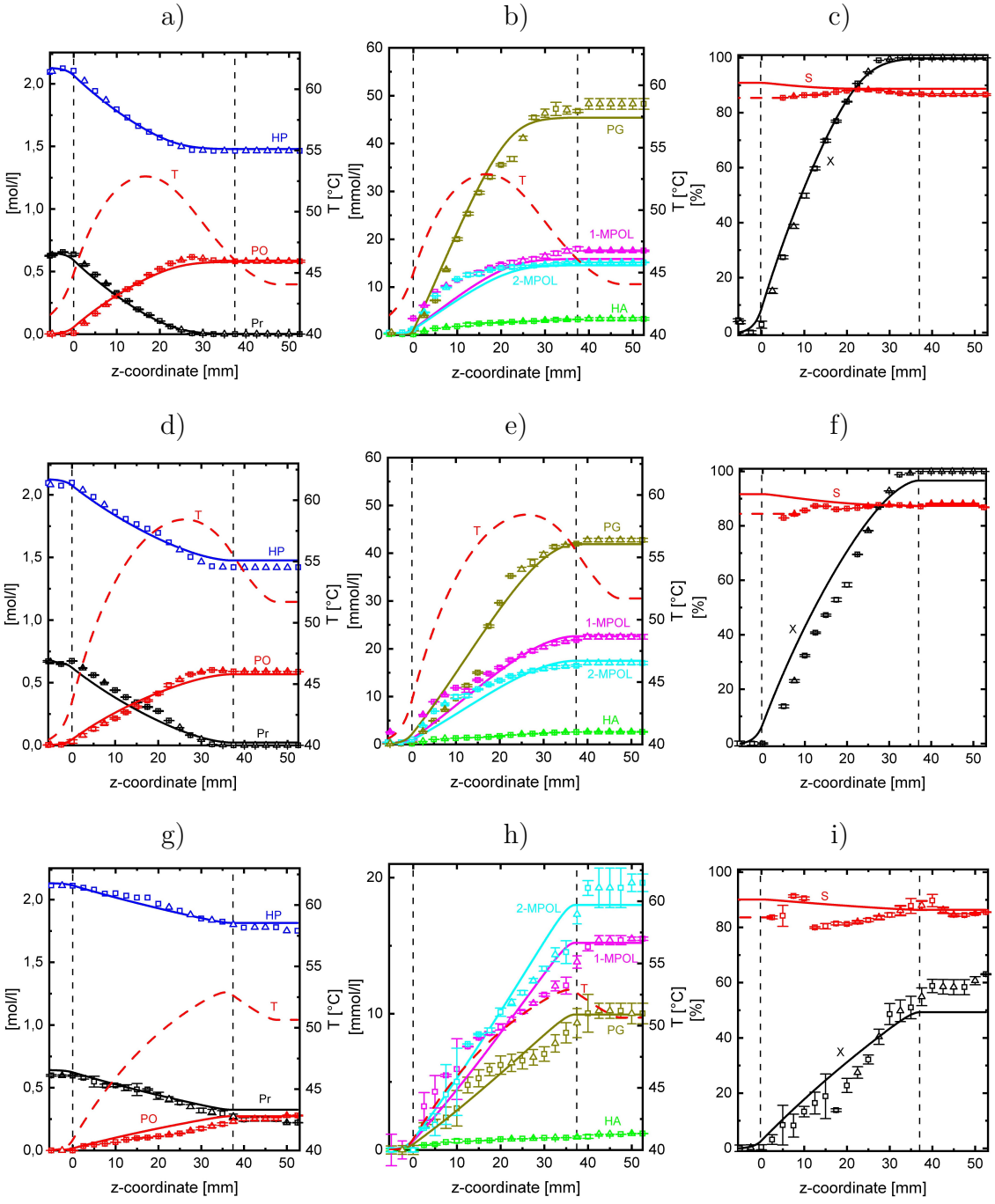

Figure 5.28: Derived Eley-Rideal model and experimental data CPR-1 (top row) a), b), c). CPR-2 (center row) d), e), f). CPR-3 (bottom row) g), h), i). Concentration, temperature, Pr conversion (X) and PO selectivity (S) profiles. Note: Numerical simulation (solid lines), Experimental data (squares with error bars).

is conducted with a concentration of HP and Pr that far exceeds the amount of available $Ti(SiO)_3 \bullet OH$ sites on the surface of the catalyst, the reaction rate will be limited to the maximal speed at which these sites can adsorb and dissociate HP molecules, which can explain the zeroth-order behavior reported by Clerici at high HP concentration [80]. As the reaction progresses, Pr is consumed and the surface reaction becomes slower, then the rate is governed by the surface reaction of Pr with the $Ti^*(SiO)_3OH \bullet OOH \bullet H_2O$ active specie until Pr is fully consumed.

$$r_2 = \frac{k_2 k_3 [H_2O_2][C_3H_6]}{(k_2[H_2O_2] + k_3[C_3H_6])} \xrightarrow{k_3[C_3H_6] <<< k_2[H_2O_2]}$$
$$r_2 = \frac{\cancel{k_2[H_2O_2]} k_3[C_3H_6]}{\cancel{k_2[H_2O_2]}} \rightarrow \boxed{r_2 = k_3[C_3H_6]}$$

Additionally, the selectivity towards PO can be expressed as a quotient of reaction rates as follows:

$$S_z^{PO} = \frac{moles\ PO}{total\ moles\ Pr\ reacted} \rightarrow S_z^{PO} = \frac{r_2 - r_4 - r_5 - r_6}{r_2}$$
$$S_z^{PO} = 1 - K_7 k_4 [H_2O] - K_7 k_5 [CH_3OH] - K_7 k_6 [CH_3OH]$$
$$S_z^{PO} = 1 - K_7 k_4' - K_7 k_5' - K_7 k_6' = 1 - K_7 \left(k_4' + k_5' + k_6'\right) \approx constant$$

In this sense, the selectivity of the reaction at the coordinate (z) depends on the side products rate constants and the (K_7) factor leading to a approximately constant selectivity that fits the experimental data shown in Figure 5.28 c), f) and i). For reactor coordinates near the entrance of the reactor both simulated and experimental selectivities diverge. This deviation is attributed to the complexity of the analyte mixture. Traces amounts of low volatile products remain in the sample loops of the Gas Chromatograph, resulting in a lower selectivity near the start of the catalyst bed. This interaction between the analyte mixture and the analytical device cannot be modeled by the derived E-R model leading to the observed small deviation.

The models in this work were compared quantitatively by calculating the sum of the variance and F_C values between the experimental data and the value predicted by the model for each measured chemical species profile.

Parameter	E-R	Sulimov	Di Serio
$\sum_{i=1}^{n} S_i^2 =$	0.0215	0.1594	1.1077
$\sum_{i=1}^{n} F_{C_i} =$	44.51	194.03	646.15

$\sum_{i=1}^{n} F_{critical}(n-p-n_e+1, n_e-1, 1-\alpha) = 116.1$

Table 5.8: Statistical comparison of models for CPR-1

Table 5.9: Parameters derived Eley-Rideal model

Parameter	Value	Units	Parameter	Value	Units
$k°_2$	$(1,6 \pm 0,05)x10^{-9}$	$\left[\frac{m^3}{(kg*s)}\right]$	$H_2^{\circ *}$	$(18,71 \pm 0,86)x10^3$	$\left[\frac{J}{mol}\right]$
$k°_3$	$(6,64 \pm 1,04)x10^2$	$\left[\frac{m^3}{(kg*s)}\right]$	E_3^*	$(45,03 \pm 3,15)x10^3$	$\left[\frac{J}{mol}\right]$
$k°_4$	$(7,48 \pm 0,608)x10^5$	$\left[\frac{m^3}{(kg*s)}\right]$	E_4^*	$(60,59 \pm 4,54)x10^3$	$\left[\frac{J}{mol}\right]$
$k°_5$	$(3,1 \pm 0,53)x10^5$	$\left[\frac{m^3}{(kg*s)}\right]$	E_4^*	$(63,45 \pm 5,65)x10^3$	$\left[\frac{J}{mol}\right]$
$k°_6$	$(2,3 \pm 0,56)x10^5$	$\left[\frac{m^3}{(kg*s)}\right]$	E_6^*	$(62,97 \pm 5,86)x10^3$	$\left[\frac{J}{mol}\right]$
$K°_7$	$(3,5 \pm 0,34)x10^{-5}$	$\left[\frac{(kg*s)}{mol}\right]$	$H_7^{\circ *}$	$(20,48 \pm 1,07)x10^3$	$\left[\frac{J}{mol}\right]$
$k°_8$	$(4,3 \pm 0,4)x10^1$	$\left[\frac{m^3}{(kg*s)}\right]$	E_8^*	$(49,81 \pm 3,44)x10^3$	$\left[\frac{J}{mol}\right]$

* Adopted from Sulimov [84]

The results of the statistical analysis of the different kinetic models in this work shown in Table 5.8 shows that the derived Eley-Rideal model has the lowest deviation with the experimental data. Moreover, the F-test at a significance level of 0.05 showed that the derived model describes adequately the experimental data. The parameters of the derived E-R model and their values are shown on Table 5.9.

Table 5.10: List of parameters of experiments HPPO-1 and POC-1

Experiment	T,P [°C, bar]	[Pr]	[HP]	LHSV [h^{-1}]	m_{cat} [g], (L mm)	m_{MFC-1} [g/h]	m_{MFC-2} [g/h]	m_{MFC-3} [g/h]	Feed wt%	SS [h]
HPPO-1	40, 30	0.6	2.0	2.0	16.5 (200)	2.6	84	-	73/24/3	≈24
POC-1	40, 30	0.6	2.0	2.0	9.4 (200)[1]	2.6	84	-	73/24/3	≈24

Feed composition in (MeOH/HP/Pr) [wt%]. [1] Total mass and length of POC-1+POC-2

5.11 Measurements in (HP-PO) pilot scale reactor

In Figure 5.29 a typical packing geometry in the (HP-PO) pilot scale spatial profile reactor is shown. The set of experimental runs performed in this reactor and their relevant experimental parameters are summarized in Table 5.10. For liquid phase reactions the flow is fed from bottom to top to avoid channeling of the liquid, which provides an uniform flooding of the reactor. A pre-packing uncoated POC was used as catalyst chair and static mixer to provide pre mixing/heating of the chemicals before the reaction zone. For the experimental run HPPO-1 the reaction zone consisted in a conventional randomly packed catalyst bed while for POC-1 the reaction zone is a structured bed constituted by two catalyst coated POCs packed on top of each other. A post-packing uncoated POC was used as post-reaction zone to provide a defined end to the reaction and stabilize the position of the catalyst particles. A thin layer of silica wool was used to thermally isolate the reaction zone from the pre and post-packing uncoated POCs and to avoid small fragments of catalyst particle to fall in the pre-mixing/heating zone. The reactor coordinate $z = 0$ corresponds to the start of the catalyst bed while negative coordinates corresponds to the pre-packing uncoated POC.

The experiments were carried under the same reaction conditions to be able to compare the heat transport performance of the conventional randomly packed bed against the structured POCs packed bed at same specific flow rate and extent of Pr conversion. Due to increasing issues regarding leakages in the analytic system only the main epoxidation reaction was measured.

In Figure 5.30 a) and c) the concentration of chemical species for the main epoxidation reaction while reaching for steady state is shown. In this case, the stability

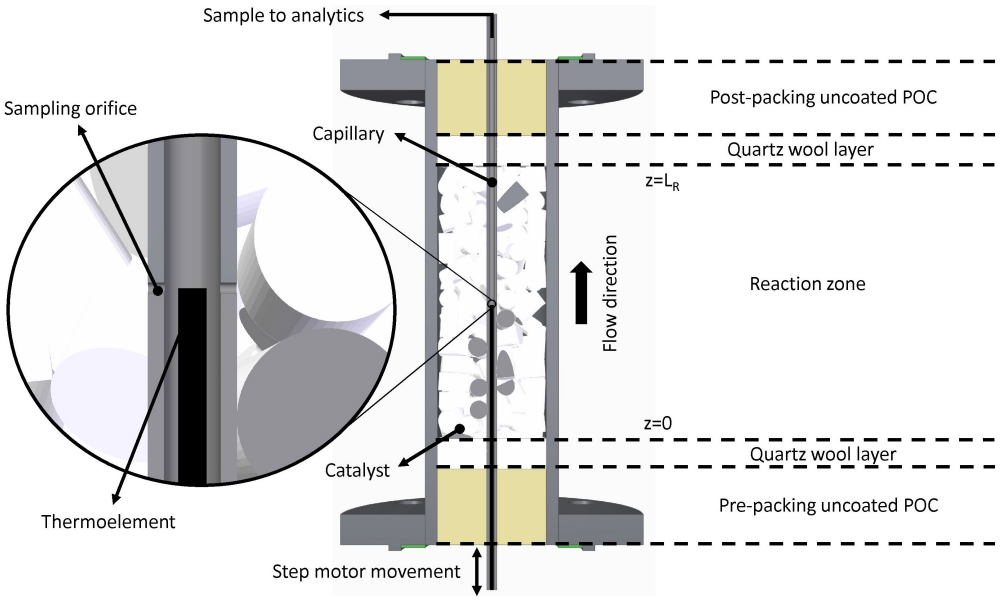

Figure 5.29: HPPO Reactor geometry

of the concentration of PO as a function of time was used as criterion for assuming steady state. This is due to the fact that the side products of reaction could not be measured, and in consequence the carbon balance closure could not be calculated. From the data it can be observed that the concentration of PO remained more or less constant during the time interval considered. This can be attributed to two assumption. The first assumption is that the reaction reached steady state, and therefore the concentration changes are independent of time. The second assumption is that the catalyst is going through a slow induction/activation period as observed in previous experiments (for example on Fresh Cat. experimental run). If the induction period is mass dependent, then the reaction on the pilot scale reactor might take longer to reach steady state. To determine which of these two assumptions is correct, further experiments on the behavior of the reaction while reaching for steady state in the pilot scale spatial profile reactor should be conducted.

The heat transport performance of both approaches can be compared by evaluating the temperature profile at the same level of Pr conversion. The concentration and temperature profiles are shown Figure 5.30 b) and d) while the dotted vertical line indicates the reactor coordinate (z) at which 72% Pr conversion is reached.

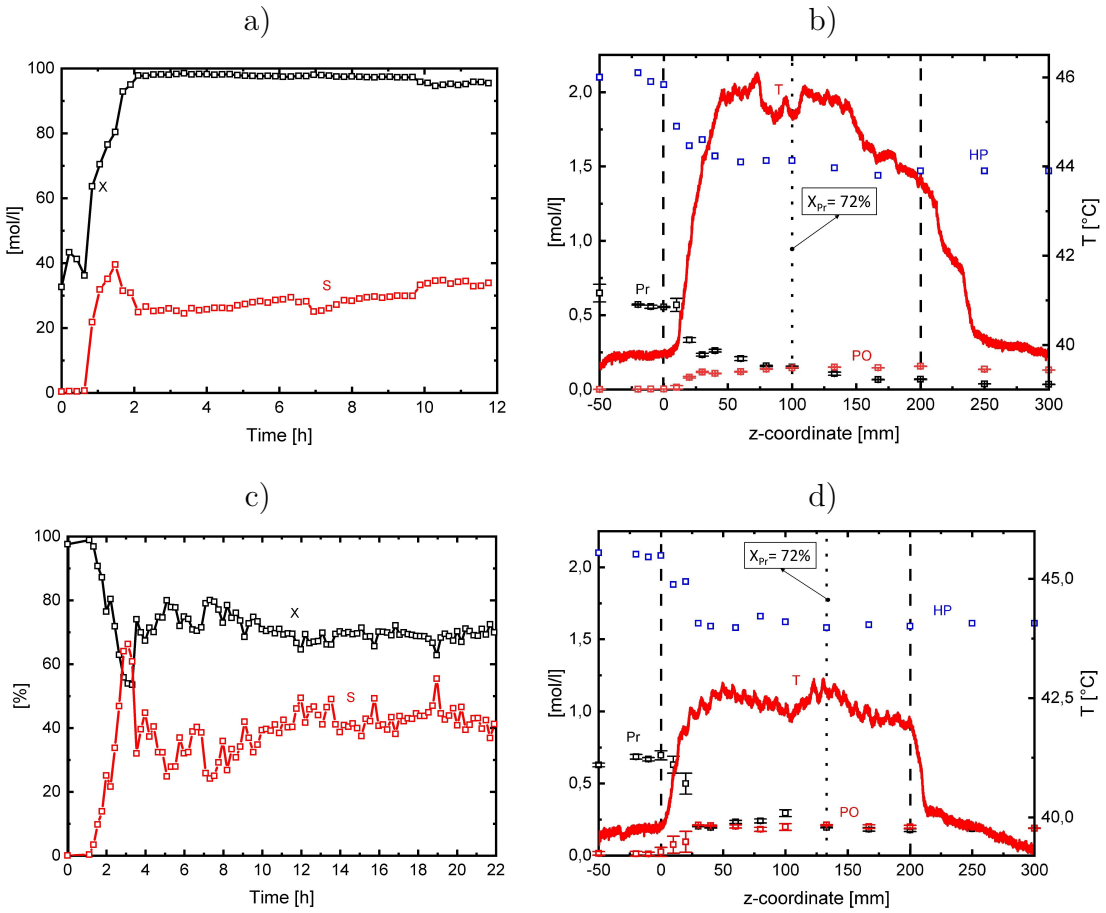

Figure 5.30: Transition towards steady state conventional bed a) (HPPO-1) and c) (POC-01), Concentration and temperature profile conventional bed b) (HPPO-1) and structured POCs bed c) (POC-1). Data measured at 40°C and 30 bar pressure

From the experimental data can be observed a reduction of the local temperature from about 46°C in the case of the conventional randomly packed catalyst bed to 42°C in the case of the structured POCs bed. Additionally, the two approaches can be compared in terms of selectivity (S) and yield (Y) at the same conversion level by the experimental data shown in Figure 5.31 a) and b). For a Pr conversion of 72% the selectivity and yield of the extrudates bed were about 29% and 21% respectively, whereas in the case of the structured bed were 47% and 34%. Therefore according to measured data, there is an improvement of the selectivity towards PO of 18% while the yield was increased by 13%.

Especially at low flow rates, POCs outperform randomly packed beds regarding their heat transfer efficiency. This is because for low Reynolds values (laminar regime), heat conduction dominates over heat convection. In this sense, POCs offer a considerable contribution to the conductive heat transport due to their highly conductive material and their interconnected matrix. To assess the flow regime under the experimental conditions the reactor scale Reynolds number is calculated:

$$Re = \frac{U_0\,\rho_{feed}\,d_R}{\mu_{feed}} = \frac{2.78e-4[m\,s^{-1}]\,859[kg\,m^{-3}]\,0.018[m]}{4.42e-4[Pa\,s]} = 8.27$$

Both MeOH and water are the solvent and co-solvent, therefore both the (μ_{feed}) and (λ_{feed}) were evaluated assuming a 80/20 wt% mixture of these chemical species. The feed density ($\rho_{feed} = 859\,[kg\,m^{-3}]$) was experimentally measured by the spatial sample mass flow meter MFM-1. Due to the fact that the experiments were carried at low specific flow rates to achieve the target $LHSV = 2.0[h^{-1}]$, the resulting flow regime is highly laminar. Therefore under these conditions, the convective influence on the heat transfer becomes negligible and heat conduction in the reactor plays a fundamental role. In consequence, to estimate the heat transport efficiency of the POCs with respect to the randomly packed catalyst bed the thermal conductivity of both approaches can be compared.

The heat conductivity of the catalyst packed bed without flow (λ_{bed}) can be calculated according to Equation 4.1 by assuming that the bed porosity (ϵ) is constant and approximately 0.4. The conductivity of the catalyst particles ($\lambda_p = 1.4\,[W\,m^{-1}\,K^{-1}]$) was assumed to be equal to the conductivity of amorphous silica

nanoparticles, these assumptions resulted in a catalyst packed bed thermal conductivity of ($\lambda_{bed} = 0.67\,[W\,m^{-1}\,K^{-1}]$). In the case of the thermal conductivity of the POCs, it can be estimated by the stagnant conductivity (λ_0) in Equation 3.5, whereas the dispersive (λ_d) and the radiative (λ_{rad}) terms can be considered negligible under the experimental conditions. In this case, the POCs are made of stainless steel 1.4404 with a thermal conductivity ($\lambda_s = 16[W\,m^{-1}\,K^{-1}]$). From the relevant geometrical parameters of the POCs a total porosity ($\epsilon_T = 0.85$) was calculated from Equation 3.6 and a tortuous path of ($\tau = 2.2$), which resulted in a stagnant conductivity ($\lambda_0 = 1.06\,[W\,m^{-1}\,K^{-1}]$). Therefore by comparing the conductive terms of both approaches, the POCs have a 1.58 times higher thermal conductivity with respect to the conventional catalyst packed bed. This improvement on the thermal conductivity can explain the reduction on the local temperature measured experimentally.

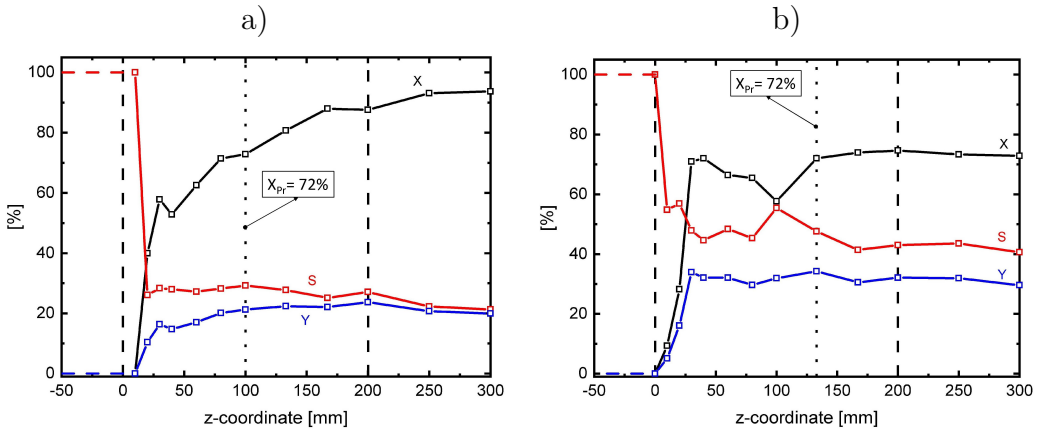

Figure 5.31: Pr conversion (X), PO selectivity (S) and yield (Y) for conventional profiles for a) Conventional bed (HPPO-1), b) Structured POCs bed (POC-1). Data measured at 40°C and 30 bar pressure

The concentration profiles for both experiments exhibit a different behavior. In the case of the concentration profile of HPPO-1 shown in Figure 5.30 b), the concentration of Pr decreases gradually along the reaction zone reaching about total conversion, while PO increases progressively reaching a maximal concentration of 0.2 $[mol\,l^{-1}]$. In the case of the concentration profile of POC-1 shown in Figure 5.30 d), both Pr and PO reached their final concentration of about 0.2 $[mol\ l^{-1}]$ and

0.21 [$mol\ l^{-1}$] respectively at about z= 30 [mm] and remained constant for the rest of the catalyst bed. This flattening of the concentration profile would suggest that the reaction stopped, but this is not supported by the temperature profile which shows that heat is still being generated. A feasible explanation is a channeling effect occurring inside the reaction zone. As can be observed at the reactor coordinate $z = 100[mm]$, there is a slight increase of Pr concentration. This reactor coordinate corresponds exactly to the superposition point of both coated POCs used as structured catalyst. This may suggest that the flow in the reactor is flowing preferentially through the annular space between the POCs and the reactor wall. The underlying mechanism that caused the flattening of the concentration profile is not fully understood and its elucidation requires further experimental data. Due to the fact that in the experiment with the structured POCs the reaction stopped for most of the length of the catalyst bed, the improvements with respect to the conventional randomly packed bed in terms of PO selectivity (S) and reaction yield (Y) measured on this work cannot be conclusively attributed to the enhanced heat transport performance of the POCs and requires further investigation. From the experimental data is not possible to determine what would have happened to the PO selectivity (S) and the yield (Y) if this phenomenon would not have been present throughout the whole extent of the structured bed. Even though questions still remain, these improvements in terms of selectivity and yield are quite significant and may provide a basis for further investigation on the application of periodic open cells structures as alternative packing for fixed bed reactors, most particularly on kinetically limited reaction systems.

6 Summary & Outlooks

This thesis shows for the first time that is possible to measure spatially resolved kinetic data in a heterogeneous catalytic liquid phase reaction under industrially relevant conditions by applying the minimally invasive capillary sampling technique. The reaction studied in this work is the selective liquid phase oxidation of propylene to propylene oxide with hydrogen peroxide over Titanium Silicalite-1 catalyst. Two spatial profile reactors were successfully design, built and brought into operation for the experiments conducted in this thesis. A compact spatial profile reactor was used to conduct kinetic measurements and study the reaction under safe conditions due to the small reacting volume. A pilot scale profile reactor with an internal diameter similar to that of a single tube in industrial scale (HP-PO) reactors was used to compare two different approaches, namely a conventional randomly packed catalyst bed and a structured packed bed prepared by additively manufactured catalyst-coated open cell structures. While most kinetic studies available in the literature performed the reaction far from industrial conditions, the results presented in this work were obtained with reaction conditions similar to those used on industrial scale reactors, that is with pressure high enough to keep propylene entirely in liquid phase.

The measurements performed in the compact profile reactor shows that the catalyst initially undergoes an induction/activation period before reaching steady state. During this period, the concentration of propylene oxide progressively increases and the carbon balance closure slowly decreases. On average it was found that 24 hours of reaction time were required for the propylene oxide to reach an stable concentration and the carbon balance closure to decrease below an acceptable threshold of 10%. As feasible explanations for the observed phenomena two mechanism were proposed. On one hand, it is known that propylene oxide can form high molecular weight oligomers by reacting with the side products of reaction. These

high molecular weight side products can accumulate in the pores of the catalyst leading to the observed difference in the closure of the carbon balance during the transition period. Nevertheless, it was found that this mechanism cannot solely account for the total difference of mass during the transition period towards steady state. As additional explanation, a limitation on the analytical methods applied in this work was proposed. The maximal inlet temperature of the Gas Chromatograph used in this work is 220 °C, therefore oligomers with high boiling point may not be in gas phase as they are injected to the columns of the device and for this reason cannot be correctly measured. Most likely, both proposed mechanism may take place simultaneously. Additionally, it was observed that after a first long induction/activation period subsequent measurements exhibit a shorter activation time. For a fresh catalyst sample, 75 hours were required for the carbon balance closure to reach less than 20 %, while for subsequent measurements with the same catalyst sample took on average 24 hours to reach values below the threshold of 10%. The point at which the carbon balance closure reached less than 10 % was used as criterion to define when the reaction reached steady state. The evidence that subsequent measurements required a significant shorter induction/activation time may suggest that the catalyst requires a chemical treatment with, e.g: hydrogen peroxide/water/methanol solutions, before performing the reaction. The underlying mechanism of this induction/activation period is not fully understood and requires further investigation.

The spatially resolved concentration profiles of the main epoxidation reaction follows a pseudo-zeroth-order behavior. Several DFT simulations have found that the rate determining step in the propylene epoxidation is the adsorption and successive dissociation of hydrogen peroxide on $Ti(SiO)_3OH$ sites forming a Ti-peroxo active specie and a molecule of water. If the reaction rate is given by the dissociative adsorption of hydrogen peroxide and the concentration of hydrogen peroxide molecules far exceeds the number of available Ti sites on the surface of the catalyst the epoxidation rate will limited to the maximial rate at which $Ti(SiO)_3OH$ sites can adsorb and dissociate hydrogen peroxide molecules, leading to the observed pseudo-zeroth-order behavior. In contrast to the main reaction, side reactions exhibit a typical nonlinear trend. Propylene gylcol was measured as dominant side product. Additionally, the presence of hydroxyacetone and methoxyacetone

was detected by GC/MS screening data. These species were not previously reported in the literature. Moreover, hydroxyacetone and methoxyacetone are likely to be formed by the reaction of propylene glycol and methoxypropanol with hydrogen peroxide. The extent of hydrogen peroxide decomposition is considered a safety hazard in technical scale reactors since oxygen and propylene can form explosive mixtures, therefore the accurate quantification of species that consume hydrogen peroxide may be needed to asses accurately the extent of decomposition of hydrogen peroxide within the reactor. Quantitative data for the formation of hydroxyacetone was provided for the first time in this work.

Due to leakages in the gas chromatograph used in this work further kinetic data could not be measured. Most likely, the leakage was caused by small catalyst particles suspended in the spatial sample flow that scratched the surface of a sampling valve. Suspended particles can be caused by the direct movement of the sampling capillary against the catalyst bed which can cause small catalyst particles to detach from the support. These small particles can both damage downstream devices and clog the side sampling orifice of the capillary stopping the experiment. In this sense, it was found that it is necessary to use a quartz liner between the sampling capillary and the catalyst bed to avoid contact between both during the movement of the spatial sampling system. In this regard, special consideration should be taken in the selection of protective component for analytical devices such as in-line filters when dealing with liquid phase reactions and small particles such as the Titanium Silicalite-1 catalyst. Additionally, it was observed that using a stainless steel sampling capillary provides an additional surface from which the heat of reaction can be transported out of the system, thus flattening the temperature profile. To enable the measurement of temperature profiles, the material of the sampling capillary should be substituted by a material with low thermal conductivity such as fused silica.

The acquired kinetic data in this work was used to validate two of the most relevant kinetic model in the scientific literature by simulation using an axial 1D-pseudo-homogeneous dispersion model. It was found that the models could not describe accurately the measured concentration gradients. This might be explain by the fact that both models are based on the assumption that the surface reaction of propylene with $Ti{\bullet}OOH$ active specie is the rate determining step. Additionally, a

new model based on an Eley-Rideal reaction mechanism in which hydrogen peroxide dissociatively adsorbs on a Ti(IV) site forming a $Ti \bullet OOH \bullet H_2O$ active specie and propylene reacts weakly adsorbed to form propylene oxide was proposed. The rate determining step of the derived rate law equation for the epoxidation reaction is the dissociative adsorption of hydrogen peroxide on Ti(IV) species which is in agreement with the relevant DFT studies in the literature. The experimental differential rate shows a linear trend with $R^2 = 0.99$ and $R^2 = 0.98$ when plotted according to the linearized form of the derived rate law for the main epoxidation reaction. The small deviation from linearity of the experimental differential rate can be explain by the fact that the parameters of the main epoxidation reaction are not truly constant values, as hydrogen peroxide adsorption/dissociation and epoxidation reaction constants depend also on the local temperature. Statistical analysis showed that the proposed Eley-Rideal model has the lowest standard deviation and F_C value from the different kinetic models evaluated in this work.
For the fitting of the proposed model to the experimental data the main reaction pre-exponential factor and the hydrogen peroxide adsorption/dissociation constant were determined experimentally, while other kinetic parameters were taken from the model of Sulimov [84]. It was observed that the proposed model is not able to fully capture the non-linear trends of the side products concentration profiles in the first 10-15 mm of the catalyst bed, where pronounced temperature variations occur. These deviations with respect to the experimental data suggest that the model parameters require further optimization. An improvement in the accuracy of the model can be achieved by an experimental determination of all kinetic parameters, namely the reaction pre-exponential factors, activation energies, adsorption constant and adsorption enthalpies. For this, a systematic study of the reaction dependence on the temperature and the initial concentration of chemical species should be conducted. Moreover, the minimal invasive sampling technique can be integrated with different spectroscopic methods such a Raman spectroscopy. Both Xiong [101] and Bordiga [103] showed that the Titanium Silicalite-1 catalyst exhibit a resonance feature which allows the enhancement of the Raman signal by several order of magnitude. In this sense, the integration of a systematic study of the reaction parameters combined with a direct spectroscopic measurement of the surface intermediates while performing the reaction under industrial conditions

in the developed spatial experimental setups, has the potential of providing unprecedented insights into the reaction mechanism and would constitute the most comprehensive study on this industrially relevant reaction so far.

A pilot scale profile reactor was used to compare the performance of a structured packed bed prepared by additively manufactured catalyst-coated open cell structures against a conventional randomly packed bed under the same reaction conditions and conversion. At a propylene conversion of 72% a reduction of the local temperature from 46°C to 42°C was observed for the randomly packed bed and the open cell structures respectively. Additionally, an increase of the selectivity toward propylene oxide of about 18% and of the yield of reaction of about 13% was measured. Nevertheless, these improvements with respect to the conventional randomly packed bed cannot be attributed conclusively to the enhanced thermal transport properties of the open cell structures. Due to increasing problems with leakages in the analytical device used in this work only the main epoxidation reaction could be measured. For this reason, the carbon balance closure could not be calculated and the experimental data was measured by assuming that the reaction reached steady state once the concentration of propylene oxide remained stable for about 5 hours. In this sense, the experimental data might have been obtained while the catalyst in the pilot scale reactor was undergoing an induction/activation transition period similar to the one observed in the compact reactor. Future measurements should be performed measuring all products of reaction. The point at which the steady state is reached in the pilot scale profile reactor should be studied by continuously monitoring the species concentration at the outlet of the reactor and plotting the carbon balance closure as a function of time. Additionally, the concentration profiles of the bed constituted by catalyst-coated open cell structures showed an abnormal behavior. At the reactor coordinate z=30 $[mm]$ the reaction seems to stop and the concentration of chemical species remained constant for the remaining length of the catalyst bed. This flattening of the concentration profile would suggest that the reaction stopped, but this is not supported by the temperature profile which shows that heat is still being generated. A feasible explanation is a channeling effect causing the chemical species to flow preferentially through the annular space between the catalyst-coated open cells and the reactor wall. From the experimental data is not possible to determine if the improvements

in terms of propylene oxide selectivity and reaction yield would have remained if the reaction would had proceeded without flattening of the concentration profile. In this sense, further investigation to explain this abnormal behavior should be conducted. Even though the results are not conclusive, the measured improvements in terms of selectivity and yield are quite significant and may provide a basis for further investigation on the application of periodic open cells structures as alternative packing for fixed bed reactors, most particularly on kinetically limited reaction systems.

In conclusion, the minimal invasive sampling technique was successfully applied in both a compact and a pilot scale profile reactors which underlines the robustness and versatility of this technique. Moreover, it was shown that this measurement principle can provide a significant amount of kinetic data which can be used to validate kinetic models from literature and develop models that can accurately describe the concentration gradients inside of the catalyst bed. This measurement principle can be integrated with several spectroscopic methods, which allows to probe structure and reactivity of the catalyst as a function of the local process conditions inside the reactor. These insights into the chemical and physical processes occurring inside of the reactor under real industrial conditions can be used as basis to substitute trial and error approaches with a knowledge based design of the catalytic process.

7 Appendix

7.1 Evaluation of transport limitations and dispersion

All parameters used for the evaluation of transport limitation are given in Table 7.1, while the results of the calculation can be found in Table 7.2

Mears [129]: External mass transport limitation

The mass transfer coefficient was calculated with the correlation provided in the work of Freek Kapteijn and Jacob A. Moulijn for liquids flowing through packed beds with $0.0016 < Re_p < 55$ [129]. The diffusion coefficients for the chemicals species through the bulk solvent were calculated by the Wilke-Chang equation for diffusion in liquids [164]. External mass transport limitation was evaluated both experimentally and analytically. The experimental evaluation of external mass transport limitations can be found in the main body of the thesis.

$$\frac{r_{obs} r_p n}{k_c C_b} < 0.15$$

(r_{obs}): volume based observed reaction rate in $[mol\ m^{-3}\ s^{-1}]$
(r_p): catalyst particle radius in $[m]$
(n): reaction order $[-]$
k_c: mass transfer coefficient $[m^2\ s^{-1}]$
C_b: bulk concentration of Pr $[mol\ m^{-3}]$

Weisz-Prater [141]: Internal mass transport limitation

After the exclusion of external mass transfer limitations it can be assumed that the surface concentration of propylene (C_s) is equal to the bulk fluid concentration (C_b)

$$\frac{R_{obs} r_p^2}{C_s D_{eff}} \leq 0.3$$

$$D_{eff} = \frac{\epsilon_p D_{C_3H_6}}{\tau}$$

C_s: surface concentration of Pr $[mol\, m^{-3}]$
D_{eff}: effective diffusion coefficient of Pr $[m^2\, s^{-1}]$
$D_{C_3H_6}$: diffusion coefficient of Pr $[m^2\, s^{-1}]$
ϵ_p: catalyst porosity $[-]$
τ: catalyst tortuosity $[-]$

Mears [140]: External heat transport limitation

Potential heat transfer limitations were evaluated by assuming that only the main reaction, the selective oxidation of propylene to propylene oxide contributes to heat formation in the system. Activation energy was adopted from the previously developed model by Sulimov [84] . The heat transfer coefficient was estimated according to literature [162].

$$\frac{|\Delta H_r|\, R_{obs} r_p}{h T_b} \leq 0.15 \frac{T_b R}{E_a}$$

(ΔH_r): heat of reaction in $[J\, mol^{-1}]$
(h): heat transport coefficient $[W\, m^{-2}\, K^{-1}]$
(T_b): temperature of the bulk fluid $[K]$
(E_a): reaction activation energy $[J\, mol^{-1}]$
(R): Universal gas constant $[J\, mol^{-1}\, K^{-1}]$

Anderson [140]: Internal heat transport limitation

After the exclusion of external mass transfer limitations it can be assumed that the surface temperature of the catalyst (T_s) is equal to the bulk fluid temperature (T_b)

$$\frac{|\Delta H_r| R_{obs} r_p^2}{\lambda T_b} \leq 0.75 \frac{T_b R}{E_a}$$

(λ): catalyst thermal conductivity $[W\ m^{-1}\ K^{-1}]$
(T_s): temperature at the surface of the catalyst $[K]$

Axial dispersion at reactor scale

If $Bo > 80$, the deviations from ideal plug flow are small and the reactor can be regarded as a cascade of N CSTRs.

$$N = \frac{Bo}{2} = \frac{Pe_{m,ax}}{2} \frac{l}{d_p} \qquad \text{(liquids, } \mathrm{Re_p}<100\text{)}$$

Table 7.1: Overview of parameters applied for the evaluation of transport limitations at reactor scale

Parameter	Description	Value	Units
r_{obs}	volume based observed reaction rate	$1,02$	$[mol \quad m^{-3}\, s^{-1}]$
r_p	catalyst particle radius	$1,88 \times 10^{-4}$	$[m]$
n	reaction order	1	$[-]$
k_c	mass transfer coefficient	$3,8 \times 10^{-5}$	$[m\, s^{-1}]$
$C_s = C_b$	surface and bulk concentration	650	$[mol\, m^{-3}]$
D_{eff}	effective diffusion coefficient	5.8×10^{-10}	$[m^2\, s^{-1}]$
$D_{C_3H_6}$	effective diffusion coefficient	3.52×10^{-9}	$[m^2\, s^{-1}]$
ϵ_p	catalyst porosity	0.5	$[-]$
τ	catalyst tortuosity	3	$[-]$
ΔH_r	heat of reaction	$-151,09 \times 10^3$	$[J\, mol^{-1}]$
h	heat transport coefficient	324.2	$[W\, m^{-2}\, K^{-1}]$
$T_s = T_b$	surface and bulk temperatures	313.15	$[K]$
E_a	activation energy	46.5×10^3	$[J\, mol^{-1}]$
R	universal gas constant	$8,314$	$[J\, mol^{-1}\, K^{-1}]$
λ	catalyst thermal conductivity	$1,4$	$[W\, m^{-1}\, K^{-1}]$
$Pe_{m,ax}$	particle axial Peclet number	$0,5$	$[-]$
l	bed length	60×10^{-3}	$[m]$

Table 7.2: Overview of dimensionless criterion evaluated to test for the significance of external/internal mass and heat transfer limitations as well as axial dispersion at reactor scale

	Criterion	Calculated Value	Limit
External mass limitation	Mears	$0,0077$	$< 0,15$
Internal mass limitation	Weisz-Prater	$0,094$	$\leq 0,3$
External heat limitation	Mears	$2,84 \times 10^{-4}$	$< 8,4^{-3}$
Internal heat limitation	Anderson	$1,23 \times 10^{-5}$	$< 4,1^{-2}$
Axial Dispersion	Bodenstein	$70,6$	> 80

7.2 Kinetic parameters used for numerical simulations

Table 7.3: Sulimov model parameters [84]

Parameter	Value	Units	Parameter	Value	Units
k_{1°	$3.64x10^2$	$\left[\frac{l}{(g*s)}\right]$	E_1	$4.50x10^4$	$\left[\frac{J}{mol}\right]$
k_{2°	$1.31x10^2$	$\left[\frac{l}{(g*s)}\right]$	E_2	$6.06x10^4$	$\left[\frac{J}{mol}\right]$
k_{3°	$2.35x10^2$	$\left[\frac{l}{(g*s)}\right]$	E_3	$6.35x10^4$	$\left[\frac{J}{mol}\right]$
k_{4°	$2.66x10^2$	$\left[\frac{l}{(g*s)}\right]$	E_4	$6.30x10^4$	$\left[\frac{J}{mol}\right]$
k_{5°	$4.96x10^2$	$\left[\frac{l}{(g*s)}\right]$	E_5	$4.98x10^4$	$\left[\frac{J}{mol}\right]$
$b^\circ{}_{H_2O_2}$	$5.00x10^{-4}$	$\left[\frac{l}{mol}\right]$	$Q^\circ{}_{H_2O_2}$	$1.87x10^4$	$\left[\frac{J}{mol}\right]$
$b^\circ{}_{C_3H_6O}$	$1.83x10^{-3}$	$\left[\frac{l}{mol}\right]$	$Q^\circ{}_{C_3H_6O}$	$2.05x10^4$	$\left[\frac{J}{mol}\right]$

Table 7.4: Di Serio model parameters [83]

Parameter	Value	Units	Parameter	Value	Units
$k_{1_{ref^*}}$	$4.97x10^{-1}$	$\left[\frac{l}{(g*s)}\right]$	E_1	$4.56x10^4$	$\left[\frac{J}{mol}\right]$
$k_{d1_{ref^*}}$	$1.97x10^{-3}$	$\left[\frac{l^2}{(g*mol*s)}\right]$	E_{d1^*}	$1.06x10^5$	$\left[\frac{J}{mol}\right]$
$k_{d2_{ref^*}}$	$5.18x10^{-6}$	$\left[\frac{l^2}{(g*mol*s)}\right]$	E_{d2^*}	$1.26x10^5$	$\left[\frac{J}{mol}\right]$
$k_{d3_{ref^*}}$	$7.33x10^{-4}$	$\left[\frac{l^2}{(g*mol*s)}\right]$	E_{d3^*}	$1.47x10^5$	$\left[\frac{J}{mol}\right]$
$k_{d4_{ref^*}}$	$5.18x10^{-6}$	$\left[\frac{l^2}{(g*mol*s)}\right]$	E_{d4^*}	$1.26x10^5$	$\left[\frac{J}{mol}\right]$
$k_{d1_{ref}}$	$1.58x10^{-7}$	$\left[\frac{l^2}{(g*mol*s)}\right]$	E_{d1}	$4.48x10^4$	$\left[\frac{J}{mol}\right]$
$k_{d2_{ref}}$	$1.01x10^{-7}$	$\left[\frac{l^2}{(g*mol*s)}\right]$	E_{d2}	$1.42x10^5$	$\left[\frac{J}{mol}\right]$
$k_{d3_{ref}}$	$1.90x10^{-7}$	$\left[\frac{l^2}{(g*mol*s)}\right]$	E_{d3}	$6.69x10^4$	$\left[\frac{J}{mol}\right]$
$k_{d4_{ref}}$	$1.01x10^{-7}$	$\left[\frac{l^2}{(g*mol*s)}\right]$	E_{d4}	$1.42x10^5$	$\left[\frac{J}{mol}\right]$
$k_{d_{ref}}$	$4.08x10^{-7}$	$\left[\frac{l}{(g*s)}\right]$	E_d	$8.16x10^4$	$\left[\frac{J}{mol}\right]$
K_{ads_1}	$3.47x10^{-3}$	$\left[\frac{l}{mol}\right]$	K_{ads_2}	$8.28x10^0$	$\left[\frac{l}{mol}\right]$
K_{ads_3}	$4.54x10^{-1}$	$\left[\frac{l}{mol}\right]$	K_{ads_4}	$7.58x10^0$	$\left[\frac{l}{mol}\right]$

List of Abbreviations

1-MPOL	1-methoxy-2-propanol
2-MPOL	2-methoxy-1-propanol
CPR	Compact Profile Reactor
E-R	Eley Rideal
HA	Hydroxyacetone
HP	Hydrogen Peroxide
HP-PO	Hydrogen peroxide-propylene oxide
L-H	Langmuir Hinshelwood
LHSV	Liquid hourly space velocity
MA	Methoxyacetone
MeOH	Methanol
MPOL	Methoxypropanol

MTBE	Methyl tert butyl ether
PG	Propylene Glycol
PO	Propylene oxide
PO-CH	Propylene oxide-cumene hydroperoxide
POCs	Periodic open cell structures
PO-SM	Propylene oxide-styrene monomer
PO-MTBE	Propylene oxide-methyl tert-butyl ether
Pr	Propylene
TEOS	Tetraethyl orthosilicate
TEOT	Tetraethyl orthotitanate
TPAOH	Tetrapropylammonium hydroxide
TS-1	Titanium Silicalite-1

List of Figures

3.1 Reactions of the industrially relevant production processes for propylene oxide. Adopted from [15] 5
3.2 Reaction scheme for the epoxidation and total oxidation reaction pathways for Pr and ethylene over silver catalyst. Taken from [53] . 9
3.3 BASF/DOW HP-PO process simplified flow chart 11
3.4 Evonik/Thyssenkrupp HP-PO process simplified flow chart 12
3.5 TS-1 structure, Si(grey) and Ti(black) tetrahedral connected via oxygen bridges (white) (taken from [64]) 13
3.6 Eley-Rideal mechanisms (left) HP adsorbed, Pr free. (right) Pr adsorbed, HP free 19
3.7 Langmuir-Hinshelwood mechanisms (left) HP and Pr adsorbed on a single active site. (right) HP and Pr adsorbed on different active sites 19
3.8 Reaction network and chemical species considered by a) Di Serio [83] b) Sulimov [84] 20
3.9 Resonance effect on the Ti-peroxo complex in a the TS-1/H_2O/H_2O_2 system taken from [103]: (Top) UV-vis diffusive reflectance spectroscopy spectra showing the electronic adsorption of the sample at 385 nm do to the ligand to metal charge transfer. (Bottom) Raman spectra measured with a 442 nm laser line before and after interaction with H_2O/H_2O_2, doted and solid lines respectively . . . 23
3.10 a) Five membered ring active site proposed by Clerici et. al. [97] b) 6-coordinated active site proposed by Xiong et. al. [108] c) Dinuclear active site proposed by Gordon et. al. [107] 25

3.11 Three defective active sites proposed by Xiong et. al. [108]. a) Defective site from hydration of perfect tetrahedral $Ti(SiO)_4$, b) Defective site located in a Si vacancy c) Defective site located on the surface of the catalyst 25
3.12 DFT stepwise mechanistic scheme of Pr epoxidation on tripodal (1I) site of TS-1 catalyst. Taken from [106] 25
3.13 Influence of different reaction media on the epoxidation of Pr (taken from [92]) 27
3.14 LLE diagram for the Pr-MeOH-Water mixture at 40°C (taken from [110]) 27
3.15 Comparison of different packed reactors and their properties taken from [114] 28
3.16 a)Comparison of the overall heat transfer coefficient of a diamond POCS and a randomly packed bed. b) Diamond unit cell with important geometric properties strut diameter d_s, cell length l_c, window diameter d_w, and strut length l_s. Figures taken from [116] . 29
3.17 Differential and Integral experimental fixed bed reactors 33
3.18 Sketch of SpaciMS Instrument (taken from [8]) 35
3.19 Picture of opened channel reactor with catalyst plate(taken from [9]) 35
3.20 Spatial sampling principle by Horn: (Left) Magnified view of sampling arrangement for measurement of local concentration and temperature. (Center) Sectional view of a experimental spatial fixed bed reactor. (Right) Spatially resolved concentration and temperature profile. 36
3.21 Steps in heterogeneous catalytic reaction 37
3.22 Experimental test for external mass transfer limitations 38
3.23 Experiment test for internal mass transfer limitations 39

4.1 TS-1/SiO_2 pellets and TS-1/SiO_2 splits 43
4.2 a) and b) POCs dip-coating device, c) Periodic open cell structure POCs. Taken from [146] 44
4.3 Condensation reaction of silanol groups on the surface of silica particles 44

4.4 Typical sigmoidal titration curve and its first derivative as a function of titrant volume 46
4.5 Potentiometric Titration Unit TitroLine 7000 SI Analytics 47
4.6 (Up) GC Diagram OFF Positions. Outside GC (Blue), red (Valve box), grey (Oven). (Down) GC injection valves arrangement 48
4.7 Classification of classical continuum models 49
4.8 Axial and Radial Peclet numbers as a function of the particle Reynolds number for packed beds, take from [158] 51

5.1 Simplified flow diagram of experimental setup 58
5.2 (left) Scheme of the pilot scale liquid phase profile reactor (middle) Sectional cut of the spatial sealing concept (right) Pilot scale profile reactor 60
5.3 (left) Compact profile reactor (right) Feed modules 61
5.4 3D model of MFC-1, MFC-2, MFC-3 and pump modules 65
5.5 a) TS-1/SiO_2 catalyst diffraction pattern, b) FT-IR spectrum of the TS-1 catalyst powder 66
5.6 SEM images of a) Catalyst pellet b) TS-1 agglomerated particles c) Catalyst splits 66
5.7 Dip coating cycles 1 to 3. Taken from [146] 66
5.8 Dip coating cycles 4 to 6. Taken from [146] 67
5.9 GC/MS data, taken from [176] 68
5.10 a) CPR Reactor geometry and b) Typical operation point of experimental runs. 73
5.11 Mass Transfer limitation experiment, 3 hours between each measurement 74
5.12 Experimental data Ext. Lim.. a) HP conversion (X_{HP}), Pr conversion (X_{Pr}) and PO selectivity (S) , b) Main products concentrations. Measured at constant space time LHSV = 3 [h^{-1}], 40°C and 20 bar pressure 75

5.13 Transition towards steady state for Fresh Cat.: Pr conversion (X), PO selectivity (S), carbon balance closure and products distribution. Measured at 40°C and 20 bar pressure. Note: main products Pr and PO in $[mol\ l^{-1}]$ (left axis), side products 1-MPOL, 2-MPOL, PG and HA in $[mmol\ l^{-1}]$ (right axis). 78
5.14 Transition towards steady state for CPR-1: Pr conversion (X), PO selectivity (S), carbon balance closure and products distribution. Measured at 40°C and 20 bar pressure. Note: main products Pr and PO in $[mol\ l^{-1}]$ (left axis), side products 1-MPOL, 2-MPOL, PG and HA in $[mmol\ l^{-1}]$ (right axis). 79
5.15 Transition towards steady state for CPR-2: Pr conversion (X), PO selectivity (S), carbon balance closure and products distribution. Measured at 40°C and 20 bar pressure. Note: main products Pr and PO in $[mol\ l^{-1}]$ (left axis), side products 1-MPOL, 2-MPOL, PG and HA in $[mmol\ l^{-1}]$ (right axis). 79
5.16 Transition towards steady state for CPR-3: Pr conversion (X), PO selectivity (S), carbon balance closure and products distribution. Measured at 40°C and 20 bar pressure. Note: main products Pr and PO in $[mol\ l^{-1}]$ (left axis), side products 1-MPOL, 2-MPOL, PG and HA in $[mmol\ l^{-1}]$ (right axis). 80
5.17 Difference between outlet and inlet mass flow rates $\Delta\dot{m} = \dot{m}_{outlet} - \dot{m}_{inlet}$ as a function of time during the transition towards steady state. a) Fresh Cat, b) CPR-1. Measured at 40°C and 20 bar pressure. 80
5.18 Difference between outlet and inlet mass flow rates $\Delta\dot{m} = \dot{m}_{outlet} - \dot{m}_{inlet}$ as a function of time during the transition towards steady state. a) CPR-2, b) CPR-3. Measured at 40°C and 20 bar pressure. 81
5.19 Experimental data CPR-1: a) Main epoxidation reaction concentration profile, b) Side reactions concentration profiles, c) PO selectivity (S) and Pr conversion (X), d) Carbon balance closure as a function of coordinate (z). Measured at 40°C and 20 bar pressure. Note: Triangle data point: interpolated data, square data point: measured data. 85

5.20 Experimental data CPR-2: a) Main epoxidation reaction concentration profile, b) Side reactions concentration profiles, c) PO selectivity (S) and Pr conversion (X), d) Carbon balance closure as a function of coordinate (z). Measured at 40°C and 20 bar pressure. Note: Triangle data point: interpolated data, square data point: measured data. 86
5.21 Experimental data CPR-3: a) Main epoxidation reaction concentration profile, b) Side reactions concentration profiles, c) PO selectivity (S) and Pr conversion (X) , d) Carbon balance closure as a function of coordinate **(z)**. Measured at 40°C and 20 bar pressure. Note: Triangle data point: interpolated data, square data point: measured data. 87
5.22 Simulated concentration, temperature, Pr conversion (X) and PO selectivity (S) profiles for data set CPR-1 by Di Serio [83]. Note: Numerical simulation (solid lines). Experimental data (squares with error bars). 91
5.23 Simulated concentration, temperature, Pr conversion (X) and PO selectivity (S) profiles for data set CPR-1 by Sulimov [84]. Note: Numerical simulation (solid lines). Experimental data (squares with error bars). 91
5.24 Simulated concentration, temperature, Pr conversion (X) and PO selectivity (S) profiles for data set CPR-2 by Sulimov [84]. Note: Numerical simulation (solid lines). Experimental data (squares with error bars). 92
5.25 Simulated concentration, temperature, Pr conversion (X) and PO selectivity (S) profiles for data set CPR-3 by Sulimov [84]. Note: Numerical simulation (solid lines). Experimental data (squares with error bars). 92
5.26 Experimental $[C_3H_6]/r_2$ as a function of $[C_3H_6]/[H_2O_2]$ a) CPR-1, b) CPR-2 98
5.27 Experimental $[C_3H_6]/r_n$ as a function of $[C_3H_6]/[H_2O_2]$ for (r_4), (r_5) and (r_6) 99

5.28 Derived Eley-Rideal model and experimental data CPR-1 (top row) a), b), c). CPR-2 (center row) d), e), f). CPR-3 (bottom row) g), h), i). Concentration, temperature, Pr conversion (X) and PO selectivity (S) profiles. Note: Numerical simulation (solid lines), Experimental data (squares with error bars). 101
5.29 HPPO Reactor geometry 105
5.30 Transition towards steady state conventional bed a) (HPPO-1) and c) (POC-01), Concentration and temperature profile conventional bed b) (HPPO-1) and structured POCs bed c) (POC-1). Data measured at 40°C and 30 bar pressure 106
5.31 Pr conversion (X), PO selectivity (S) and yield (Y) for conventional profiles for a) Conventional bed (HPPO-1), b) Structured POCs bed (POC-1). Data measured at 40°C and 30 bar pressure 108

List of Tables

3.1 List of relevant publications about HPPO kinetics E-R= Eley-Rideal, L-H= Langmuir-Hinshelwood 16
3.2 Kinetic models by Sulimov and Di Serio 21

4.1 List of Chemicals used 41
4.2 Boundary conditions of axial 1D pseudo-homogenous dispersion model 53

5.1 Main Characteristics of pilot scale (HP-PO) reactor 60
5.2 Main Characteristics of CPR reactor 62
5.3 Main Characteristics of feed modules 64
5.4 Results of dip-coating procedures. Taken from [146] 67
5.5 List of parameters of experiment GC/MS 68
5.6 Main parameters of experimental runs 72
5.7 Proposed reaction mechanism 95
5.8 Statistical comparison of models for CPR-1 103
5.9 Parameters derived Eley-Rideal model 103
5.10 List of parameters of experiments HPPO-1 and POC-1 104

7.1 Overview of parameters applied for the evaluation of transport limitations at reactor scale 119
7.2 Overview of dimensionless criterion evaluated to test for the significance of external/internal mass and heat transfer limitations as well as axial dispersion at reactor scale 120
7.3 Sulimov model parameters [84] 120
7.4 Di Serio model parameters [83] 121

Bibliography

[1] M. Boudart, Heterogeneous Catalysis by Metals, J. Mol. Catal. 30 (1-2) (1985) 27–38.

[2] G. Rothenberg, Catalysis: Concepts And Green Applications, John Wiley & Sons, 2017.

[3] M. Geske, O. Korup, R. Horn, Resolving Kinetics and Dynamics of a Catalytic Reaction Inside a Fixed Bed Reactor by Combined Kinetic and Spectroscopic Profiling, Catal. Sci. Technol. 3 (1) (2013) 169–175.

[4] R. Horn, O. Korup, M. Geske, U. Zavyalova, I. Oprea, R. Schlögl, Reactor for In Situ Measurements of Spatially Resolved Kinetic Data in Heterogeneous Catalysis, Rev. Sci. Instrum. 81 (6) (2010) 064102.

[5] M. A. Bañares, M. O. Guerrero-pérez, J. L. G. Fierro, G. G. Cortez, Raman Spectroscopy During Catalytic Operations with On-Line Activity Measurement (Operando Spectroscopy): A Method for Understanding the Active Centres of Cations Supported on Porous Materials, J. Mater. Chem. 12 (11) (2002) 3337–3342.

[6] S. J. Tinnemans, J. G. Mesu, K. Kervinen, T. Visser, T. A. Nijhuis, A. M. Beale, D. E. Keller, A. M. Van Der Eerden, B. M. Weckhuysen, Combining Operando Techniques in One Spectroscopic-Reaction Cell: New Opportunities for Elucidating the Active Site and Related Reaction Mechanism in Catalysis, Catal. Today 113 (1-2) (2006) 3–15.

[7] W. P. Partridge, J. M. Storey, S. A. Lewis, R. W. Smithwick, G. L. Devault, M. J. Cunningham, N. W. Currier, T. M. Yonushonis, Time-Resolved Measurements of Emission Transients by Mass Spectrometry, SAE Trans. (2000) 2983–2991.

[8] J. Sá, D. L. A. Fernandes, F. Aiouache, A. Goguet, C. Hardacre, D. Lundie, W. Naeem, W. P. Partridge, C. Stere, Spacims: Spatial and Temporal Operando Resolution of Reactions Within Catalytic Monoliths, Analyst 135 (9) (2010) 2260–2272.

[9] J. Kopyscinski, T. J. Schildhauer, F. Vogel, S. M. Biollaz, A. Wokaun, Applying Spatially Resolved Concentration and Temperature Measurements in a Catalytic Plate Reactor for the Kinetic Study of CO Methanation, J. Catal. 271 (2) (2010) 262–279.

[10] F. Meemken, P. Müller, K. Hungerbühler, A. Baiker, Simultaneous Probing of Bulk Liquid Phase and Catalytic Gas-Liquid-Solid Interface Under Working Conditions Using Attenuated Total Reflection Infrared Spectroscopy, Rev. Sci. Instrum. 85 (8) (2014) 084101.

[11] O. Korup, S. Mavlyankariev, M. Geske, C. F. Goldsmith, R. Horn, Measurement and Analysis of Spatial Reactor Profiles in High Temperature Catalysis Research, Chem. Eng. Process. 50 (10) (2011) 998–1009.

[12] R. Horn, In-Situ Measurements of Spatially Resolved Spectroscopic Data Within a Reactor Chamber of a Reactor, uS Patent 9,400,253 (2016).

[13] P. Bassler, M. Weidenbach, H. Goebbel, The New HPPO Process for Propylene Oxide: From Joint Development to Worldscale Production, Chem. Eng. Trans. 21 (2010) 571–576.

[14] T. A. Nijhuis, M. Makkee, J. A. Moulijn, B. M. Weckhuysen, The Production of Propene Oxide: Catalytic Processes and Recent Developments, Ind. Eng. Chem. Res. 45 (10) (2006) 3447–3459.

[15] F. Schmidt, M. Bernhard, H. Morell, M. Pascaly, HPPO Process Technology a Novel Route to Propylene Oxide without Coproducts, Chem. Today 32 (2) (2014) 31–35.

[16] W. F. Richey, Chlorohydrins, Kirk-Othmer Encycl. Chem. Technol. (2000).

[17] V. Russo, R. Tesser, E. Santacesaria, M. Di Serio, Chemical and Technical Aspects of Propene Oxide Production Via Hydrogen Peroxide, Ind. Eng. Chem. Res. 52 (3) (2013) 1168–1178. doi:10.1021/ie3023862.

[18] M. Becker, DE 1939791 (1979).

[19] H. Baer, M. Bergamo, A. Forlin, L. H. Pottenger, J. Lindner, Propylene Oxide, American Cancer Society, 2012. doi:10.1002/14356007.a22_239.pub3.

[20] T. Seo, J. Tsuji, Process for Producing Propylene Oxide, uS Patent 6,646,139 (2003).

[21] J. Schmidt, DE 2617432 (1979).

[22] E. L. Lines, R. J. Fairbrother, J. A. Herbst, Catalytic Epoxidation of Alkylene Compounds, uS Patent 4,157,346 (1979).

[23] H. Wulff, US 3829392 (1974).

[24] M. Rameswaran, R. N. Cochran, Epoxidation Process, US Patent 5,081,267 (1992).

[25] J. G. Zajacek, G. L. Crocco, Integrated Process for Epoxide Production, US Patent 5,214,168 (1993).

[26] K. H. Simmrock, Die Herstellungsverfahren für Propylenoxid und Ihre Elektochemische Alternative, Chem. Ing. Tech. 48 (12) (1976) 1085–1096.

[27] J. Tsuji, J. Yamamoto, M. Ishino, N. Oku, Development of New Propylene Oxide Process, Sumitomo Kagaku 1 (2006) 4–10.

[28] T. Junpei, I. Yoshiaki, S. Koji, Method for Producing Propylene Oxide (2006).
URL http://v3.espacenet.com/textdoc?DB=EPODOC&IDX=EP1837334

[29] Y. Jun, G. Shigeru, Method for Producing Propylene Oxide (Feb. 2010).
URL https://lens.org/147-859-538-937-376

[30] T. Junpei, I. Masaru, Process for Producing Cumene, EP 1598330 A1 (Nov. 2005).

[31] R. Van Santen, H. Kuipers, The Mechanism of Ethylene Epoxidation, Adv. Catal. 35 (1987) 265–321.

[32] J. R. Monnier, The Direct Epoxidation of Higher Olefins Using Molecular Oxygen, Appl. Catal., A 221 (1-2) (2001) 73–91.

[33] G. Lu, X. Zuo, Epoxidation of Propylene by Air Over Modified Silver Catalyst, Catal. Lett. 58 (1) (1999) 67–70.

[34] J. Lu, M. Luo, H. Lei, C. Li, Epoxidation of Propylene on NaCl-Modified Silver Catalysts with Air as the Oxidant, Appl. Catal., A 237 (1-2) (2002) 11–19.

[35] J. Lu, J. J. Bravo-suárez, M. Haruta, S. T. Oyama, Direct Propylene Epoxidation Over Modified Ag/CaCo3 Catalysts, Appl. Catal., A 302 (2) (2006) 283–295.

[36] G. Jin, G. Lu, Y. Guo, Y. Guo, J. Wang, X. Liu, Epoxidation of Propylene by Molecular Oxygen Over Modified Ag–MoO3 Catalyst, Catal. Lett. 87 (3) (2003) 249–252.

[37] G. Jin, G. Lu, Y. Guo, Y. Guo, J. Wang, X. Liu, Direct Epoxidation of Propylene with Molecular Oxygen Over Ag–MoO3/ZrO2 Catalyst, Catal. Today 93 (2004) 173–182.

[38] W. Yao, G. Lu, Y. Guo, Y. Guo, Y. Wang, Z. Zhang, Promotional Effect of Y2O3 on the Performance of Ag/α-Al2O3 Catalyst for Epoxidation of Propylene with Molecular Oxygen, J. Mol. Catal. A: Chem. 276 (1-2) (2007) 162–167.

[39] W. Yao, Y. L. Guo, X. H. Liu, Y. Guo, Y. Q. Wang, Y. S. Wang, Z. G. Zhang, G. Z. Lu, Epoxidation of Propylene by Molecular Oxygen Over the Ag–Y2O3–K2O/α-Al2O3 Catalyst, Catal. Lett. 119 (1) (2007) 185–190.

[40] W. Yao, X. Zheng, Y. Guo, W. Zhan, Y. Guo, G. Lu, Role of Chlorohydrocarbon in Increasing Selectivity of Propylene Oxide over Ag–Y2O3–K2o/α-Al2O3 Catalyst for Epoxidation of Propylene by Molecular Oxygen, J. Mol. Catal. A: Chem. 342 (2011) 30–34.

[41] J. J. Cowell, A. K. Santra, R. M. Lambert, Ultraselective Epoxidation of Butadiene On Cu {111} and the Effects of cs Promotion, J. Am. Chem. Soc. 122 (10) (2000) 2381–2382.

[42] A. K. Santra, J. J. Cowell, R. M. Lambert, Ultra-Selective Epoxidation of Styrene on Pure Cu {111} and the Effects of cs Promotion, Catal. Lett. 67 (2) (2000) 87–91.

[43] J. J. Cowell, A. K. Santra, R. Lindsay, R. M. Lambert, A. Baraldi, A. Goldoni, Bonding and Reactivity of Styrene on Cu (110): Heterogeneous Alkene Epoxidation without the Use of Silver, Surf. Sci. 437 (1-2) (1999) 1–8.

[44] O. P. Vaughan, G. Kyriakou, N. Macleod, M. Tikhov, R. M. Lambert, Copper as a Selective Catalyst for the Epoxidation of Propene, J. Catal. 236 (2) (2005) 401–404.

[45] R. L. Cropley, F. J. Williams, A. J. Urquhart, O. P. Vaughan, M. S. Tikhov, R. M. Lambert, Efficient Epoxidation of a Terminal Alkene Containing Allylic Hydrogen Atoms: Trans-Methylstyrene on Cu {111}, J. Am. Chem. Soc. 127 (16) (2005) 6069–6076.

[46] T. Hayashi, K. Tanaka, M. Haruta, Selective Vapor-Phase Epoxidation of Propylene Over Au/TiO2 Catalysts in the Presence of Oxygen and Hydrogen, J. Catal. 178 (2) (1998) 566–575.

[47] J. Lu, X. Zhang, J. J. Bravo-suárez, T. Fujitani, S. T. Oyama, Effect of Composition and Promoters in Au/TS-1 Catalysts for Direct Propylene Epoxidation Using H2 and O2, Catal. Today 147 (3-4) (2009) 186–195.

[48] B. Taylor, J. Lauterbach, W. Delgass, Gas-Phase Epoxidation of Propylene Over Small Gold Ensembles on TS-1, Appl. Catal., A 291 (1-2) (2005) 188–198.

[49] B. Taylor, J. Lauterbach, G. E. Blau, W. N. Delgass, Reaction Kinetic Analysis of the Gas-Phase Epoxidation of Propylene Over Au/TS-1, J. Catal. 242 (1) (2006) 142–152.

[50] L. Cumaranatunge, W. N. Delgass, Enhancement of Au Capture Efficiency and Activity of Au/TS-1 Catalysts for Propylene Epoxidation, J. Catal. 232 (1) (2005) 38–42.

[51] E. E. Stangland, B. Taylor, R. P. Andres, W. N. Delgass, Direct Vapor Phase Propylene Epoxidation Over Deposition-Precipitation Gold-Titania Catalysts in the Presence of H2/O2: Effects of Support, Neutralizing Agent, and Pretreatment, J. Phys. Chem. B 109 (6) (2005) 2321–2330.

[52] W.-s. Lee, M. C. Akatay, E. A. Stach, F. H. Ribeiro, W. N. Delgass, Reproducible Preparation of Au/TS-1 with High Reaction Rate for Gas Phase Epoxidation of Propylene, J. Catal. 287 (2012) 178–189.

[53] E. A. Carter, W. A. Goddard Iii, The Surface Atomic Oxyradical Mechanism for Ag-Catalyzed Olefin Epoxidation, J. Catal. 112 (1) (1988) 80–92.

[54] E. P. Agency, Presidential Green Chemistry Challenge: 2010 Greener Synthetic Pathways Award, (date of access 07.03.2021).
URL https://www.epa.gov/greenchemistry/

[55] W. Eul, A. Moeller, N. Steiner, Hydrogen Peroxide, American Cancer Society, 2001. doi:10.1002/0471238961.0825041808051919.a01.pub2.

[56] G. Goor, J. Glenneberg, S. Jacobi, J. Dadabhoy, E. Candido, Hydrogen Peroxide, American Cancer Society, 2019, pp. 1–40. doi:10.1002/14356007.a13_443.pub3.

[57] M. Pralus, J. Lecoq, J. Schirmann, New ways in the catalytic epoxidation of olefins by hydrogen peroxide, in: Fundamental Research in Homogeneous Catalysis, Springer, 1979, pp. 327–343.

[58] R. A. Sheldon, J. K. Kochi, Chapter 3 - Metal Catalysis in Peroxide Reactions, in: R. A. SHELDON, J. K. KOCHI (Eds.), Metal-catalyzed Oxidations of Organic Compounds, Academic Press, 1981, pp. 33–70. doi:10.1016/B978-0-12-639380-4.50009-9.

[59] A. Tullo, Dow, BASF to Build Propylene Oxide, Chemical & Engineering News Archive 82 (36) (2004) 15. doi:10.1021/cen-v082n036.p015a.

[60] G.-p. Schindler, C. Walsdorff, R. Korner, H.-g. Gobbel, Process for Producing Propylene Oxide, uS Patent App. 11/168,454 (2007).

[61] T. G. Hofen. W., Process for the Epoxidation of Olefins, Pat Nr. WO 03/016296 A2 (Degussa AG, Uhde GmbH, 2003).

[62] G. H. Grosch, U. Müller, A. Walch, N. Rieber, M. Fischer, S. Quaiser, W. Harder, K. Eller, P. Bassler, A. Wenzel, Others, Method for Oxidizing an Organic Compound Containing at Least One CC Double Bond, uS Patent 6,518,441 (2003).

[63] M. Taramasso, G. Perego, B. Notari, Preparation of Porous Crystalline Synthetic Material Comprised of Silicon and Titanium Oxides, uS Patent 4,410,501 (1983).

[64] J. To, P. Sherwood, A. A. Sokol, I. J. Bush, C. R. A. Catlow, H. J. Van Dam, S. A. French, M. F. Guest, QM/MM Modelling of the TS-1 Catalyst Using HPOX, J. Mater. Chem. 16 (20) (2006) 1919–1926.

[65] M. G. Clerici, Titanium Silicalite-1, John Wiley and Sons, Ltd, 2008, Ch. 18, pp. 705–754. doi:10.1002/9783527626113.ch18.

[66] P. Ratnasamy, D. Srinivas, H. Knözinger, Active Sites and Reactive Intermediates in Titanium Silicate Molecular Sieves, Vol. 48 of Advances in Catalysis, Academic Press, 2004, pp. 1–169. doi:10.1016/S0360-0564(04)48001-8.

[67] G. Perego, R. Millini, G. Bellussi, Synthesis And Characterization Of Molecular Sieves Containing Transition Metals In The Framework, Springer Berlin Heidelberg, Berlin, Heidelberg, 1998, pp. 187–228. doi:10.1007/3-540-69615-6_7.

[68] A. Van Der Pol, J. Van Hooff, Parameters Affecting the Synthesis of Titanium Silicalite 1, Appl. Catal., A 92 (2) (1992) 93–111.

[69] S. B. Shin, D. Chadwick, Kinetics of Heterogeneous Catalytic Epoxidation of Propene with Hydrogen Peroxide Over Titanium Silicalite TS-1, Ind. Eng. Chem. Res. 49 (17) (2010) 8125–8134.

[70] D. Scarano, A. Zecchina, S. Bordiga, F. Geobaldo, G. Spoto, G. Petrini, G. Leofanti, M. Padovan, G. Tozzola, Fourier-Transform Infrared and Raman Spectra of Pure and Al-, B-, Ti-and Fe-Substituted Silicalites: Stretching-Mode Region, J. Chem. Soc. Faraday Trans. 89 (22) (1993) 4123–4130.

[71] E. Astorino, J. B. Peri, R. J. Willey, G. Busca, Spectroscopic Characterization of Silicalite-1 and Titanium Silicalite-1, J. Catal. 157 (2) (1995) 482–500.

[72] F. Geobaldo, S. Bordiga, A. Zecchina, E. Giamello, G. Leofanti, G. Petrini, Drs UV-vis and EPR Spectroscopy of Hydroperoxo and Superoxo Complexes in Titanium Silicalite, Catal. Lett. 16 (1-2) (1992) 109–115.

[73] R. Millini, E. P. Massara, G. Perego, G. Bellussi, Framework Composition of Titanium Silicalite-1, J. Catal. 137 (2) (1992).

[74] J.-p. Catinat, M. Strebelle, Process for Regeneration of Catalysts of Titanium Silicalite Type, uS Patent 6,169,050 (2001).

[75] U. Müller, J. H. Teles, A. Wenzel, W. Harder, P. Rudolf, A. Rehfinger, P. Baβler, N. Rieber, Method for Regenerating a Zeolite Catalyst, uS Patent 6,790,969 (2004).

[76] G. Thiele, Method for the Regeneration of a Catalyst, uS Patent 5,620,935 (1997).

[77] Y. Zuo, M. Wang, W. Song, X. Wang, X. Guo, Characterization and Catalytic Performance of Deactivated and Regenerated TS-1 Extrudates in a Pilot Plant of Propene Epoxidation, Ind. Eng. Chem. Res. 51 (32) (2012) 10586–10594.

[78] W. Feng, Y. Wang, G. Wu, Y. Lin, J. Xu, H. Shi, T. Zhang, S. Wang, X. Wu, P. Yao, Liquid Phase Propylene Epoxidation With H2O2 on TS-1/SiO2 Catalyst in a Fixed-Bed Reactor: Experiments and Deactivation Kinetics, J. Chem. Technol. Biotechnol. 90 (8) (2015) 1489–1496.

[79] Q. Wang, L. Wang, J. Chen, Y. Wu, Z. Mi, Deactivation and Regeneration of Titanium Silicalite Catalyst for Epoxidation of Propylene, J. Mol. Catal. A: Chem. 273 (1-2) (2007) 73–80.

[80] M. Clerici, G. Bellussi, U. Romano, Synthesis of Propylene Oxide from Propylene and Hydrogen Peroxide Catalyzed by Titanium Silicalite, J. Catal. 129 (1) (1991) 159–167.

[81] M. G. Clerici, P. Ingallina, Epoxidation of Lower Olefins with Hydrogen Peroxide and Titanium Silicalite, J. Catal. 140 (1) (1993) 71–83.

[82] G. Thiele, Process for the Production of Epoxides from Olefins, uS Patent 5,675,026 (1997).

[83] V. Russo, R. Tesser, E. Santacesaria, M. Di Serio, Kinetics of Propene Oxide Production Via Hydrogen Peroxide with TS-1, Ind. Eng. Chem. Res. 53 (15) (2014) 6274–6287.

[84] A. Sulimov, S. Danov, A. Ovcharova, A. Ovcharov, V. Flid, Kinetics of Propylene Epoxidation with Hydrogen Peroxide Catalyzed by Extruded Titanium Silicalite in Methanol, Kinet. Catal. 57 (4) (2016) 466–473.

[85] Z. Pastukhova, V. Levitin, E. Katsman, L. Bruk, Others, Kinetics and Mechanism of Allyl Alcohol Epoxidation with Hydrogen Peroxide on a Titanium Silicalite Catalyst TS-1. Formulation and Discrimination Between Hypothetical Mechanisms, Kinet. Catal. 62 (5) (2021) 604–620.

[86] M. Alvear, K. Eraenen, D. Y. Murzin, T. Salmi, Study of the Product Distribution in the Epoxidation of Propylene Over TS-1 Catalyst in a Trickle-Bed Reactor, Ind. Eng. Chem. Res. 60 (6) (2021) 2430–2438.

[87] J. H. Teles, A. Rehfinger, P. Bassler, A. Wenzel, N. Rieber, P. Rudolf, Method for the Production of Propylene Oxide, uS Patent 6,756,503 (2004).

[88] S. Danov, A. Sulimov, V. Kolesnikov, A. Ovcharov, Kinetics of Propylene Epoxidation with Hydrogen Peroxide, Kinet. Catal. 54 (2) (2013) 193–198.

[89] X. Liang, Z. Mi, Y. Wu, L. Wang, E. Xing, Kinetics of Epoxidation of Propylene Over TS-1 in Isopropanol, React. Kinet. Catal. Lett. 80 (2) (2003) 207–215.

[90] G. Wu, Y. Wang, L. Wang, W. Feng, H. Shi, Y. Lin, T. Zhang, X. Jin, S. Wang, X. Wu, Others, Epoxidation of Propylene with H2O2 Catalyzed by Supported TS-1 Catalyst in a Fixed-Bed Reactor: Experiments and Kinetics, Chem. Eng. J. 215 (2013) 306–314.

[91] L. Wang, Y. Wang, G. Wu, W. Feng, T. Zhang, R. Yang, X. Jin, H. Shi, S. Wang, Epoxidation of Propylene Over Titanosilicate-1 in Fixed-Bed Reactor: Experiments and Kinetics, Asian J. Chem. 26 (2014) 943–950. doi:10.14233/ajchem.2014.15519.

[92] Y. Wu, Q. Liu, X. Su, Z. Mi, Effect of Solvents on Propylene Epoxidation over TS-1 Catalyst, Front. Chem. China 3 (1) (2008) 112–117.

[93] A. Corma, P. Esteve, A. Martınez, Solvent Effects during the Oxidation of Olefins and Alcohols with Hydrogen Peroxide on Ti-beta Catalyst: The Influence of the Hydrophilicity–Hydrophobicity of the Zeolite, J. Catal. 161 (1) (1996) 11–19.

[94] J. C. Van Der Waal, H. Van Bekkum, Zeolite Titanium Beta: A Versatile Epoxidation Catalyst. Solvent Effects, J. Mol. Catal. A: Chem. 124 (2-3) (1997) 137–146.

[95] M. Boccuti, K. Rao, A. Zecchina, G. Leofanti, G. Petrini, Spectroscopic Characterization of Silicalite and Titanium-Silicalite, in: Studies in Surface Science and Catalysis, Vol. 48, Elsevier, 1989, pp. 133–144.

[96] B. Notari, Synthesis and Catalytic Properties of Titanium Containing Zeolites, in: Studies in Surface Science and Catalysis, Vol. 37, Elsevier, 1988, pp. 413–425.

[97] G. Bellussi, A. Carati, M. G. Clerici, G. Maddinelli, R. Millini, Reactions of Titanium Silicalite with Protic Molecules and Hydrogen Peroxide, J. Catal. 133 (1) (1992) 220–230. doi:10.1016/0021-9517(92)90199-R.

[98] S. Bordiga, S. Coluccia, C. Lamberti, L. Marchese, A. Zecchina, F. Boscherini, F. Buffa, F. Genoni, G. Leofanti, XAFS Study of Ti-Silicalite: Structure of Framework Ti (IV) in the Presence and Absence of Reactive Molecules (H2O, NH3) and Comparison with Ultraviolet-Visible and IR Results, J. Phys. Chem. 98 (15) (1994) 4125–4132.

[99] P. E. Sinclair, C. R. A. Catlow, Quantum Chemical Study of the Mechanism of Partial Oxidation Reactivity in Titanosilicate Catalysts: Active Site Formation, Oxygen Transfer, and Catalyst Deactivation, J. Phys. Chem. B., 103 (7) (1999) 1084–1095.

[100] C. Lamberti, S. Bordiga, A. Zecchina, G. Artioli, G. Marra, G. Spano, Ti Location in the MFI Framework of Ti- Silicalite-1: A Neutron Powder Diffraction Study, J. Am. Chem. Soc. 123 (10) (2001) 2204–2212.

[101] L. Wang, G. Xiong, J. Su, P. Li, H. Guo, In Situ UV Raman Spectroscopic Study on the Reaction Intermediates for Propylene Epoxidation on TS-1, J. Phys. Chem. C 116 (16) (2012) 9122–9131.

[102] J. To, A. A. Sokol, S. A. French, C. R. A. Catlow, Hybrid QM/MM Investigations Into the Structure and Properties of Oxygen-Donating Species in TS-1, The Journal of Physical Chemistry C 112 (18) (2008) 7173–7185.

[103] S. Bordiga, A. Damin, F. Bonino, G. Ricchiardi, A. Zecchina, R. Tagliapietra, C. Lamberti, Resonance Raman Effects in TS-1: The Structure of Ti (IV) Species and Reactivity Towards H2O, NH3 and H2O2: An In Situ Study, Phys. Chem. Chem. Phys. 5 (20) (2003) 4390–4393.

[104] D. H. Wells Jr, W. N. Delgass Jr, K. T. Thomson, Evidence of Defect-Promoted Reactivity for Epoxidation of Propylene in Titanosilicate TS-1 Catalysts: A DFT study, J. Am. Chem. Soc. 126 (9) (2004) 2956–2962.

[105] X. Nie, X. Ji, Y. Chen, X. Guo, C. Song, Mechanistic Investigation of Propylene Epoxidation with H2O2 Over TS-1: Active Site Formation, Intermediate Identification, and Oxygen Transfer Pathway, Mol. Catal. 441 (2017) 150–167.

[106] X. Nie, X. Ren, X. Ji, Y. Chen, M. J. Janik, X. Guo, C. Song, Mechanistic Insight Into Propylene Epoxidation with H2O2 Over Titanium Silicalite-1: Effects of Zeolite Confinement and Solvent, J. Phys. Chem. B 123 (34) (2019) 7410–7423.

[107] C. P. Gordon, H. Engler, A. S. Tragl, M. Plodinec, T. Lunkenbein, A. Berkessel, J. H. Teles, A.-n. Parvulescu, C. Copéret, Efficient Epoxidation Over Dinuclear Sites in Titanium Silicalite-1, Nature 586 (7831) (2020) 708–713.

[108] G. Xiong, Y. Cao, Z. Guo, Q. Jia, F. Tian, L. Liu, The Roles of Different Titanium Species in TS-1 Zeolite in Propylene Epoxidation Studied by In Situ UV Raman Spectroscopy, Phys. Chem. Chem. Phys. 18 (1) (2016) 190–196.

[109] T. Haas, W. Hofen, J. Sauer, G. Thiele, Process for the Epoxidation of Olefins, uS Patent 6,600,055 (2003).

[110] A. Sulimov, S. Danov, A. Ovcharova, A. Ovcharov, V. Flid, Studying the Effect of Process Parameters on the Epoxidation of Propylene in a Methanol Medium in the Presence of Extruded Titanium Silicate, Catal. Ind. 8 (2) (2016) 116–120.

[111] C. G. Visconti, G. Groppi, E. Tronconi, Highly Conductive Packed Foams: A New Concept for the Intensification of Strongly Endo-and Exo-Thermic Catalytic Processes in Compact Tubular Reactors, Catal. Today 273 (2016) 178–186.

[112] A. Cybulski, J. A. Moulijn, Structured Catalysts And Reactors, CRC press, 2005.

[113] O. Laguna, P. Lietor, F. I. Godino, F. Corpas-iglesias, A Review on Additive Manufacturing and Materials for Catalytic Applications: Milestones, Key Concepts, Advances and Perspectives, Mater. Des. 208 (2021) 109927.

[114] C. Busse, H. Freund, W. Schwieger, Intensification of Heat Transfer in Catalytic Reactors by Additively Manufactured Periodic Open Cellular Structures (POCS), Chem. Eng. Process. 124 (2018) 199–214.

[115] E. Bianchi, W. Schwieger, H. Freund, Assessment of Periodic Open Cellular Structures for Enhanced Heat Conduction in Catalytic Fixed-Bed Reactors, Adv. Eng. Mater. 18 (4) (2016) 608–614.

[116] G. Littwin, S. Roder, H. Freund, Systematic Experimental Investigations and Modeling of the Heat Transfer in Additively Manufactured Periodic Open Cellular Structures with Diamond Unit Cell, Ind. Eng. Chem. Res. 60 (18) (2021) 6753–6766.

[117] M. Klumpp, A. Inayat, J. Schwerdtfeger, C. Körner, R. Singer, H. Freund, W. Schwieger, Periodic Open Cellular Structures with Ideal Cubic Cell Geometry: Effect of Porosity and Cell Orientation on Pressure Drop Behavior, Chemical Engineering Journal 242 (2014) 364–378.

[118] V. V. Calmidi, R. L. Mahajan, Forced Convection in High Porosity Metal Foams, J. Heat Transfer 122 (3) (2000) 557–565.

[119] D. Edouard, T. T. Huu, C. P. Huu, F. Luck, D. Schweich, The Effective Thermal Properties of Solid Foam Beds: Experimental and Estimated Temperature Profiles, International journal of heat and mass transfer 53 (19-20) (2010) 3807–3816.

[120] M. Wallenstein, M. Kind, B. Dietrich, Radial Two-Phase Thermal Conductivity and Wall Heat Transfer Coefficient of Ceramic Sponges–Experimental Results and Correlation, International Journal of Heat and Mass Transfer 79 (2014) 486–495.

[121] Y. Peng, J. Richardson, Properties of Ceramic Foam Catalyst Supports: One-Dimensional and Two-Dimensional Heat Transfer Correlations, Applied Catalysis A: General 266 (2) (2004) 235–244.

[122] E. Bianchi, T. Heidig, C. G. Visconti, G. Groppi, H. Freund, E. Tronconi, Heat Transfer Properties of Metal Foam Supports for Structured Catalysts: Wall Heat Transfer Coefficient, Catalysis today 216 (2013) 121–134.

[123] E. Bianchi, G. Groppi, W. Schwieger, E. Tronconi, H. Freund, Numerical Simulation of Heat Transfer in the Near-Wall Region of Tubular Reactors Packed With Metal Open-Cell Foams, Chemical Engineering Journal 264 (2015) 268–279.

[124] A. Lind, Ø. Vistad, M. F. Sunding, K. A. Andreassen, J. H. Cavka, C. A. Grande, Multi-Purpose Structured Catalysts Designed and Manufactured by 3D Printing, Mater. Des. 187 (2020) 108377.

[125] S. Danaci, L. Protasova, J. Lefevere, L. Bedel, R. Guilet, P. Marty, Efficient CO2 Methanation Over Ni/Al2O3 Coated Structured Catalysts, Catal. Today 273 (2016) 234–243.

[126] T. Stiegler, K. Meltzer, A. Tremel, M. Baldauf, P. Wasserscheid, J. Albert, Development of a Structured Reactor System for CO2 Methanation Under Dynamic Operating Conditions, Energy Technol. 7 (6) (2019) 1900047.

[127] C. Spille, V. P. Tholan, B. Straiton, M. Johannsen, M. Hoffmann, Q. Marashdeh, M. Schlüter, Electrical Capacitance Volume Tomography (ECVT) for Characterization of Additively Manufactured Lattice Structures (AMLS) in Gas-Liquid Systems, Fluids 6 (9) (2021) 321.

[128] C. Spille, A. Lyberis, M. I. Maiwald, D. Herzog, M. Hoffmann, C. Emmelmann, M. Schlüter, Smart-Reactors: Tailoring Gas Holdup Distribution by Additively Manufactured Lattice Structures, Chemical engineering & technology 43 (10) (2020) 2053–2061.

[129] F. Kapteijn, J. A. Moulijn, Laboratory Testing of Solid Catalysts, Handb. Heterog. Catal. 4 (2008) 2.

[130] S. L. Shannon, J. G. Goodwin Jr, Characterization of Catalytic Surfaces by Isotopic-Transient Kinetics During Steady-State Reaction, Chem. Rev. 95 (3) (1995) 677–695.

[131] J. T. Gleaves, J. Ebner, T. Kuechler, Temporal Analysis of Products TAPa Unique Catalyst Evaluation System with Submillisecond Time Resolution, Catal. Rev.: Sci. Eng. 30 (1) (1988) 49–116.

[132] J. T. Gleaves, G. Yablonsky, X. Zheng, R. Fushimi, P. L. Mills, Temporal Analysis of Products TAPRecent Advances in Technology for Kinetic Analysis of Multi-Component Catalysts, J. Mol. Catal. A: Chem. 315 (2) (2010) 108–134.

[133] K. Morgan, J. Touitou, J.-s. Choi, C. Coney, C. Hardacre, J. A. Pihl, C. E. Stere, M.-y. Kim, C. Stewart, A. Goguet, Others, Evolution and Enabling Capabilities of Spatially Resolved Techniques for the Characterization of Heterogeneously Catalyzed Reactions, ACS Catal. 6 (2) (2016) 1356–1381.

[134] R. Horn, K. Williams, N. Degenstein, L. Schmidt, Syngas by Catalytic Partial Oxidation of Methane On Rhodium: Mechanistic Conclusions from Spatially Resolved Measurements and Numerical Simulations, J. Catal. 242 (1) (2006) 92–102.

[135] O. Korup, C. F. Goldsmith, G. Weinberg, M. Geske, T. Kandemir, R. Schlögl, R. Horn, Catalytic Partial Oxidation of Methane on Platinum Investigated by Spatial Reactor Profiles, Spatially Resolved Spectroscopy, And Microkinetic Modeling, J. Catal. 297 (2013) 1–16.

[136] H. Schwarz, M. Geske, C. F. Goldsmith, R. Schlögl, R. Horn, Fuel-rich Methane Oxidation in a High-Pressure Flow Reactor Studied by Optical-Fiber Laser-Induced Fluorescence, Multi-Species Sampling Profile Measurements and Detailed Kinetic Simulations, Combust. Flame 161 (7) (2014) 1688–1700.

[137] M. E. Davis, R. J. Davis, 5.4 Evaluation Of Kinetic Parameters, Courier Corporation, 2012.

[138] G. Ertl, H. Knözinger, J. Weitkamp, Others, Handbook Of Heterogeneous Catalysis, Vol. 2, Citeseer, 1997.

[139] J. J. Carberry, Chemical And Catalytic Reaction Engineering, Courier Corporation, 2001.

[140] D. E. Mears, Diagnostic Criteria for Heat Transport Limitations in Fixed Bed Reactors, J. Catal. 20 (2) (1971) 127–131.

[141] P. Weisz, C. Prater, Interpretation of Measurements in Experimental Catalysis, in: Advances in catalysis, Vol. 6, Elsevier, 1954, pp. 143–196.

[142] M. E. Davis, R. J. Davis, 6.3 Internal Transport Effects, Vol. 2, McGraw-Hill, New York, 2012.

[143] D. Serrano, R. Sanz, P. Pizarro, I. Moreno, P. De Frutos, S. Blázquez, Preparation of Extruded Catalysts Based on TS-1 Zeolite for Their Application in Propylene Epoxidation, Catal. Today 143 (1-2) (2009) 151–157.

[144] Y. Zuo, M. Liu, L. Hong, M. Wu, T. Zhang, M. Ma, C. Song, X. Guo, Role of Supports in the Tetrapropylammonium Hydroxide Treated Titanium Silicalite-1 Extrudates, Ind. Eng. Chem. Res. 54 (5) (2015) 1513–1519.

[145] Y. Liu, Y. Y. Zhang, T. Y. Yang, W. L. He, Study on the Calcination of Titanium Silicalite Zeolite TS-, in: Adv. Mater. Res., Vol. 287, Trans Tech Publ, 2011, pp. 317–321.

[146] W. Philip, Coating, Reaction Analysis and Simulation of a Periodic Open Cell Structure with a TS-1 Catalyst for the Epoxidation of Propylene in a Profile Reactor, Master Thesis, Hamburg University of Technology (2021).

[147] L. Scriven, Physics and Applications of Dip Coating and Spin Coating, MRS Online Proc. Libr. 121 (1988).

[148] A. I. Vogel, J. Bassett, J. Bassett, Vogel's Textbook Of Quantitative Inorganic Analysis: Including Elementary Instrumental Analysis, Longman London, 1978.

[149] J. Reichert, S. Mcneight, H. Rudel, Determination of Hydrogen Peroxide and Some Related Peroxygen Compounds, Ind. Eng. Chem., Anal. Ed. 11 (4) (1939) 194–197.

[150] A. G. Dixon, M. Nijemeisland, CFD as a Design Tool for Fixed-Bed Reactors, Ind. Eng. Chem. Res. 40 (23) (2001) 5246–5254.

[151] R. A. Bernard, R. H. Wilhelm, Turbulent Diffusion in Fixed Beds of Packed Solids, Chem. Eng. Prog. 46 (5) (1950) 233–244.

[152] R. Bauer, Effective Radial Thermal Conductivity of Packings in Gas Flow, Int. Chem. Eng. 18 (1978) 181–204.

[153] H. F. Rase, Chapter 5 - Design and Operating Models, in: H. F. Rase (Ed.), Fixed-Bed Reactor Design and Diagnostics, Butterworth-Heinemann, 1990, pp. 105–155. doi:10.1016/B978-0-409-90003-3.50011-7.

[154] V. Specchia, S. Sicardi, Modified Correlation for the Conductive Contribution of Thermal Conductivity in Packed Bed Reactors, Chem. Eng. Commun. 6 (1-3) (1980) 131–139.

[155] M. Edwards, J. Richardson, Gas Dispersion in Packed Beds, Chem. Eng. Sci. 23 (2) (1968) 109–123.

[156] R. L. Kabel, Models for Flow Systems and Chemical reactors, c. y. wen and l. t. fan, marcel dekker, inc., new york, 581 pages., AIChE J. 22 (2) (1976) 412–412. doi:10.1002/aic.690220233.

[157] K. Bischoff, O. Levenspiel, Fluid DispersionGeneralization and Comparison of Mathematical ModelsII Comparison of Models, Chem. Eng. Sci. 17 (4) (1962) 257–264.

[158] R. Wilhelm, Progress Towards the a Priori Design of Chemical Reactors, Pure Appl. Chem. 5 (3-4) (1962) 403–422.

[159] E. Tsotsas, M7 Heat and Mass Transfer in Packed Beds with Fluid Flow, in: VDI Heat Atlas, 2010.

[160] R. Benenati, C. Brosilow, Void Fraction Distribution in Beds of Spheres, AIChE J. 8 (3) (1962) 359–361.

[161] L. Roblee, R. Baird, J. Tierney, Radial Porosity Variations in Packed Beds, AIChE J. 4 (4) (1958) 460–464.

[162] E. Tsotsas, D6 Properties Of Solids And Solid Materials, Springer Berlin Heidelberg, Berlin, Heidelberg, 2010, pp. 570–580. doi:10.1007/978-3-540-77877-6_26.

[163] V. Gnielinski, G9 Fluid-Particle Heat Transfer In Flow Through Packed Beds Of Solids, Springer Berlin Heidelberg, Berlin, Heidelberg, 2010, pp. 743–744. doi:10.1007/978-3-540-77877-6_42.

[164] C. R. Wilke, P. Chang, Correlation of Diffusion Coefficients in Dilute Solutions, AIChE J. 1 (2) (1955) 264–270. doi:10.1002/aic.690010222.

[165] U. Hanefeld, L. Lefferts, Catalysis: An Integrated Textbook For Students, John Wiley & Sons, 2018.

[166] D. W. Pepper, J. C. Heinrich, The Finite Element Method: Basic Concepts And Applications With Matlab, MAPLE, And COMSOL, CRC press, 2017.

[167] G. D. Wehinger, M. Kraume, V. Berg, O. Korup, K. Mette, R. Schlögl, M. Behrens, R. Horn, Investigating Dry Reforming of Methane With Spatial Reactor Profiles and Particle-Resolved CFD Simulations, AIChE J. 62 (12) (2016) 4436–4452.

[168] H. Schwarz, Y. Dong, R. Horn, Catalytic Methane Combustion on a Pt Gauze: Laser-Induced Fluorescence Spectroscopy, Species Profiles, and Simulations, Chem. Eng. Technol. 39 (11) (2016) 2011–2019.

[169] Y. Dong, O. Korup, J. Gerdts, B. R. Cuenya, R. Horn, Microtomography-Based CFD Modeling of a Fixed-Bed Reactor with an Open-Cell foam Monolith and Experimental Verification by Reactor Profile Measurements, Chem. Eng. J. 353 (2018) 176–188.

[170] Y. Dong, M. Geske, O. Korup, N. Ellenfeld, F. Rosowski, C. Dobner, R. Horn, What Happens in a Catalytic Fixed-Bed Reactor for N-Butane Oxidation to Maleic Anhydride? Insights from Spatial Profile Measurements and Particle Resolved CFD Simulations, Chem. Eng. J. 350 (2018) 799–811.

[171] B. Wojciechowski, N. Rice, 8 - Fitting Rate Expressions to TSR Data, in: B. Wojciechowski, N. Rice (Eds.), Experimental Methods in Kinetic Studies, Elsevier Science, Amsterdam, 2003, pp. 183–195. doi:10.1016/B978-044451314-4/50009-5.

[172] K. Madsen, H. Nielsen, O. Tingleff, Methods for Non-Linear Least Squares Problems (2nd ed.) (2004) 60.

[173] 7. Kinetic Parameters From Fitting LangmuirHinshelwood Models, John Wiley & Sons, Ltd, 2003, pp. 288–290. doi:10.1002/3527602658.ch7.

[174] M. Schmal, Chemical Reaction Engineering: Essentials, Exercises And Examples, CRC Press, 2014.

[175] A. Aquino, O. Korup, R. Horn, Liquid Phase Epoxidation of Propylene to Propylene Oxide with Hydrogen Peroxide on Titanium Silicalite-1: Spatially Resolved Measurements and Numerical Simulations, Industrial & Engineering Chemistry Research 62 (7) (2023) 3098–3115. doi:10.1021/acs.iecr.2c03373.

[176] A. Aquino, Liquid Phase Selective Oxidation of Propylene to Propylene Oxide on Titanium Silicalite Catalyst in a Compact Profile Reactor, Master Thesis, Hamburg University of Technology (2001).

[177] S. Bordiga, F. Bonino, A. Damin, C. Lamberti, Reactivity of Ti(IV) Species Hosted in TS-1 Towards H2O2/H2O Solutions Investigated by Ab Initio Cluster and Periodic Approaches Combined with Experimental XANES and EXAFS Data: A Review and New Highlights, Physical Chemistry Chemical Physics 9 (35) (2007) 4854–4878.

[178] C. Lamberti, S. Bordiga, D. Arduino, A. Zecchina, F. Geobaldo, G. Spano, F. Genoni, G. Petrini, A. Carati, F. Villain, Others, Evidence of the Presence of Two Different Framework Ti (IV) Species in Ti- Silicalite-1: In Vacuo Conditions: An EXAFS and a Photoluminescence Study, The Journal of Physical Chemistry B 102 (33) (1998) 6382–6390.